Coherent Multidimensional Off-resonant THz Spectroscopy on Semiconductors

D I S S E R T A T I O N

zur Erlangung des akademischen Grades

Dr. rerum naturalium
(Dr. rer. nat.)
im Fach Physik

eingereicht an der
Mathematisch-Naturwissenschaftlichen Fakultät
Humboldt-Universität zu Berlin

von

Dipl.-Phys. Carmine Somma

Präsidentin der Humboldt-Universität zu Berlin:
Prof. Dr.-Ing. Dr. Sabine Kunst

Dekan der Mathematisch-Naturwissenschaftlichen Fakultät :
Prof. Dr. Elmar Kulke

Gutachter/innen:
1. Prof. Dr. Thomas Elsaesser
2. Prof. Dr. Kurt Busch
3. Prof. Dr. Manfred Helm

Tag der mündlichen Prüfung:
13th June 2017

Abstract

The work presented in this thesis is motivated by three inter-connected objectives: to study new coherent sources of high-field ultra-broadband terahertz (THz) pulses for multi-octave THz spectroscopy, to develop novel techniques in the frequency range 0.1-30 THz capable of accessing single and multiple quantum coherences off-resonantly under nonperturbative conditions and to understand their dynamics on their fundamental ultrafast time scale.

For the first time, the coherent generation of ultrashort MV/cm field pulses with a spectral content covering the frequency range 0.1-30 THz continuously is demonstrated in the organic crystal DSTMS by non-phase-matched difference frequency mixing within the broad spectrum of femtosecond near infrared pulses.

Coherent multidimensional terahertz spectroscopy (CMTS) has developed into an important technique for, e.g, driving low-energy excitations in both bulk and nanostructured semiconductors and monitoring their coherent dynamics. A novel CMTS technique employing three phase-locked inter-delayed THz pulses is implemented. It relies on a collinear interaction of the pulses with a sample, so that different contributions to the nonlinear signal are emitted in the same direction, and thus can be measured all at once. Phase-resolved detection by electro-optic sampling allows for measuring amplitude and absolute phase of the nonlinear signal, thereby enabling to investigate the evolution of coherent interactions between quantum excitations in real time. In CMTS, the nonlinear signal is dissected into the distinct nonlinear contributions in the corresponding multidimensional frequency domain.

This novel technique is applied to study the nonlinear off-resonant response of two undoped bulk semiconductors, the wide-bandgap ferroelectric lithium niobate ($LiNbO_3$, $E_g = 1000$ THz) and the narrow-bandgap indium antimonide (InSb, $E_g = 40$ THz), in the nonperturbative regime. In $LiNbO_3$, the nonlinear signal is generated by a femtosecond nonlinear shift current (SC), which is a distinctive characteristic of the bulk photovoltaic effect. The SC stems from the lack of inversion symmetry and the ultrafast dephasing of the field-induced interband coherent polarization due to a sufficiently high decoherence rate, which enables tunneling of electrons from the valence to the conduction band. In InSb, the nonlinear signal is caused by the coherent response on both the two-phonon and two-photon interband excitations. The impulsive generation of the two-phonon coherent polarization is enhanced by the large interband transition dipole of InSb, resulting in much larger polarization amplitudes than in the regime of linear response. In the future, CMTS could be applied for example to gain further insight in magnetic multi-quantum coherences of materials with long range magnetic order. Furthermore this novel concept can be easily implemented into two-colour nonlinear spectroscopic experiments.

Abstract

Diese Dissertationsschrift behandelt drei miteinander verbundene Themen; die Erforschung neuer kohärenter Höchstfeld-Terahertzpulse mit ultrabreitbandigem Spektrum für Spektroskopie über mehrere Oktaven der Wellenlänge, die Entwicklung neuartiger Verfahren im Frequenzbereich von 0.1–30 THz für die Beobachtung von Quantenkohärenzen im nicht-resonanten, nicht-perturbativen Regime und das Verständnis der Dynamik dieser Quantenkohärenzen auf deren ultrakurzen Zeitskalen.

Zum ersten Mal konnte die kohärente Erzeugung von ultrakurzen Pulsen mit Feldstärken im MV/cm Bereich mit einem kontinuierlichen Spektralbereich von 0.1–30 THz im organischen Kristall DSTMS mit nicht-phasenangepasster Differenzfrequenzmischung innerhalb des breitbandigen Spektrums von Femtosekundenpulsen im nahen-Infrarot gezeigt werden.

Kohärente mehrdimensionale Terahertzspektroskopie (CMTS) hat sich zu einer wichtigen Methode zur Untersuchung der niederenergetischen Anregungen von makroskopischen und nanostrukturierten Halbleitern and deren kohärenter Dynamik entwickelt. Eine neuartige CMTS Methode mit drei phasenstarren, zueinander zeitverzögerten Terahertzpulsen wurde entwickelt. Sie beruht auf der kollinearen Wechselwirkung der Pulse mit der Probe, sodass verschiedene Ordnungen des nichtlinearen Signals in gleicher Richtung emittiert werden und deshalb gleichzeitig gemessen werden können. Amplitude und Phase des nichtlinearen Signals können durch elektro-optisches Abtasten vermessen werden, wodurch die zeitliche Entwicklung der kohärenten Wechselwirkungen in Echtzeit untersucht werden kann. CMTS erlaubt zusätzlich die eindeutige Zerlegung des nichtlinearen Signals in die verschiedenen nichtlinearen Ordnungen in der jeweiligen mehrdimensionalen Frequenzdomäne.

Die nichtlineare, nicht-resonante Antwort zweier undotierter Halbleiter, des Ferroelektrikums Lithiumniobat mit großer Bandlücke ($LiNbO_3$, $E_g = 1000$ THz) und Indiumantimonids mit kleiner Bandlücke (InSb, $E_g = 40$ THz) kann mit dieser neuartigen Methode im nicht-perturbativem Regime untersucht werden. In $LiNbO_3$ wird das nichtlineare Signal durch einen Femtosekunden nichtlinearen Verschiebestrom (SC) hervorgerufen. Dies ist ein eindeutiges Charakteristikum des photovoltaischen Effekts im Volumenkristall. Der Verschiebestrom wird durch die gebrochene Inversionssymmetrie des Kristalls in Verbindung mit einer ultraschnellen Dephasierung der feldinduzierten, kohärenten interband-Polarisation hervorgerufen. Die Dephasierung der interband-Polarisation erlaubt das Tunneln von Elektronen vom Valenzband in das Leitungsband. In InSb wird das kohärente Signal durch sowohl zwei-Phonen als auch zwei-Photonen interband-Anregungen erzeugt. Die impulsive Anregung einer kohärenten zwei-Phononen Polarisation wird durch das große Übergangsdipolmoment von InSb verstärkt, was zu deutlich größeren Amplituden der Polarisation als im linearem Regime führt. In der Zukunft kann CMTS zum Beispiel verwendet werden, um einen tieferen Einbick in die magnetische Multi-Quanten Koheränz in Materialien mit langreichweitiger magnetischer Ordnung zu gewinnen. Darüber hinaus kann CMTS einfach innerhalb der nichtlinearen Zwei-Farben Spektroskopie realisiert werden.

Contents

Introduction

The terahertz (THz) range of the electromagnetic spectrum bridges the microwave and the far infrared regions, being conventionally defined from 0.1 to 10 THz (3.33 cm^{-1} to 333.6 cm^{-1}). Distinct spectral fingerprints of free carriers, low-energy excitations in semiconductor structures, e.g., phonons, polarons and excitons, and both vibrational and rotational modes of many large molecules occur in the THz range.

This region has been the last spectral range to be spectroscopically explored owing to the lack of coherent sources and detectors. During the Eighties, advances in electrooptics and photoconduction methods made it possible to coherently generate and detect THz radiation, thereby leading to the development of broadband time-domain THz spectroscopy [6, 7, 111]. The growing demand for THz pulses with bandwidth even larger than the conventional THz range in spectroscopic applications led to a great deal of effort for studying different types of ultra-broadband THz sources [74, 75, 86, 108]. In this respect, organic nonlinear crystals have gained an important role [15, 84, 114].

Over the last two decades incisive and further advances in the generation and the control of femtosecond high-field THz pulses [36, 46, 48, 49, 103] have opened up the way to new spectroscopic techniques for investigating the light-matter interaction on an ultrafast time scale in the strong-field regime. Nonlinear THz spectroscopies, e.g., nonlinear THz transmission and THz-pump/THz-probe, have enabled to access nonequilibrium dynamics and nonlinear carrier coherent transport in semiconductor-based systems. More specifically, a wealth of fascinating nonlinear phenomena, such as light impact ionization, multiphoton absorption, multiphoton-assisted or field-induced interband tunneling, polaronic effects and ballistic carrier transports, have been driven either resonantly or nonresonantly by THz radiation with strong electric fields and have been monitored by phase-resolved techniques [17, 37, 50, 52, 53, 61, 76, 77].

Despite the maturity of such methods, a coherent multidimensional terahertz spectroscopy is necessary to investigate the unexplored field of the multi-

quantum coherences in the THz range. To this purpose, starting from the pioneering work of Kuehn et al. [78] we have developed a novel two-dimensional (2D) THz spectroscopy, employing three strong collinear THz pulses with variable delays. This technique allows to monitor the nonlinear response as a function of three time variables. As a result, the nonlinear electric field appears as dissected in different contributions in the corresponding multidimensional frequency domain, leading to a straightforward analysis of it.

This thesis focuses on the nonlinear response of semiconductors driven off-resonantly in nonperturbative conditions, demonstrating intriguing quantum-mechanical aspects of light-matter interaction.

Outline

The thesis begins with a chapter on theoretical and experimental concepts in the generation and detection of ultrashort broadband THz pulses. After a comparison among different methods for generating THz pulses with high electric field, the discussion is focused on phase-matched difference frequency generation and on how the latter is employed in the nonlinear crystal GaSe in order to achieve a tunable coherent THz source. Afterwards, phase-resolved detection in the nonlinear crystal ZnTe via electro-optic sampling is discussed. The last section of this chapter concerns the coherent THz generation in the nonlinear organic crystal DSTMS and its application in a spectroscopic measurement. This study demonstrates that this inorganic crystal holds the potential for being employed in multi-octave THz transmission spectroscopy.

Chapter 2 addresses THz multidimensional coherent spectroscopy. Initially, the main differences between this novel approach and the traditional multidimensional spectroscopic techniques established in the infrared and the visible ranges are assessed. Then, the retrieval of the nonlinear electric field is discussed. Regarding the analysis of the nonlinear signal, the concept of multidimensional frequency vectors is introduced, being a powerful mathematical tool for identifying the various contributions, i.e., rephasing and nonrephasing parts of the nonlinear response. Furthermore, in the perspective of visualizing the light-matter interactions in nonlinear processes schematically, a representation of the Liouville pathways, equivalent to the double-sided Feynman diagrams, is discussed. A description of the experimental setup for two-dimensional nonlinear THz spectroscopy with two and three pulses is the subject of last section of this chapter.

The possibility of driving a current in an insulator in extremely off-resonance conditions is addressed in Chap. 3. The nonlinear response of the wide-bandgap

($E_g \backsimeq 1000$ THz) ferroelectric crystal lithium niobate ($LiNbO_3$) is investigated by 2D nonlinear spectroscopy employing two strong 2-THz fields. The main contribution to the nonlinear signal consists in a nonresonant-interband-tunnelling current stemming from both the ultrafast destruction of the coherent interband polarizazion created by the driving THz field and the lack of inversion symmetry in the crystal structure.

Applying a sequence of off-resonant THz pulses with high electric field on a semiconductor allows for generating two-quantum coherences corresponding to quantum excitations of the system. The mechanisms of generation and dephasing of such multi-quantum coherent polarizations are investigated via 2D nonlinear spectroscopy with three high-field 22-THz pulses in the prototypical narrow-bandgap ($E_g \backsimeq 41$ THz) indium antimonide InSb. The results are presented and discussed in Chap. 4.

Chapter 1

Experimental and Theoretical Principles on Terahertz Generation and Detection

This chapter concerns the coherent generation and detection of ultrafast terahertz (THz) pulses in nonlinear crystals. As these processes rely on nonlinear optical effects driven by intense femtosecond laser pulses, we will first give a description of our laser system and, then, introduce some aspects of nonlinear optics with an emphasis on a second order nonlinear effect, i.e, the phase-matched difference frequency mixing. We exploit this mechanism for the generation of sub-picosecond pulses continuously tunable from a few THz to 40 THz in the nonlinear crystal gallium selenide (GaSe). We refer to these frequencies as the THz range. Afterwards, we will describe the linear electro-optic effect and how it is used for the detection of the THz transients in the nonlinear crystal zinc telluride (ZnTe). Finally we will discuss the generation of ultrafast and high field THz electric transients in the organic crystal DSTMS and their first application in a spectroscopic measurement.

1.1 Ti:Sapphire Laser System

The THz generation is driven by a commercial femtosecond Ti:sapphire (Ti:Sa) amplifier provided by Femtolasers: the system FEMTOPOWER Compact PRO.

	Oscillator [@ 85 MHz]	Amplifier [@ 1 kHz]
Pulse duration	12 fs	25 fs
Spectral width [centered @ 800 nm]	120 nm FWHM	45 nm FWHM
Average output power	420 mW	up tp 1 W
Output pulse energy	5 nJ	up to 1 mJ
Peak power	500 kW	up tp 50 GW

Table 1.1: Specifications of the Ti:Sa oscillator system

It employs a chirped pulse amplification scheme and basically consists of three major parts: stretcher, amplifier and compressor. The system is a multipass amplifier which is seeded by broadband ($\Delta\lambda$ ∼120 nm) ultrashort pulses from a Ti:Sa oscillator. The latter delivers 12 fs pulses with a center wavelength of 800 nm at a 85 MHz repetition rate, with a modelocked output average power of 420 mW. Since the pulse amplification leads to a gain factor of 10^6, it is necessary to decrease the peak power of the pulses from the oscillator, without reducing the pulse energy (∼ 5 nJ), to a level where the damage of the optical components is avoided. This is achieved by letting the pulses pass through a heavy flint glass slab (SF57) before entering the amplifier. In this way the pulses from the oscillator are stretched to about 3 ps. The pulse amplification consists of nine passes through the Ti:Sa amplifier crystal, which is optically pumped by the output of a frequency-doubled Nd:YLF laser emitting at 527 nm at a 1 kHz repetition rate. After the fourth pass, the 85 MHz pre-amplified oscillator pulses are coupled to a KDP Pockels cell system to select a pulse train at 1 kHz. After having passed through the pulse selecting system, the pre-amplified beam is split in two: one is coupled to a second Ti:Sa multipass amplifier by two piezo-controlled mirrors, the other is relaunched into the amplifying crystal of the first amplifier. After the amplification stage, the 1 kHz beam is compressed to about 25 fs. We use a prism in the first and a grating-based compressor in the second amplifier.

Another important instrument, which we have implemented in both amplifiers, is the DAZZLER, an acousto-optic programmable dispersive filter designed by Fastlite. It is an acousto-optic modulator which uses sound waves as a diffraction grating. By tuning the timing, frequency, amplitude and chirps up to the fourth order of the acoustic wave, we are able to shape the spectral phase and

amplitude of the amplifier pulses. The programmable parameters of the two DAZZLER are experimentally tuned in order to optimize the THz generation.

Furthermore, we exploit a minor part of the output beam from the oscillator for detecting the electric field of the THz radiation. To compensate the chromatic dispersion of optical components, which consequently leads to a temporal broadening of the ultrashort oscillator pulses, the oscillator beam is sent onto a couple of chirped dielectric mirrors. Here, the pulses bounce four times back and forth before being coupled to the phase-resolved detection system, which will be presented in the section 1.3.

1.2 Generation of Short THz Pulses with Fixed Carrier-Envelope Phase

So far, several techniques and approaches are available for the generation of THz electromagnetic transients such as synchrotron and free-electron lasers (FEL) emission [1, 18], quantum cascade lasers (QCL) [120, 124, 125], photo-conductive emission, two-colour field-driven gaseous plasmas, optical rectification and difference frequency generation in nonlinear optical crystals. These two latter mechanisms lead to THz pulses with fixed carrier-envelope phase as described below.

In the photo-conductive scheme [29], a biased semiconductor, e.g., GaAs, is illuminated by femtosecond pulses with photon energy above its band-gap. The resulting photon absorption leads to the formation of electron-hole pairs, and the subsequent acceleration of the photo-carriers due to the external DC voltage gives rise to a fast changing photo-current (photo-current surge effect). The fast transient leads to the radiation of THz sub-picosecond electromagnetic waves.

An alternative approach to generate high-field single-cycle THz pulses relies on driving nonlinear processes in centro-symmetric media, e.g., gas plasmas [8–10]. In this scheme, an asymmetric electric field consisting of an amplified Ti:Sa pulse and its second harmonic is tightly focused in air or noble gas. When the laser pulse intensity reaches values of a few TW/cm^2 in the focus, a plasma is generated. The nonlinear interaction between the fundamental and the second harmonic in the laser-generated plasma allows to obtain broadband THz electric fields. Although this method overcomes the disadvantages of damage threshold for the THz sources based on nonlinear crystal, it is not yet mature for widespread applications in nonlinear spectroscopy due to large fluctuations of pulse parameters, mainly pulse energy and beam profile.

A more reliable and simpler technique of generation of broadband THz pulses

exploits difference-frequency generation (DFG) induced by near-infrared (NIR) pulses in crystals without inversion symmetry. In such crystals, a nonlinear polarization generated by two optical input pulses acts as a source radiating sub-picosecond pulses with a frequency content in the THz range. A wide range of materials has been explored. Inorganic crystals, e.g., ZnTe, GaP, $LiNbO_3$ and GaSe, and organic crystals, e.g., DAST, OH1, and DSTMS, were employed to obtain frequencies below 10 THz. Furthermore, GaSe can be used as a source of radiation with frequencies above 10 THz, provided that the NIR pulses used for the generation have a sufficient bandwidth. Since the DFG process is used for all the experiments described in this thesis, it will be discussed in more detail in the next section.

1.2.1 Principles of Nonlinear Optics

The response of matter under the influence of electromagnetic radiation can be described in terms of the polarization $\mathbf{P}$, which, in turn, may generate new electromagnetic waves. In the linear regime of light-matter interaction, the induced polarization $\mathbf{P}$ is proportional to the electric field $\mathbf{E}$ of the incident radiation. For high intensity radiation this approximation is not appropriate anymore. One can express the polarization as a power series in the applied electric field. Often it is worth separating the linear and nonlinear contributions. The total polarization $\mathbf{P}$ is written as:

$$\mathbf{P} = \mathbf{P}^{\mathrm{L}} + \mathbf{P}^{\mathrm{NL}}. \tag{1.1}$$

The linear polarization $\mathbf{P}^{\mathrm{L}}$ rules the phenomena of linear optics. The relation between $\mathbf{P}^{\mathrm{L}}$ and the applied electric field $\mathbf{E}$ is given by

$$\mathrm{P}_i^{\mathrm{L}}(\mathbf{r},\mathrm{t}) = \sum_j \int \chi_{ij}^{(1)}(\mathrm{t}-\mathrm{t}_1)\,\mathrm{E}_j(\mathbf{r},\mathrm{t}_1)\,\mathrm{dt}_1, \tag{1.2}$$

where $\chi^{(1)}$ is a 2-rank tensor and represents the linear susceptibility. The nonlinear contribution $\mathbf{P}^{\mathrm{NL}}$ in a non-centrosymmetric medium contains also the second order and can be expressed as

$$\begin{aligned}\mathrm{P}_i^{\mathrm{NL}}(\mathbf{r},\mathrm{t}) = &\sum_{jk} \int \chi_{ijk}^{(2)}(\mathrm{t}-\mathrm{t}_1,\mathrm{t}-\mathrm{t}_2)\,\mathrm{E}_j(\mathbf{r},\mathrm{t}_1)\,\mathrm{E}_k(\mathbf{r},\mathrm{t}_2)\,\mathrm{dt}_1\mathrm{dt}_2 \\ &+ \text{higher orders}\end{aligned} \tag{1.3}$$

where $\chi^{(2)}$ is a 3-rank tensor and represents the second-order nonlinear susceptibility responsible for sum and difference frequency generation.

Using the nonlinear polarization the wave equation for the electric field is

$$\nabla \times \nabla \times \mathrm{E} + \frac{\epsilon^{(1)}}{c_0^2}\frac{\partial^2 \mathrm{E}}{\partial t^2} = -\frac{1}{\epsilon_0 c_0^2}\frac{\partial^2 \mathrm{P_{NL}}}{\partial t^2} \tag{1.4}$$

where $\epsilon^{(1)} = 1 + \chi^{(1)}$ is the relative permittivity of the material. The wave equation (1.4) shows the key role which is played by the nonlinear polarization as a source term. Whenever the term $\partial^2 \mathrm{P_{NL}}/\partial t^2$ is non-vanishing, charges are being accelerated, and it is known that accelerated charges are sources of electromagnetic radiation.

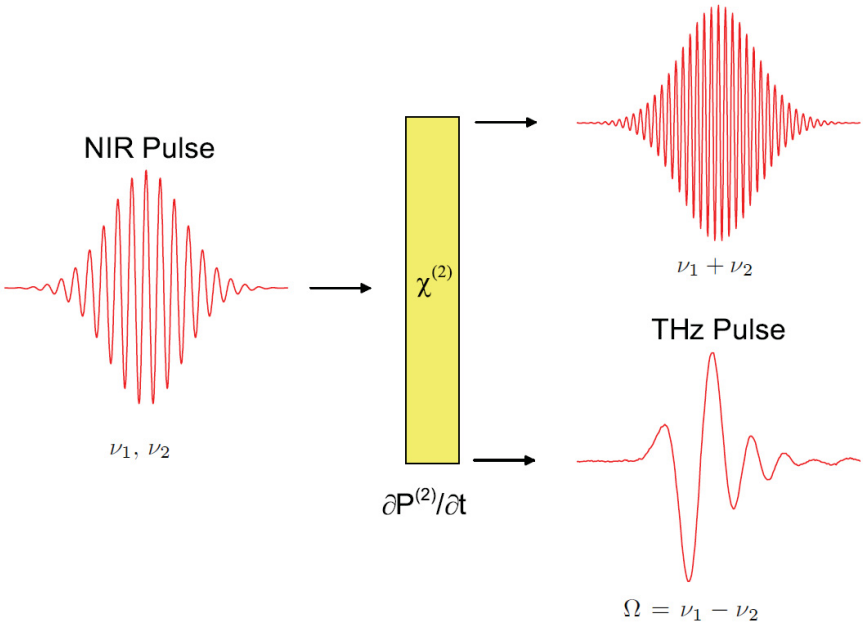

Figure 1.1: Each frequency pair ν_1, ν_2 of the field E drives a time-dependent nonlinear polarization at sum and difference frequencies in a $\chi^{(2)}$ nonlinear crystal. For ultrashort NIR pulses, the nonlinear polarization components with sum and difference frequencies are respectively in the visible or ultraviolet range and THz range.

Starting from Eq. 1.3, the mechanism of DFG is described in the frequency domain by a nonlinear polarization of the form

$$\mathrm{P}_i^{(2)}(\Omega) = \sum_{jk} \int_{\mathrm{spectr}} d\nu \chi_{ijk}^{(2)}(\Omega; \nu_1, \nu_1 - \Omega)\mathrm{E}_j(\nu_1)e^{i\phi_{\mathrm{CEP}}}\mathrm{E}_k^*(\nu_1 - \Omega)e^{-i\phi_{\mathrm{CEP}}} + \text{c.c.} \tag{1.5}$$

Here, ϕ_{CEP} is the carrier-envelope phase (CEP) of the 800 nm pulses. As schematically illustrated in Fig. 1.1, a nonlinear polarization is generated at a frequency $\Omega = \nu_1 - \nu_2$ for each frequency pair ν_1, ν_2 which has a detuning $\Delta\nu = \Omega$. For the femtosecond NIR pulses from our Ti:Sa amplifier whose spectrum is depicted in Fig. 1.2, the detuning covers a frequency range up to several tens of THz. The highest frequency Ω which could be generated via difference-frequency mixing is approximately 60 THz. Most importantly, according to Eq. 1.5, such a mechanism allows for generating THz pulses with a locked CEP although the internal phase of the 800 nm pulses, i.e., the relative phase shift between the peak of the envelope and maximum of the carrier, might change from shot-to-shot. As a result, the THz electric-field profile is the same for each shot.

The spectral shape and central frequency of THz pulses generated by difference frequency mixing depend on the dispersion of the second-order nonlinear susceptibility $\chi^{(2)}$, the transmission range of the nonlinear crystal, the bandwidth of the excitation NIR pulse and the phase mismatch between the NIR and THz pulses co-propagating through the crystal. The latter is removed by phase-matching schemes and the THz waves coherently generated in different locations are all in phase at the end of the nonlinear crystal, i.e., constructively interfere. The phase-matching condition reads:

$$\Delta k \equiv k_{THz}(\Omega) - [k_{NIR}(\nu) - k_{NIR}(\nu - \Omega)] = 0 \tag{1.6}$$

Since the THz frequencies are much smaller than the NIR frequencies and the NIR spectral components are approximately equal to the central frequency ν_c, the phase-matching condition (1.6) can be expressed by :

$$\Delta k \approx k_{THz}(\Omega) - \Omega \left(\frac{dk_{NIR}}{d\nu} \right)_{\nu=\nu_c} = \frac{\Omega}{v_\varphi(\Omega)} - \frac{\Omega}{v_g(\nu_c)} \tag{1.7}$$

which means that phase-matching is achieved when the phase velocity $v_\varphi(\Omega)$ of the THz wave matches the group velocity $v_g(\nu_c)$ of the NIR wave. For $\Delta k \neq 0$, the coherence length, i.e., the interaction length over which the NIR wave and newly generated THz waves are in phase, is given by

$$l_{coh} \equiv \pi/\Delta k = \frac{c}{2\Omega|n(\Omega) - N_g(\nu)|} \tag{1.8}$$

where c is the speed of light in vacuum, n and N_g the refractive and group refractive indices, respectively.

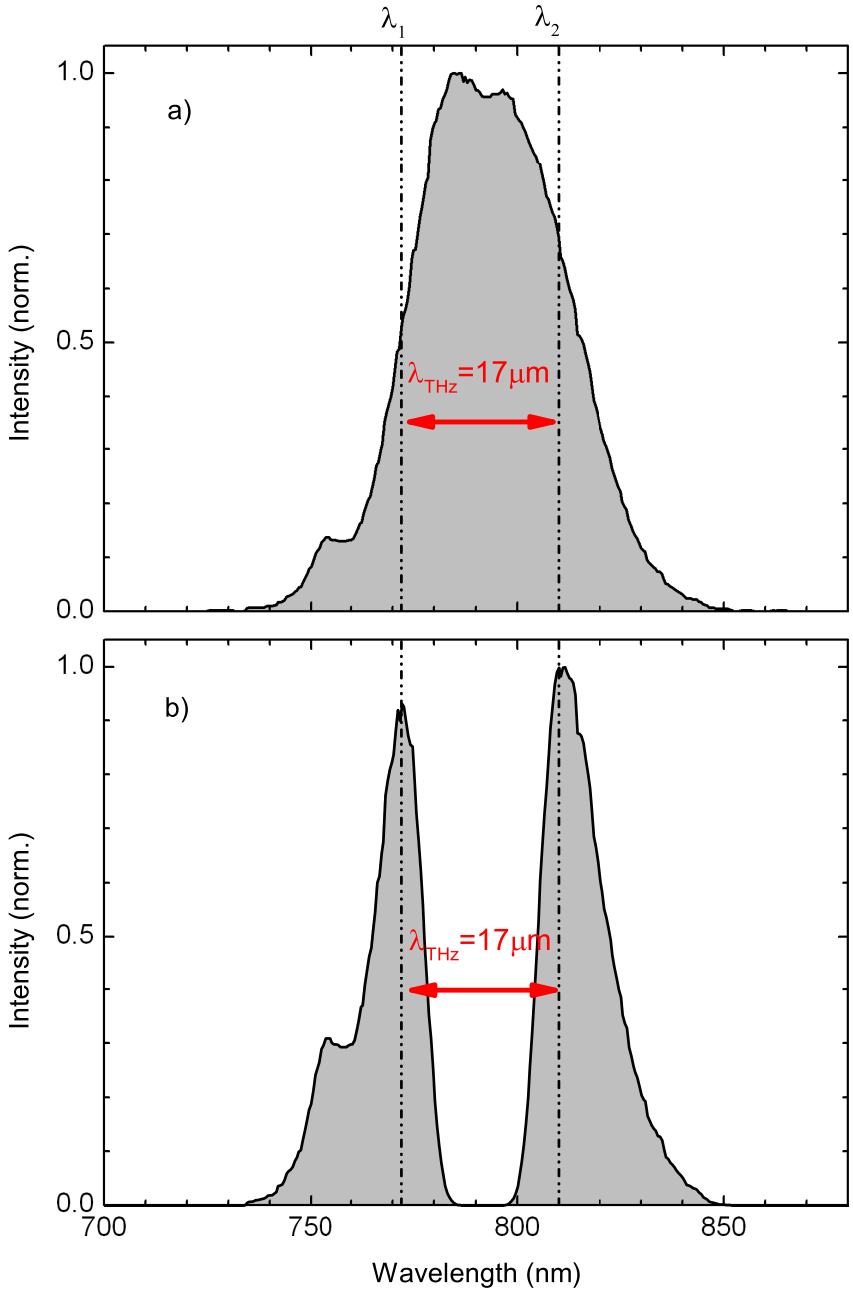

Figure 1.2: (a) Spectrum of the NIR pulses from the Ti:Sa amplifier without the pulse shaper. (b) Spectrum of NIR pulses, tailored to enhance the DFG for generating THz transients at the central wavelength $\lambda_{THz} = 17$ μm ($\nu_{THz} \simeq$ 18 THz)

1.2.2 Phasematched Difference Frequency Mixing in GaSe

GaSe is a birefringent crystal (n_o = 2.883 and n_{eo} = 2.502 [88], being the ordinary and extraordinary refractive indices at 0.8 μm respectively) especially suitable for converting NIR pulses into light with frequencies up to the THz range under phase matching conditions, due to its wide transmission range in the near-infrared and THz spectral range and the exceptionally strong second-order nonlinearity (54 pm/V).

The NIR pulses provided by the Ti:Sa amplifier system are employed to generate THz pulses. Here, we present a scheme relying on phase-matched type I difference frequency mixing of frequency components from the broad spectrum of a single near-infrared pulse in a GaSe crystal. However, the DFG is not efficient for the generation of THz pulses with frequencies above 10 THz since in this case the mixing process involves only the spectral wings of the near-infrared pulse. To circumvent this problem, with the help of the pulse shaper in our setup we enhance the amplification of the spectral wings by filtering out the central spectral components of the NIR pulses after the pre-amplification (cf. Fig. 1.2). We set the width of the central dip in such a way that the central frequencies of the low and high wings are detuned by the THz frequency ν_{THz} which we need to generate for driving our experiments.

To satisfy type I phase matching within the spectrum of a single near-infrared pulse, it is required to cross polarize the pulse spectral wings in such a way to be the ordinary and extraordinary polarization components while traveling through the GaSe crystal. For this purpose, we exploit the birefringence of an uniaxial (001)-oriented MgF_2 plate. Figure 1.3 illustrates the generation geometry in our setup. Passing through the MgF_2 plate, the NIR beam is split into two waves. Light polarized perpendicular to the plane containing the propagation vector k and the optical axis is the ordinary wave. Such light experiences a refractive index n_o. Light polarized in the plane containing k and the optical axis is the extraordinary wave and experiences a refractive index $N_{eo}(\theta^{int})$, which depends on the internal tilt angle θ^{int} between k and the optical axis according to the relation

$$\frac{1}{N_{eo}^2(\theta^{int})} = \frac{\sin^2\theta^{int}}{n_{eo}^2} + \frac{\cos^2\theta^{int}}{n_o^2} \tag{1.9}$$

where n_{eo} is the principal value of the extraordinary refractive index, and θ^{int} is connected to the external tilt angle θ_{MgF_2}. After having traveled the full thickness of the plate , the two waves accumulate a phase retardation given by:

$$\gamma(\lambda, \theta_{MgF_2}) = \frac{2\pi d}{\lambda}\sqrt{n_o^2 - \sin^2\theta_{MgF_2}}\left(\sqrt{\frac{1 - n_{eo}^{-2}\sin^2\theta_{MgF_2}}{1 - n_o^{-2}\sin^2\theta_{MgF_2}}} - 1\right) \tag{1.10}$$

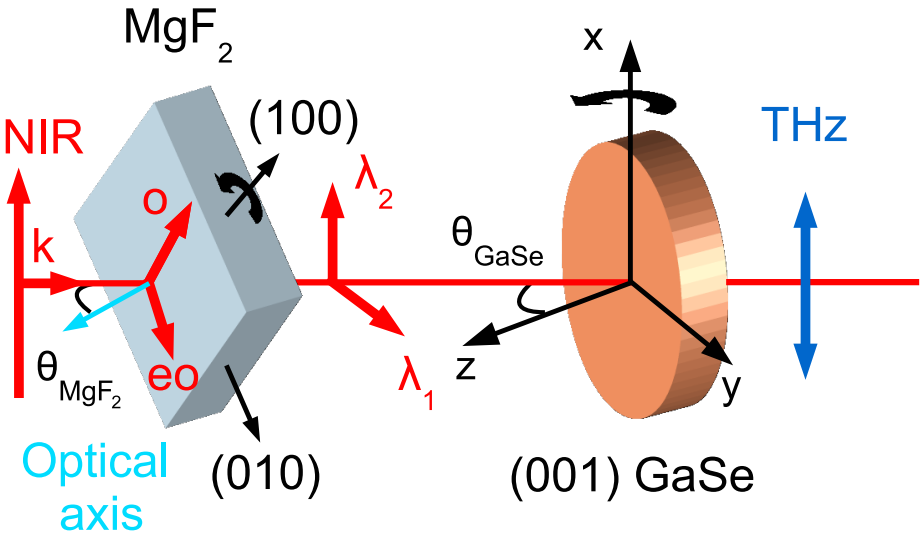

Figure 1.3: Experimental geometry to generate tunable THz pulses via type I phasematched difference frequency mixing in a 100 μm thick (001)-GaSe crystal. The birefringent MgF_2 plate imposes a frequency-dependent phase-shift on the different spectral components of the NIR pulse in such a way that the polarization of the spectral wing at λ_1 is rotated by 90°. Adjusting the phasematching angle θ_{GaSe} allows to tune the frequency of the generated THz pulse.

As the indices of refraction n_o and n_{eo} are almost constant in the frequency range covered by the spectrum of the NIR pulse [28] (1.37 and 1.38, respectively), the phase retardation γ is inversely proportional to the wavelength λ. By appropriately tilting the MgF_2 with respect to the propagation of the incident NIR beams, it is possible to achieve phase retardations $\gamma(\lambda_1) = 2\pi(N + 1/2)$ and $\gamma(\lambda_2) = 2\pi N$, where N is an integer number. As a result, the low and high spectral wings are cross polarized. To use the birefringence of the MgF_2 crystal, the plate is placed in the NIR beam as follows: starting with the optical axis parallel to the wave vector $\mathbf{k}$, the MgF_2 plate is first rotated by 45° around the optical axis and then by φ around the (100) direction. In this geometry, at the end of the plate the electric field is given by:

$$E(\lambda) = E_o\hat{o} + E_{eo}e^{i\gamma(\lambda)}\hat{eo} \tag{1.11}$$

where $\hat{o}$ and $\hat{eo}$ are the unit vectors of the ordinary polarization and the extraordinary polarization, respectively. Both components enclose an angle of 45° with

the polarization of the NIR pulse. For the high spectral wing, the electric field is given by $E(\lambda_2) = E_o\hat{o} + E_{eo}\hat{eo}$, parallel to the polarization of the NIR pulse. For the low spectral wing, the electric field is given by $E(\lambda_1) = E_o\hat{o} - E_{eo}\hat{eo}$, perpendicular to the polarization of the NIR pulse. Such cross polarized components drive the DFG process inside a (001)-GaSe crystal. The latter is an uniaxial hexagonal crystal displaying a $\bar{6}m2$ symmetry. Accordingly, the only nonvanishing tensor elements of the second-order susceptibility correspond to the indices $yyy = -yxx = -xxy = -xyx$.

The incident beam propagates in the xy-plane of the GaSe crystal. By rotating the crystal around the x-axis, the phase-matching conditions in the GaSe are changed and THz pulses are generated at different central wavelengths. The DFG occurs among the cross-polarized components within the spectrum of a single near-infrared pulse.

The generation of THz radiation at frequencies below 10 THz via DFG is obtained by exploiting all the spectrum of the NIR pulse shown in Fig. 1.2(a). The MgF_2 plate is removed from the setup and the NIR pulse impinges perpendicularly onto the GaSe crystal. The characterization of THz pulses via electro-optic sampling is discussed in the next section.

1.3 Phase-Resolved Detection by Electro-Optic Sampling

Electro-optic (EO) sampling represents a powerful technique for directly measuring the amplitude and phase of the electric field of sub-picosecond THz pulses. This method exploits another $\chi^{(2)}$ nonlinear process, the linear EO effect, also known as the Pockels effect. The ultrafast modulation of the index of refraction, induced by a THz electric field in a non-centrosymmetric crystal, is read-out by a short probe optical pulse.

Its high electro-optic coefficient and its proper transmission property in the near-infrared and THz spectral range make the ZnTe an excellent sensor for broadband coherent THz detection by EO sampling.

Figure 1.4 illustrates the detection part in our setup. A linearly polarized NIR probe beam is tightly focused by a parabolic mirror (PM) onto a ZnTe crystal, through which it propagates collinearly with the THz beam. The birefringence induced by the THz electric field changes the state of polarization of the probe pulse. Therefore, upon THz irradiation the ZnTe acts as a waveplate which imposes on the polarization components of the probe pulse a phase retardance $\Delta\Gamma$ proportional to the instantaneous THz electric field. For a (110)-

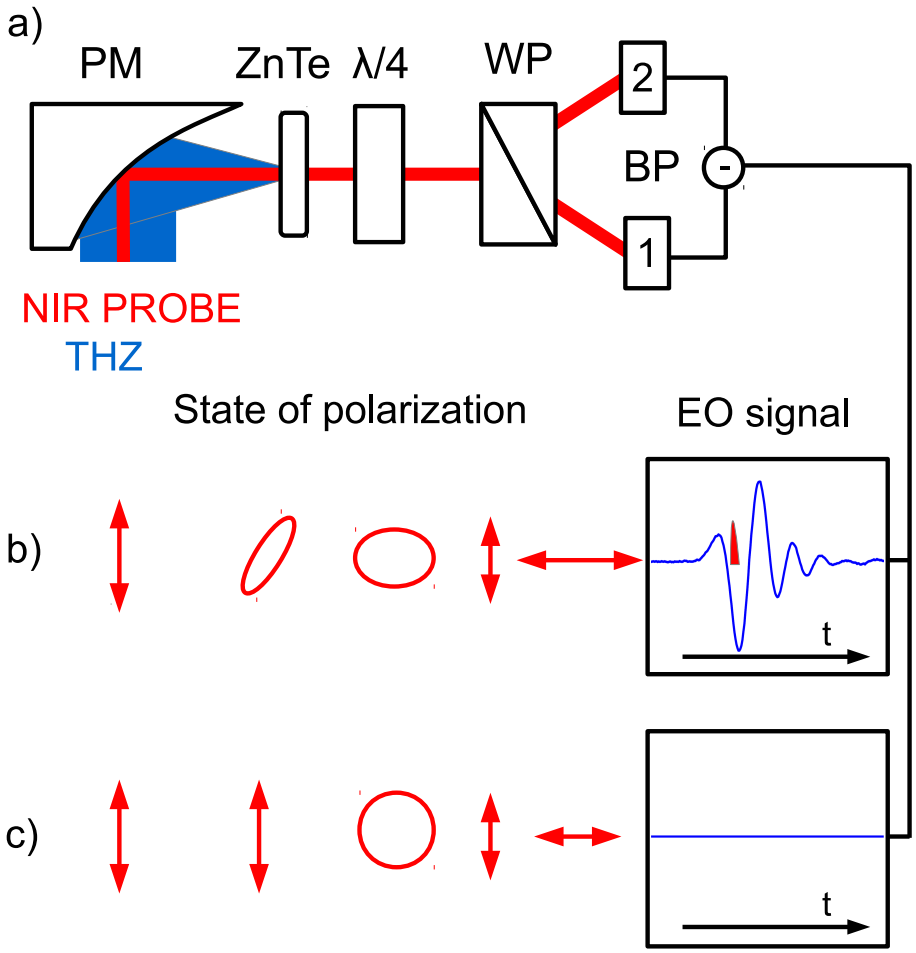

Figure 1.4: a) Experimental setup for phase-resolved detection of THz electric field by using electro-optic sampling: the THz electric field induces a birefringence which affects the polarization of the sampling pulse. The electro-optic modulation induced by the ultrafast Pockels effect is detected by a $\lambda/4$ waveplate, a Wollaston prism and a couple of balanced photodiodes. b), c) Evolution of the polarization with and without the presence of the THz pulse in the ZnTe. By varying the time delay t between the probe and the THz pulses the temporal waveform of the THz electric field is sampled.

oriented ZnTe crystal, the optimum for EO detection is achieved when the linear polarization of the probe beam is perpendicular or parallel to the direction of the THz polarization. With the THz pulse polarized along the (001) direction of the ZnTe crystal, the phase retardance is given by:

$$\Delta\Gamma = \frac{2\pi d}{\lambda} n_0^3(\lambda) r_{41} E_{THz} \tag{1.12}$$

where λ stands for the probe wavelength, n_0 for the index of refraction without THz field, d for the thickness of the crystal and r_{41} (3.9×10^{-10} cm/V) for the non-vanishing component of the ZnTe EO tensor **r**.

The ultrafast modulation of the probe polarization state is analyzed by a combination of a $\lambda/4$ waveplate ($\lambda/4$), a Wollaston prism (WP), a couple of balanced photodiodes (BP) and a delay stage. The $\lambda/4$ waveplate introduces an additional phase retardance of 45° between the polarization components of the probe pulse, thereby allowing to distinguish the sign of the THz electric field. The WP splits the probe beam into horizontally and vertically polarized components, whose intensities are measured by two balanced photodiodes. The resulting differential intensity, normalized to the total intensity of the probe, is given by

$$\frac{\Delta \mathrm{I}}{\mathrm{I}_1 + \mathrm{I}_2} = \sin \Delta\Gamma \approx \Delta\Gamma \tag{1.13}$$

For a moderate modulation, the differential intensity is proportional to the THz electric field. The typical modulation is $10^{-2} \sim 10^{-4}$.

There are several factors which affect the sensitivity at which the THz electric field is detected in the ZnTe. These include the strong dispersion in both the refractive index and absorption in the THz range and the frequency dependence of the electro-optic coefficient r_{41}. The very strong TO phonon resonance at 5.3 THz leads to a wide absorption band in the range of 4–6 THz (reststrahlen band). Another crucial aspect is the matching between the group velocity of the NIR probe pulse and the phase velocity of the THz pulse. In case of mismatching, the THz electric field will be averaged since the probe pulse samples several parts of the THz pulse. Consequently, the time resolution decreases, which in turn limits the detectable THz frequencies. It is not possible to achieve a broadband velocity matching over all the THz range due to dispersion. The lower frequencies in the THz range undergo less velocity mismatch than the higher ones. To reduce the effects of phase-mismatching, one has to choose a ZnTe thickness comparable to the coherence length. We use a 300 μm-thick ZnTe crystal for detecting THz pulses centered at frequency below the reststrahlen band, whereas for frequency above it we use a 10 μm-thick ZnTe piece. In the latter case, the detection bandwidth is approximately 30 THz. A (100)-ZnTe substrate of 300 μm thickness is attached to the thin EO active ZnTe to prevent Fabry-Perot effects .

We use the ultrashort pulses from the oscillator instead of the pulses from the amplifier as sampling pulses for two main reasons: first, their duration of 12 fs

allows to detect frequency up to 40 THz; second, by using an electronic gate technique, the differential signal ΔI related to the oscillator pulse synchronized to the THz pulse is compared with the one from the previous oscillator pulse not affected by the THz pulse. In this way, we can reduce the fluctuations of the electro-optic signal. Typical THz electric field transients are shown in figure 1.5 (a), (b). The two THz pulses last 500 fs and 150 fs (calculated as FWHM of the intensity) and are centered at 2 THz and 23 THz, respectively [see Figs. 1.5 (c), (d) for the respective spectral densities]. We determine the amplitude of the THz electric field by inverting the equation (1.13) and taking into account the transmission of the electric field through the ZnTe surface. This yields a value of about 150 kV/cm for the electric field strength, which is high enough for driving nonlinear processes in our experiments beyond the perturbative regime.

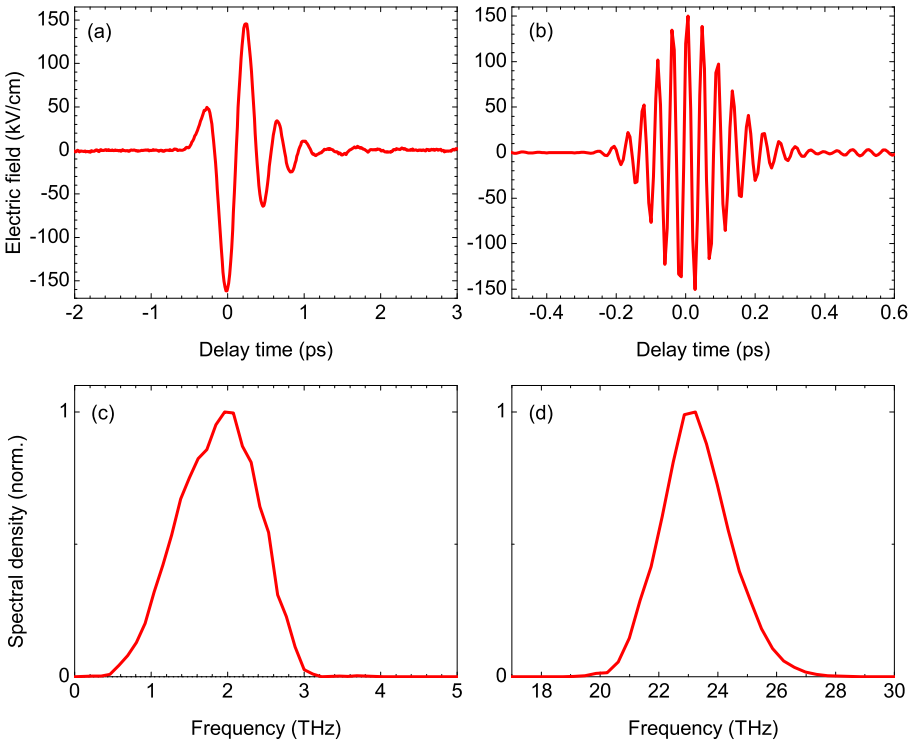

Figure 1.5: (a), (b) Transient electric field as a function of the delay time between the THz and near-infrared probe pulses. The delay zero is defined by the maximum of the transients. Both transients were generated in a 200-μm-thick GaSe crystal but for different phase-matching angles (0° and 48°, respectively) and different incoming near-infrared spectra. (c), (d) Power spectral density for the respective transients.

1.4 Ultra-broadband THz Generation in the Organic Crystal DSTMS

As described in Sec. 1.2, the most widespread scheme for the generation of broadband pulses is based on phase-matched difference frequency mixing. In such a scheme, the THz bandwidth is mostly limited by the phase-matching bandwidth, which is related to the mismatch between the phase velocity of the generated THz wave and the group velocity of the pumping wave [56]. Recently, non-centrosymmetric organic crystals have attracted great interest for the variety of applications in nonlinear optics such as second-harmonic generation of near-infrared light, electro-optic light modulation, and optical parametric oscillation [12]. Moreover, they have gained interest in the THz community due to their particularly high second-order nonlinearity [24, 94, 107, 113]. Extensive studies [16, 106, 127] have demonstrated the use of organic crystals as very efficient THz emitters. A prototype material is the stilbazolium derivative 4-N,N-dimethylamino-4'-N'-methylstilbazolium 2,4,6-trimethylbenzene sulfonate (DSTMS), which is composed of a chromophore stilbazolium cation that possesses a large molecular optical nonlinearity, and a sulfonate anion that leads to a non-centrosymmetric packing in the crystalline phase [67, 83]. With ultrashort pumping pulses of center wavelengths of 1.2, 1.5, or, recently, 0.8 μm, broadband single-cycle THz pulses with electric-field amplitude of up to MV/cm and spectral content of up to 11 THz have been generated in DSTMS by difference frequency mixing between the frequency components of the input pumping spectrum under phase-matching conditions [91, 104, 117, 118]. Furthermore, difference frequency generation of two ns pulses has been exploited in DSTMS for producing monochromatic THz waves over a widely tunable frequency range up to 20 THz [85]. Here, we demonstrate the generation of high-field ultrashort pulses with ultra-broadband spectra from 0.5 to 30 THz in the DSTMS crystal by difference frequency mixing within the spectrum of 800 nm pulses and elucidate the role of phase-matching. The result of a first spectroscopic application of DSTMS will be also discussed.

Experiment

The output beam of the Ti:Sa amplifier, which delivers 25 fs pulses with a center wavelength of 800 nm at a 1 kHz repetition rate, and pulse energies of up 1 mJ, pumps a 380-μm-thick DSTMS crystal for driving difference frequency mixing of spectral components within the pulse spectrum (see Fig. 1.6). To prevent optical damage in the DSTMS crystal [91], the pulse energy is reduced

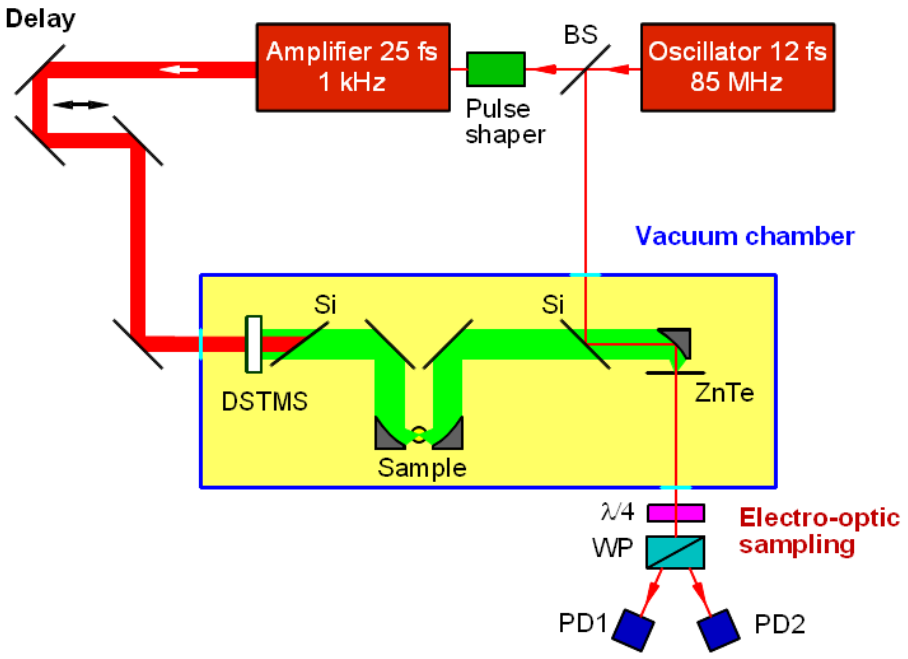

Figure 1.6: Schematic view of the experimental setup for ultra-broadband THz spectroscopy. Intense THz electric field are generated via difference-frequency mixing in DSTMS of intense 25 fs pulses stemming from an amplified Ti:Sa laser system, and detected by electro-optic sampling in a thin ZnTe crystal. A pulse shaper serves to optimize the THz generation by adjusting the spectral components of the pulses coming out of the oscillator. The THz source, the sample and the electro-optic sensor are placed in a vacuum chamber at a pressure of 10^{-6} mbar.

to 200 μJ, corresponding to a peak intensity of 100 GW/cm^2. The pump beam with a spot of 3 mm diameter is sent onto the a-b crystal surface under normal incidence. The polarization of the pump pulses is parallel to the a axis, so that the nonlinear coefficient d_{111} is exploited for the THz generation. After traveling through the nonlinear organic crystal, the 800-nm beam is blocked by a silicon wafer. The generated THz pulses are polarized along the a axis and detected by EO sampling in a 10-μm-thick ZnTe crystal using 12-fs pulses from the oscillator of the Ti:sapphire laser system. Both the generation and the detection take place in vacuum for preventing THz absorption by the water vapor present in air [116]. An acoustic-optic pulse shaper is employed for tailoring the spectrum of the oscillator pulses feeding the amplifier in order to achieve both the highest electric-field amplitude and the widest spectrum of the generated THz radiation.

Results

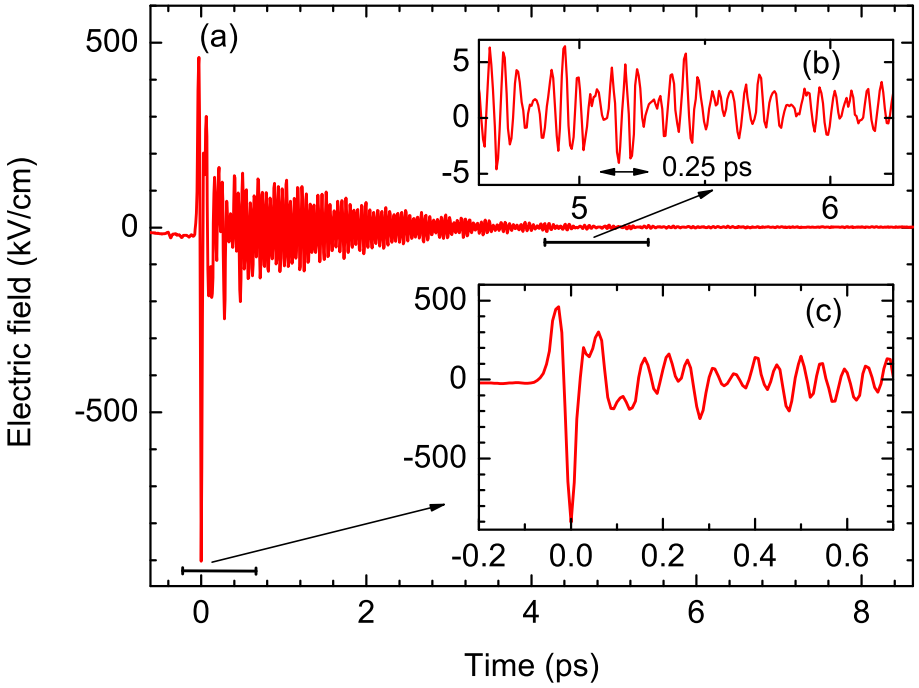

Figure 1.7: (a)-(c) Electric field profile of the THz pulse generated in the DSTMS crystal and fully phase-resolved by EO sampling. (b) and (c) are enlargements of selected time ranges.

Figures 1.7(a)-(c) show the time evolution of the electric field emitted by the DSTMS crystal. It exhibits a short initial peak with an absolute value of 900 kV/cm and a subsequent long-lived component with an initial amplitude of approximately 300 kV/cm that is damped on time scale of about 4 ps. At late times, a beating with a period of 0.25 ps is observed [see Fig. 1.7(b)]. The spectrum derived by Fourier transform of the generated electric field is presented in Fig. 1.8(a) and covers an extraordinarily wide frequency range between 0.5 and 30 THz. It displays several bands from reabsorption of the generated light. Additionally, the ultra-broadband spectrum contains two spectrally narrow lines at 16.7 and 20.7 THz, both with a width of 0.27 THz. These two pronounced spectral features cause the beating observed at late times, which persists on a picosecond time scale. We have performed additional measurements exploiting a 100-μm-thick GaP crystal (reststrahlen band 7-9 THz) as EO sensor, since the ZnTe crystal does not allow for measuring the frequency range 4–6 THz due to its reststrahlen band. As shown in Fig. 1.8(b), the emitted spectrum has no

gap between 4 and 6 THz. The EO coefficient of the GaP crystal has a strong optical phonon contribution leading to different values for frequency above and below the reststrahlen band [82]. Additionally, due to the large thickness of the crystal, the frequency response is limited up to 7 THz. As a result, the spectral power density drops down for frequencies above this value.

Discussion

The generated ultra-broadband pulses undergo reabsorption due to numerous vibrational bands of the DSTMS crystal. For an analysis, we calculate the reabsorption losses over the coherence length [dashed line in Fig 1.8(a), calculated according to Eq. 1.8], instead of the thickness of the crystal, and the infrared absorption data from [24]. The latter work refers to spectroscopic measurements on 4-N,N-dimethylamino-4'-N'-methylstilbazolium tosylate (DAST), which has a composition similar to DSTMS [106]. For a frequency below 4 THz, two strong resonances at 1 and 3 THz lead to losses of more than 99% and 40%, respectively. For frequencies between 6 and 16 THz, the reabsorption leads to losses on the order of 50% at the maxima of vibrational bands; it is negligible between the maxima. Consequently, the spectral power rises as the frequency increases. The pronounced spectral components in the emission spectrum at 16.7 and 20.7 THz stem from molecular vibrations of the system. Due to the low symmetry of the DSTMS crystal structure, most vibrations are both Raman and infrared active. As a result, the 800 nm pumping pulses drives a polarization on the $v = 0 \rightarrow 1$ transition responsible for the narrow lines via a Raman process. Such a polarization gives rise to coherent infrared emission [105]. The slow vibrational dephasing results in the long-persisting beating in the picosecond time domain. However, this issue is not fully clear and the two strong emission features may alternatively be caused by resonances in the second-order susceptibility. Therefore, further detailed studies are required. In the next paragraph, we address the importance of phase-matching for the THz generation in the DSTMS crystal.

Relevance of phase-matching

As shown in Fig. 1.8(a), the coherence length is shorter than the crystal thickness of 380 μm for frequencies above 0.7 THz. Accordingly, one would expect a minor THz emission at higher frequency. For example, one would need a DSTMS crystal with a thickness of 10 μm to efficiently generate the strong component at 20.7 THz by phase-matched difference- frequency mixing. Therefore, the following question arises : does phase-matching really play a role in the broadband generation process? To address this issue, we have performed

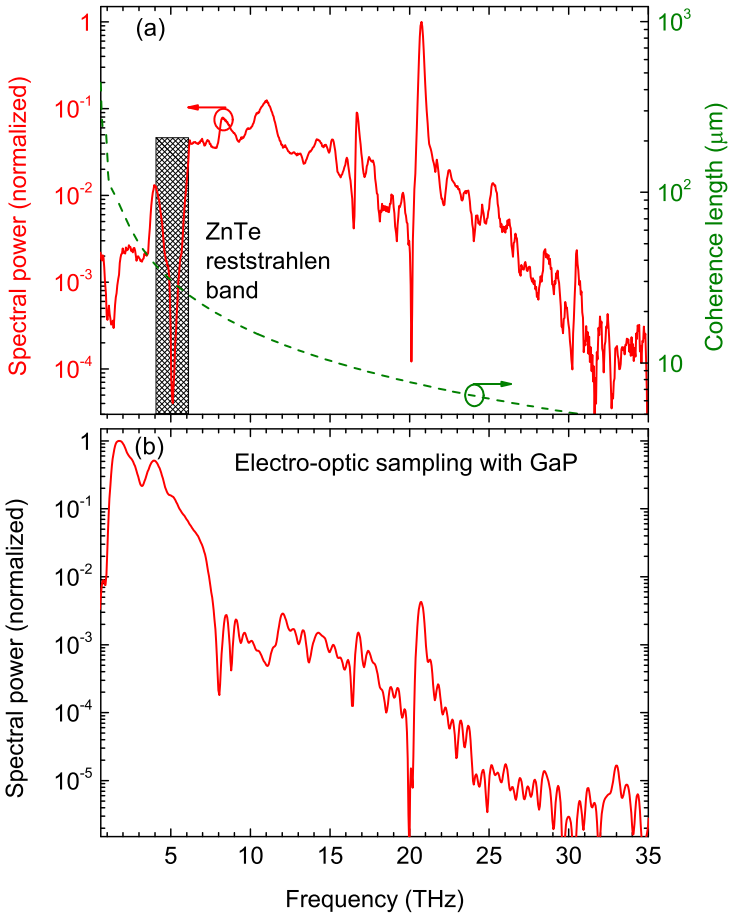

Figure 1.8: (a) Solid line, spectral power density of the THz pulse generated in the DSTMS crystal, measured with a spectral resolution of 0.05 THz. The marked region in the frequency range between 4 and 6 THz depicts the reststrahlen band of ZnTe. Dashed line, coherence length for difference-frequency mixing calculated according to Eq. 1.8. The index of refraction in the near infrared range is taken from [94], whereas the index of refraction in the THz range is calculated from the data in the works [24, 113] by using a Lorentz-oscillator model. Despite numerous absorption bands, the THz index of refraction remains essentially constant at value 2.22 for frequency above 2.2 THz with modulations $\Delta n \leq 0.1$ in correspondence of vibrational resonances. As a result, the coherence length does not display any modulation at the absorption bands. (b) Emitted spectrum from the DSTMS crystal measured by electro-optic sampling in a GaP crystal.

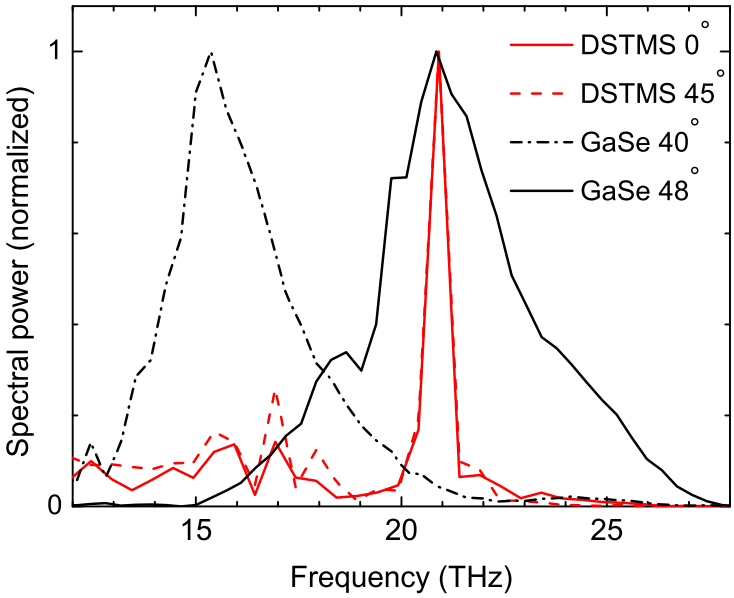

Figure 1.9: Spectral power density of the THz pulses emitted from DSTMS for normal (0°) incidence, for incidence under 45°, and of the THz pulses from a 100-μm-thick GaSe crystal under 40° and 48°.

measurements under different incidence angles, and then compared the emitted spectra from DSTMS to the spectra generated with a GaSe crystal with a thickness of 100 μm under identical experimental conditions. As shown in Fig. 1.9, the phase-matched difference-frequency generation in GaSe leads to both an evident shift of the spectrum with the angle and a spectral width narrower than the spectrum generated in DSTMS. In contrast, the spectrum of the pulses emitted from DSTMS weakly depends on the angular orientation. Such behavior suggests that difference frequency generation in DSTMS is not strongly influenced by phase matching allowing for the ultra-broadband spectrum generated. Additionally, although the coherence length in DSTMS is substantially shorter than the phase-matched interaction length of 100 μm in the GaSe crystal for frequency above 2 THz, the two crystals emits pulses with electric-field amplitudes of the same order of magnitude. This results from the fact that DSTMS displays a larger second-order nonlinearity ($d_{111} = 214 \pm 20$pm/V [94]), compared to GaSe (86 ± 17 pm/V [32]).

Ultra-broadband spectroscopy on DAST

The ultra-broadband THz pulses [Figure 1.7(a)], generated in the DSTMS crystal are tightly focused by an off-axis parabolic mirror onto a DAST crystal with

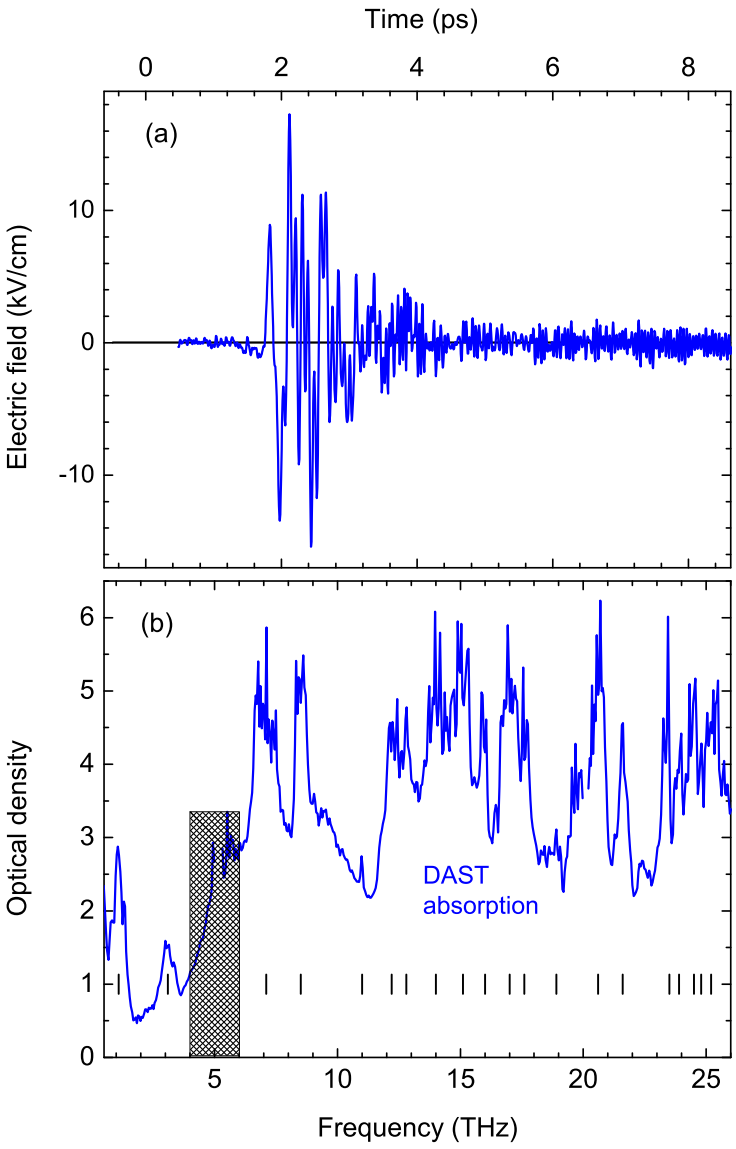

Figure 1.10: (a) Electric field transient transmitted through a 0.445-mm-thick DAST crystal. (b) Optical density ($OD = -\log_{10} T$) of the DAST crystal (T: transmission). In the spectral range 4 and 6 THz, the data are not reliable because of the reststrahlen band of the ZnTe. The vertical lines represent the frequency at which vibrational absorption occurs.

a thickness of 0.445 mm. The DAST crystal is oriented in a way that the electric field of the incident pulses is parallel to its a axis. The electric field of the transmitted pulses is fully phase-resolved by EO sampling in the ZnTe crystal. As shown in Fig 1.10, the peak amplitude of the incident electric field is re-

This work	[24]	This work	[119]	This work	[119]
1.1	1.1	14.0	14.1	20.7	20.5
3.1	3.1	14.7	14.5	21.6	21.7
7.1	7.0	15.1	15.0	23.5	
8.5	8.4	16.0	16.1	23.9	
11.0	11.0	16.4	16.5	24.5	24.5
12.2	12.3	16.9	17.0	24.8	24.8
12.8		17.7		25.2	
		18.9	18.7		

Table 1.2: Frequencies of absorption lines in DAST (in THz) in the frequency range 0–25 THz from the present work (experimental uncertainty ±0.1 THz), compared with absorption data from [24, 119].

duced to a strength of about 17 kV/cm. Apart from reflection losses, which we have estimated to be on the order of 30%, the reduction in amplitude is mainly caused by the vibrational bands of the crystal in the frequency range covered by the broadband incident pulse [24, 119]. Comparing the spectrum of the incident and transmitted pulses, we have calculated the optical density (OD) shown in Fig 1.10(b). The measurements show that our setup enables to measure absorption at least up to an OD of 6. The OD displays several absorption peaks due to vibration transitions. The vibrational frequencies obtained are summarized in Tab. 1.2 and in full agreement with absorption data from former works [24, 119].

Chapter 2

Phase-Resolved Two-Dimensional Nonlinear THz Spectroscopy

Femtosecond two-dimensional (2D) optical spectroscopy has proven to be one of the most powerful diagnostic tools among the nonlinear ultrafast spectroscopic techniques, being capable, for example, to monitor the temporal evolution of elementary excitations and to identify correlations among them at the same time [55, 93]. Due to its versatility, it has been extensively applied on various systems, namely molecules of chemical and biological interest [43, 51, 98], light-harvesting complexes [14], nanostructured and bulk semiconductors [59], and atomic vapors [25]. In the infrared and visible frequency range the 2D spectroscopy has yielded prominent insight on formation and breaking of hydrogen-bonds in molecule-water systems [30, 31, 70], protein-folding processes [22], the role of the electric-field shielding played by water at the interface with DNA [42], vibrational, electronic and excitonic couplings [51], formation and dissociation of solute-solvent complex [130], charge and energy transfer processes in complex molecules, nanotube thin films, and photosynthetic complexes [21].

A novel approach for 2D spectroscopy in the THz frequency range has been recently implemented. It is based on a collinear interaction geometry of a sequence of two phase-locked THz pulses interacting with the sample [78]. First applications of this approach have provided insight in nonlinear charge transport in graphene and in quantum coherent intersubband Rabi flopping in multiple quantum wells [13, 79]. Two-colour 2D THz spectroscopy has demonstrated its potential for coherent quantum control of light [34]. In Sec. 2.1, an introduction

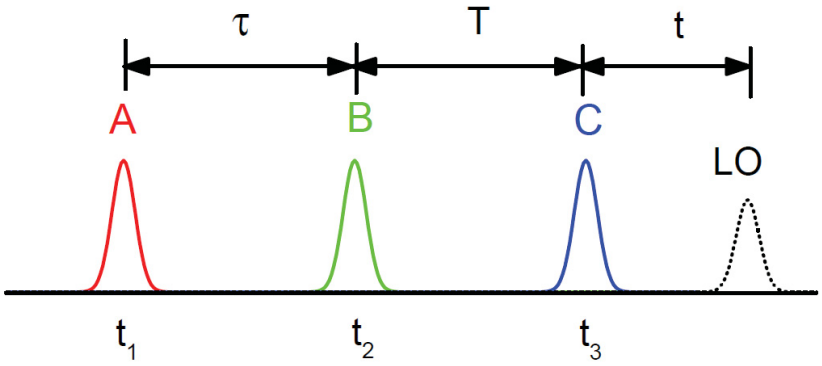

Figure 2.1: Timing sequence of three pulses A, B and C used in a 2D spectroscopy. Pulses A and B are separated by the coherence time τ, and pulses B and C by the waiting time T. The local oscillator (LO) pulse is delayed by the detection time t from the last pulse C.

to the theoretical background and methods of 2D IR/Vis spectroscopy is given. In Sec. 2.2, an extension of 2D THz spectroscopy to sequences of three pulses is presented.

2.1 2D IR/Vis Spectroscopy

2.1.1 Theoretical background

2D optical spectroscopy originates conceptually from multidimensional nuclear magnetic resonance (NMR), first demonstrated by the Ernst group in 1976 [5]. In 2D NMR spectroscopy, the structures and dynamics of molecular systems are studied by probing nuclear spin transitions and their correlations with a sequence of radio frequency pulses. In contrast to 2D NMR, 2D optical spectroscopy has been widely exploited to address the third-order nonlinear response of matter employing, e.g., photon-echo or four-wave mixing techniques. In such experiments, three pulses A, B and C with electric fields E_A, E_B and E_C, wavevectors k_A, k_B and k_C and frequencies ν_A, ν_B and ν_C interact with the sample at the times t_1, t_2 and t_3 and induce a third-order nonlinear polarization

$P^{(3)}$ resulting in the emission of the nonlinear electric field E_S. The third-order nonlinear polarization is expressed as a convolution of the nonlinear response function $S^{(3)}$ with the three electric fields [92]. $S^{(3)}$ carries the information on the microscopic ensemble-averaged dynamics of the system. The radiated nonlinear electric field is determined as

$$\begin{aligned} E_S(k_S,t) \quad \propto \quad & iP^{(3)}(k_S,t) = \int dt_3 dt_2 dt_1 S^{(3)}(t_1,t_2,t_3) E_C(k_C, t-t_3) \cdot \\ & \cdot E_B(k_B, t-t_3-t_2) E_A(k_A, t-t_3-t_2-t_1). \end{aligned} \tag{2.1}$$

In the approximation of a predominant dipole interaction between the system and the external optical fields, the response function can be written as a nested commutator of the transition dipole moment $\mu(t)$ valued at the times of the interactions [44]

$$S^{(3)}(t_1,t_2,t_3) = \left(\frac{i}{h}\right)^3 \langle \mu(t_1+t_2+t_3)[\mu(t_2+t_1),[\mu(t_1),[\mu(0),\rho(-\infty)]]]\rangle \,, \tag{2.2}$$

where $\rho(-\infty)$ is the density matrix of the system before the interactions. Here, the dipole moment operator $\mu(t)$ is in the interaction picture and, hence, its time evolution is given by the system Hamiltonian in the absence of applied fields. There are several distinct contributions to the polarization associated with different wavevectors $k_S = \pm k_A \pm k_B \pm k_C$. Each contribution corresponds to a different density matrix pathway, called Liouville pathway, that depends on the sequence of interactions, and leads to the emission of a distinct signal in the corresponding k_S direction. Among the eight possible contributions, only four are independent since k_S and $-k_S$ provide conjugated contributions.

Eq. 2.1 is commonly evaluated in the rotating wave approximation (RWA). Therefore, the terms that are nonresonant with the electric fields drop off, the ones that survive the RWA can be classified as rephasing and non-rephasing contributions. The rephasing signal is emitted with frequency $\nu_S = -\nu_A + \nu_B + \nu_C$ in the direction $k_S = -k_A + k_B + k_C$, whereas the non-rephasing signal with $\nu_S = +\nu_A - \nu_B + \nu_C$ in $k_S = +k_A - k_B + k_C$.

To show the effects of the rephasing and non-rephasing pulse sequences, we consider the field interaction with a system of molecules. As an example, we refer to the pulse sequences corresponding to the pathways S_1 and S_4, shown in Fig. 2.2 by three distinct representations (details on the rules to read them are described in the next paragraph). The first pulse puts the molecules into a coherent superposition between the ground state and the first excited state causing the molecules to oscillate in phase at their initial frequencies. However, the molecules lose their phase relationships quickly because of static inhomogeneous

and dynamical broadening mechanisms, resulting in a decaying macroscopic polarization (free induction decay) during the coherence time τ. The interaction with the second pulse converts the coherence state into a transient population state, which stores the phase information after the free induction decay. During the population period, spectral diffusion, caused, e.g., by dynamic structural evolution of the system, can affect the frequencies of the molecules, causing them to lose memory of their initial frequencies. After the waiting time T, the third pulse brings the system to a second coherent state. If the first and the last pulses interact with wavevector (frequency vector) conjugated with each other, the last pulse can counteract the phase evolution that occurred during the coherence period. Therefore, the molecules initially out of phase undergo a rephasing process. When the rephasing is completed, a macroscopic polarization is formed radiating a photon echo. Conversely, in case of a non-rephasing pulse sequence, the last pulse cannot conjugate the phase evolution occurred during the coherence period τ. As a result of the last interaction, a perturbed free induction decay occurs.

Liouville pathways representations

The Liouville pathways can be equivalently visualized in different representations. The most commonly used one is the so-called double sided Feynmann diagrams [see Fig. 2.2(a)]. Vertical lines represent the time evolution of the ket (drawn on the left) and the bra vector (drawn on the right). Time is running from the bottom to the top. Interactions with the external electric field are represented by arrows. An arrow pointing to the right represents an electric field with $\exp[-i\,(2\pi\nu t - kr)]$, while an arrow pointing to the left represents an electric field with $\exp[-i\,(-2\pi\nu t + kr)]$. The frequency and wavevector of the emitted signal (last dotted arrow) is given by the sum of the input frequencies and wavevectors. This representation allows to visualize in which type of state, coherence ($|\ 0 >< 1\ |$, $|\ 1 >< 0\ |$) or population ($|\ 0 >< 0\ |$, $|\ 1 >< 1\ |$), the system goes after each interaction. Alternatively, if energetic and temporal aspects of the evolution need to be shown, the representation depicted in Fig. 2.2(b) is more appropriate. Time is running from left to right. An arrow pointing upwards represents a change to a higher-energy state and an arrow pointing downward represents a change to a lower-energy state. A solid arrow corresponds to a transition occurring on the ket side of the density matrix, whereas a dotted arrows on the bra side. Solid and dotted arrows in sequence pointing in the same direction bring the system into a population state. The final emitting coherent polarization is depicted by a black arrow. It can be

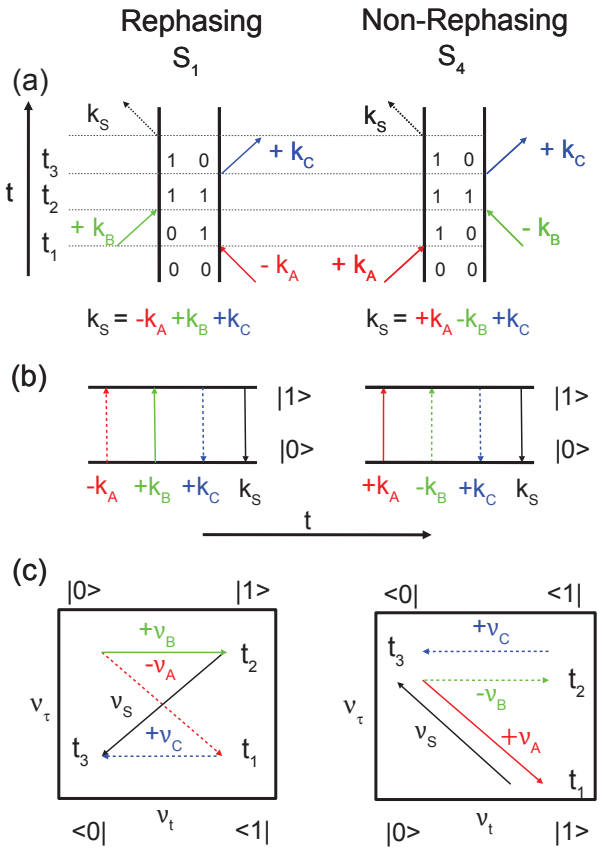

Figure 2.2: Liouville pathways S_1 and S_4 contributing to the rephasing and non-rephasing signals at the third order depicted in various representations: as (a) the commonly used double-sided Feynman diagrams, or as (b) diagrammatic representation of Ref. [101] which displays both energetic and temporal aspects of the evolution , or as (c) frequency vector-chains in the frequency space spanned by the detection frequency ν_t and the excitation frequency ν_τ [78]. In (b) and (c) the solid and the dotted arrows indicate the transition on the ket and on the bra sides of the density matrix, respectively. The frequency vectors determine the orientation of the phase fronts of the driving fields and the nonlinearly emitted field.

emissive as shown by a downward arrow or absorptive indicated by an upward arrow (not shown). An extension to visualize higher-order nonlinear processes is straightforward. This representation will be extensively used in the fourth chapter. Finally, a Liouville pathway can also be represented as a chain of frequency vectors [see Fig. 2.2(c)]. As for the previous representation, a solid arrow refers to a transition along the ket side, conversely a dotted arrow along the bra side. The direction of the frequency vector determines the orientation of the phase fronts of the driving field and the nonlinearly emitted field. This representation allows to discriminate and to isolate different contributions to the nonlinear signal even for a fully collinear interaction geometry.

2.1.2 Methods

A widespread experimental approach for spatially separating the rephasing and non-rephasing contributions uses a beam geometry in which the pulses impinge on the sample from different directions [see Fig. 2.3(a)]. The information on amplitude, phase and frequency of the signal field is obtained by heterodyne detection. The latter produces an interferogram of the local oscillator and the signal whose cross term is proportional to the electric field of the signal

$$I(k_s;\tau,T,t) \propto E_{LO}(k_S;t) \cdot E_S(k_S;\tau,T,t). \tag{2.3}$$

Here, E_{LO} is the electric field of the local oscillator. The interferogram is then spectrally resolved during the detection time t by a monochromator, providing a spectrally resolved measurement ν_t. The Fourier transform along τ on the other hand is performed numerically. As a result, a 2D spectrum $I(k_s;\nu_\tau,T,\nu_t)$ is generated for each waiting time T. The rephasing and non-rephasing spectra however carry both absorptive and dispersive contributions. The latter cause a broadening of spectral features. To obtain a purely absorptive spectrum, one has to properly phase and add together the rephasing and non-rephasing spectra, as shown by Khalil et al. [63]. The measurement of the rephasing and non-rephasing spectra could be performed simultaneously with two detectors placed in the corresponding phase-matched direction. On the other hand, by interchanging the time ordering of the first two pulses the non-rephasing signal will be emitted in the rephasing direction and vice versa. As a consequence, it is enough to place the detector in one phase-matched direction and to switch the order of the first two pulses during the measurement, keeping then constant the delay between the second and the third pulses so as to obtain a fixed waiting time. An alternative way to directly measure the purely absorptive 2D spectrum is by exploiting a pump-probe approach [126]. In this approach, a pair of two

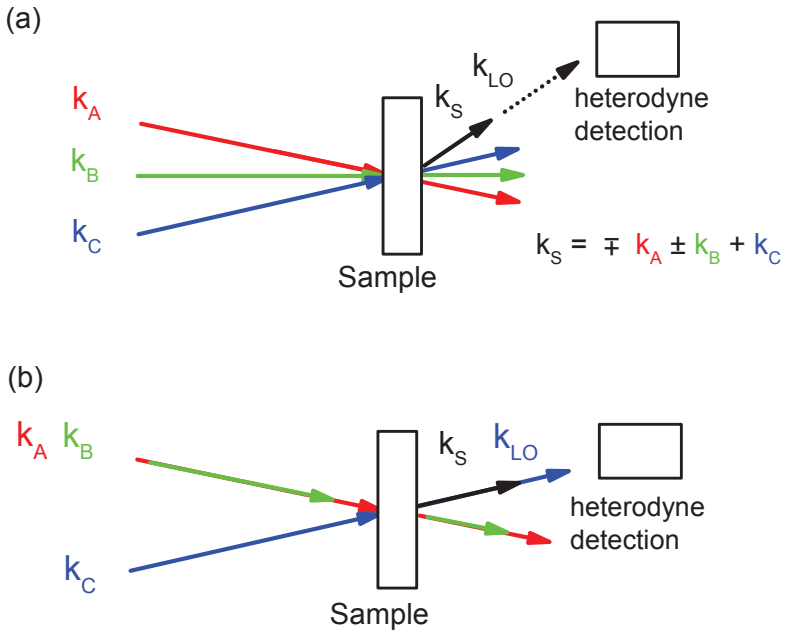

Figure 2.3: (a) Fully non-collinear interaction geometry. The wavevectors k_A, k_B and k_C of the three pulses and the wavevector k_{LO} of the local oscillator are displayed. The different contributions to the third-order nonlinear signal S are spatially separated according to the phase-matching conditions $k_S = \mp k_A \pm k_B + k_C$. The signal is detected by interference with the synchronized local oscillator pulse (heterodyne detection). (b) Partly collinear interaction geometry. Two phase-locked collinear pulses, A and B, serve as pump pulses, whereas pulse C as a probe. The nonlinear signal S is emitted in the direction of the pulse C, which acts as a local oscillator in the detection

phase-locked pulses excites the sample in a collinear geometry and, then, a third pulse, impinging on the sample from a different direction, probes the excitation [Fig. 2.3(b)]. In the pump-probe geometry both the rephasing and non-rephasing contributions are emitted in the same direction as the third pulse, which serves as the local oscillator in the heterodyned detection.

A 2D spectrum is a spectroscopic measurement plotted on two frequency axes, the excitation frequency ν_τ and the detection frequency ν_t. Unfolding the spectral information over two dimensions allows to unravel couplings among excitations. As an example to illustrate what information can be retrieved from a 2D spectrum, we show in Fig. 2.4 a schematic of the correlation spectrum of two coupled vibrational modes. The 0-1 and 1-2 transition frequencies of the modes

1 and 2 are denoted by $\nu_{01}^{(j)}$ and $\nu_{12}^{(j)}(j = 1, 2$, it labels the modes), respectively. The excitation of each mode to its first excited state results in the occurrence of two pairs of spectral peaks of opposite sign, placed at $\nu_\tau = \nu_t = \nu_{01}^{(j)}$. The positive peak, drawn in red, arises from a combination of stimulated emission and bleaching occuring at the 0-1 transition frequency, whereas the negative peak in blue stems from the further excitation of the population in the first excited state to the second, and this is redshifted to $\nu_{12}^{(j)}$. The shift between the peaks is determined by the anharmonicity of the individual vibrational mode. Due to the coupling between the modes, exciting one mode affects also the dynamic of the other one, giving rise to the off-diagonal pairs placed at $(\nu_\tau, \nu_t) = (\nu_{01}^{(1)}, \nu_{01}^{(2)})$ and $(\nu_\tau, \nu_t) = (\nu_{01}^{(2)}, \nu_{01}^{(1)})$. In this case, the separation carries information about the relative distance and the orientation between the modes.

The analysis of the lineshapes of the diagonal peaks provides further insight about the structural environment surrounding the molecules. It is typically carried out for different waiting time. Let us consider an ensemble of identical molecules placed in different surroundings. The interaction with the surrounding changes the vibrational frequency of each molecule by perturbing its vibrational potential. On the time scale in which the environment does not change, the vibrational frequency of each molecule is constant in time and its linewidth cannot be narrower than the natural or homogeneous linewidth. As a result, the 2D spectrum is elongated along the diagonal. In this static case the antidiagonal linewidth represents the homogeneous linewidth whereas the diagonal linewidth is the inhomogeneous linewidth. On the other hand, the molecules can experience spectral diffusion in case of dynamical structural changes of the system. This process causes the frequencies to evolve leading to a broadening of the antidiagonal linewidth. In the limiting case, the initial excited frequencies results completely uncorrelated to the final one causing a symmetrical circular shape of the diagonal peaks.

2.2 Three-pulse 2D THz spectroscopy

The concept of a non-collinear beam geometry is not easy to implement in the THz frequency range. Both the large diameter of the THz beams and the large spot size of the beam focus make it difficult to discriminate the different contributions of the nonlinear signal, and also to separate them from the incident beams. Moreover, the comparably short interaction length limits the thickness of the sample, leading to a modest induced nonlinear signal. On the other hand, in a collinear geometry all the nonlinear contributions are emitted in the same

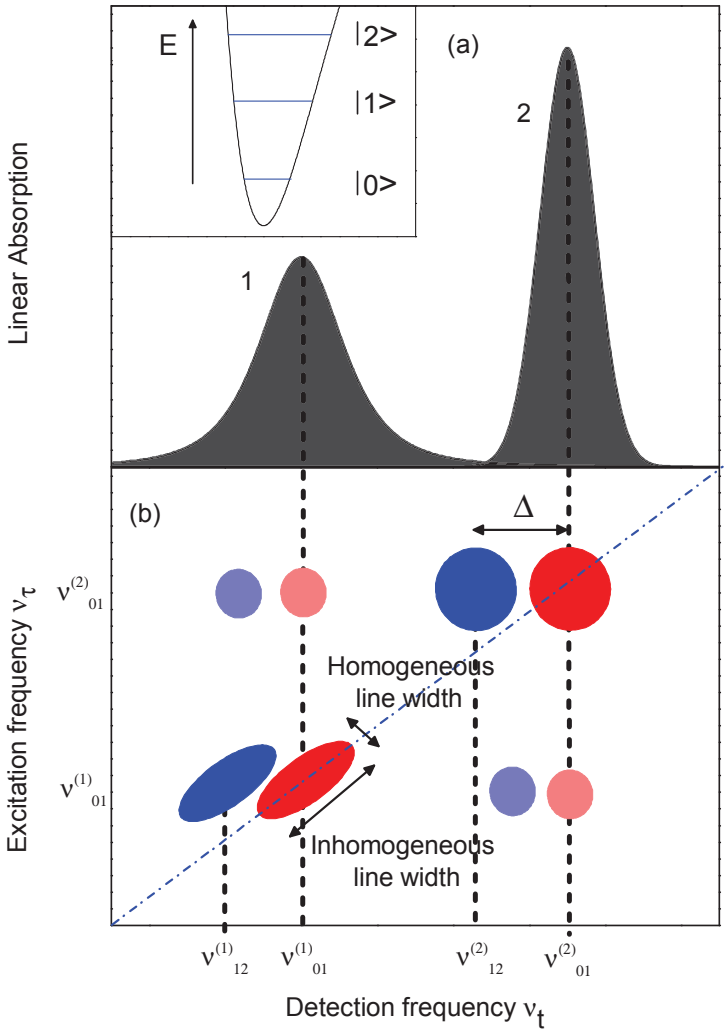

Figure 2.4: Schematic illustration of the informations contained in a 2D spectrum. (a), (b) 1D and 2D spectra of two coupled anharmonic vibrational modes. The inset depicts level scheme of each individual mode. Positive peaks (bleaching and stimulated emission) are shown in red and negative peaks (excited state absorption) in blue. Anharmonicity is shown only for the mode 2 of the diagonal doublet. The hallmark of coupling between the modes are the off-diagonal doublets.

direction of the incoming pulses. One way to separate the nonlinear signal from the transmitted electric field relays on phase cycling [115]. However, the use of this method to signals of nonlinear order higher than 3 is not straightforward. Kuehn et al. [78] have demonstrated a novel scheme of 2D spectroscopy in the THz range which allows both to simultaneously measure nonlinear signals of arbitrary order and to separate them in the frequency domain. It combines the benefits of both collinear beam geometry and phase-resolved detection by electro-optic sampling. The latter allows for measuring both phase and amplitude of the electric fields. An extension of this method to sequences of three pulses will be discussed in the next paragraphs.

2.2.1 Concepts and method

Three phase-locked THz pulses A, B and C with a carrier frequency ν_0 are incident on the sample with collinear wavevectors k_A, k_B and k_C [see Fig. 2.5(a)]. As sketched in Fig. 2.5(b), the THz pulses A and B are separated by the delay time τ, whereas B and C by the delay T. In a typical experiment, for a fixed T the delay time τ is scanned and the transmitted THz electric field is measured in real time t by electro-optic sampling with a fourth pulse, called gating pulse, generating a two-dimensional scan as function of t and τ. To extract the nonlinear signal, the transmitted electric field is measured when all three pulses ABC interact with the sample [as schematically shown in Fig. 2.5(b)], the pairs AB, BC, or CA interact and the single pulses A, B, or C interact. Each of these electric fields contains both the transmitted electric field of the incoming pulses and the nonlinear electric field emitted by the induced nonlinear polarization. Therefore, the electric field stemming from the interaction of all three pulses can be written as the difference

$$\begin{aligned} E_{\mathrm{NL}}(t,T,\tau) &= E_{\mathrm{ABC}}(t,T,\tau) - E_{\mathrm{AB}}(t,T,\tau) - E_{\mathrm{BC}}(t,\tau) \\ &\quad - E_{\mathrm{CA}}(t,T,\tau) + E_{\mathrm{A}}(t,T,\tau) + E_{\mathrm{B}}(t,\tau) + E_{\mathrm{C}}(t). \end{aligned} \quad (2.4)$$

Here, the wavevectors dependence is dropped off because of the collinear geometry. A two-dimensional Fourier transform of the nonlinear signal $E_{NL}(t,T,\tau)$ along t and τ provides the 2D spectra as function of the detection frequency ν_t and the excitation frequency ν_τ. Moreover, the 2D Fourier transform allows to separate the various contributions of the nonlinear signal.

The frequency vector is a key concept to understand how the nonlinear signal is dissected in the frequency domain. Let us consider the electric field of the

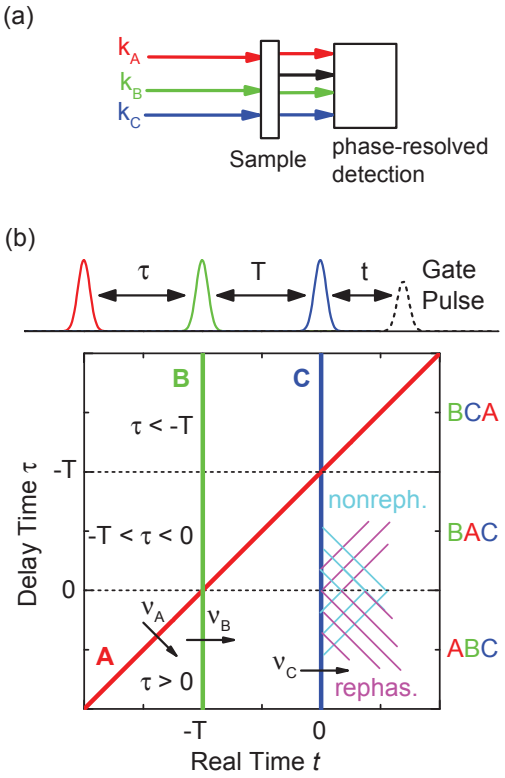

Figure 2.5: (a) Collinear interaction geometry in three-pulse 2D THz spectroscopy with the wavevectors k_A, k_B and k_C. The total electric field transmitted through the sample is fully phase-resolved by electro-optic sampling (EOS). (b) Sequence of three pulses A, B and C as function of the real time t and the delay time τ. For the pulse sequence ABC, occurring for $\tau > 0$, pulses A and B are separated by the coherence time τ, pulses B and C by the waiting time T, and the detection time is triggered by the pulse C. The phase fronts of the rephasing and non-rephasing signals are displayed in magenta and cyan, respectively. The frequency vectors ν_A, ν_B and ν_C are displayed as black arrows and determine the orientation of the phase fronts of their corresponding pulses and of the various contributions to the nonlinear signal.

pulses A, B and C as follows

$$\begin{aligned} E_A(t,T,\tau) &= \varepsilon_{\mathrm{A}}(t-T-\tau)\exp\left[-i2\pi\nu_0(t-T-\tau)\right]+c.c. \\ E_B(t,T) &= \varepsilon_{\mathrm{B}}(t-T)\exp\left[-i2\pi\nu_0(t-T)\right]+c.c \\ E_C(t) &= \varepsilon_{\mathrm{C}}(t)\exp\left[-i2\pi\nu_0 t\right]+c.c, \end{aligned} \tag{2.5}$$

where ε in each expression is a slowly varying envelope. A Fourier transform of Eq. 2.5 along t, T and τ leads to

$$\begin{aligned} \tilde{E}_A(\nu_t,\nu_T,\nu_\tau) &= \delta(\nu_t+\nu_T)\,\delta(\nu_t+\nu_\tau)\,\tilde{\varepsilon}_{\mathrm{A}}(\nu_t-\nu_0) \\ \tilde{E}_B(\nu_t,\nu_T,\nu_\tau) &= \delta(\nu_t+\nu_T)\,\delta(\nu_\tau)\,\tilde{\varepsilon}_{\mathrm{B}}(\nu_t-\nu_0) \\ \tilde{E}_C(\nu_t,\nu_T,\nu_\tau) &= \delta(\nu_T)\,\delta(\nu_\tau)\,\tilde{\varepsilon}_{\mathrm{C}}(\nu_t-\nu_0). \end{aligned} \tag{2.6}$$

Each electric field is uniquely identified in frequency space by a three-component frequency vector $\vec{\nu}=(\nu_t,\nu_T,\nu_\tau)$ defined as

$$\nu_A=\begin{pmatrix}\nu_0\\-\nu_0\\-\nu_0\end{pmatrix},\ \nu_B=\begin{pmatrix}\nu_0\\-\nu_0\\0\end{pmatrix},\ \nu_C=\begin{pmatrix}\nu_0\\0\\0\end{pmatrix}. \tag{2.7}$$

Additionally, the frequency vectors carry a geometrical meaning: their orientation in the Fourier domain determines the orientation of the phase front of any electric field in time domain, e.g., the frequency vectors are orthogonal to the phase front. In the two-dimensional time domain (t and τ) of Fig. 2.5(b), the direction of $\vec{\nu}$ corresponding to each pulse is indicated by a black arrow.

The frequency vector of the nonlinear signal is obtained from linear combinations of ν_A, ν_B and ν_C in strict analogy to the wavevector selection rules of the noncollinear four-wave mixing geometry. In the $\chi^{(3)}$ limit of nonlinear response, the frequency vectors of the rephasing and non-rephasing contributions are $\nu_R=-\nu_A+\nu_B+\nu_C$ and $\nu_{NR}=+\nu_A-\nu_B+\nu_C$. When changing the time ordering of the pulses, the frequency vectors and the coherence, waiting and detection times change their role accordingly. For details see Tab. 2.1.

Typically, the delay T between the pulses B and C is not scanned, i.e., T acts as a fixed experimental parameter and, hence, the component ν_T of the frequency vectors is not accessible. As a consequence, for the pulse sequence BCA one cannot separate the rephasing and non-rephasing contributions. Although the pulse sequence BAC distinguishes the two contributions (shown in

Pulse sequence	Coherence time	Waiting time	Detection time	Rephasing freq. vector	Non-rephasing freq. vector
ABC	τ	T	t	$\begin{pmatrix} \nu_0 \\ 0 \\ \nu_0 \end{pmatrix}$	$\begin{pmatrix} \nu_0 \\ 0 \\ -\nu_0 \end{pmatrix}$
BAC	$-\tau$	$T+\tau$	t	$\begin{pmatrix} \nu_0 \\ 0 \\ -\nu_0 \end{pmatrix}$	$\begin{pmatrix} \nu_0 \\ 0 \\ \nu_0 \end{pmatrix}$
BCA	T	$-T-\tau$	$t+T+\tau$	$\begin{pmatrix} \nu_0 \\ 0 \\ -\nu_0 \end{pmatrix}$	$\begin{pmatrix} \nu_0 \\ -2\nu_0 \\ -\nu_0 \end{pmatrix}$

Table 2.1: Coherence, waiting and detection times and frequency vectors $\vec{\nu} = (\nu_t, \nu_T, \nu_\tau)$ for different pulse sequences.

Fig. 2.5(b) as phase front ($-T < \tau < 0$)), the corresponding two-dimensional THz absorptive spectrum [79] is hard to analyze because the waiting time $T+\tau$ is not fixed, while scanning the coherence time $-\tau$. In contrast, the pulse sequence ABC allows an easy interpretation of the results. However, beyond the $\chi^{(3)}$ limit each pulse can interact with the sample more than once and scenarios different from the one of Tab. 2.1 happen. In this case, all three sequences lead to valuable information on the nonlinear response of the sample.

Selection of the nonlinear signal contributions in the frequency domain

In our collinear two-dimensional spectroscopy, the various optical nonlinearites occur in different positions in frequency space, according to their corresponding frequency vectors. Figure 2.6 schematically shows the spectral peaks of the rephasing and non-rephasing components obtained with the pulse sequence ABC. The corresponding Liouville pathways are visualized as chain of frequency arrows indicating the interaction with the electric field of each pulse. The different components are isolated by filtering and then Fourier transformed back to the time domain. This allows, then, to individually analyzed the single contribution in more details. The filtering has also the effect of effectively reducing the noise because it is performed in two dimensions. As a result, even comparably small nonlinear signal can be extracted [34].

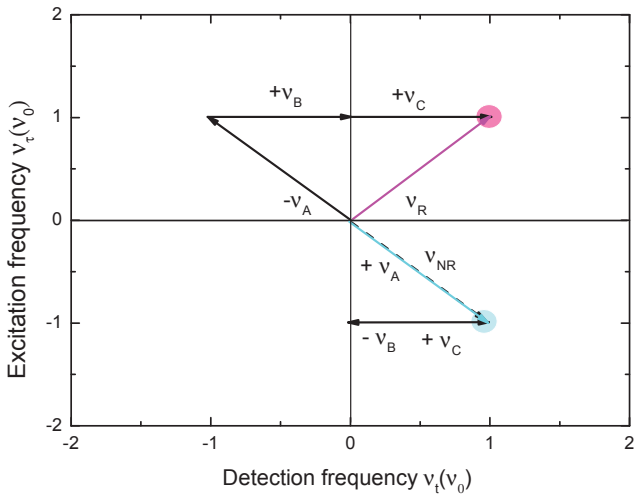

Figure 2.6: Frequency plane spanned by the detection frequency ν_t and the excitation frequency ν_τ. The contributions to the nonlinear signal result separated in the 2D frequency domain. Sequences of the frequency vectors ν_A, ν_B and ν_C corrisponding to the third-order rephasing (magenta) and non-rephasing (cyan) signals. The frequencies are given in units of the carrier frequency ν_0

2.2.2 Experimental setup

The schematic of our experimental setup for 2D collinear THz spectroscopy is illustrated in Fig. 2.7. A Ti:Sa mode-locked oscillator generates linearly polarized 12 fs pulses centered at 800 nm at 85 MHz repetition rate. Two beam splitters (BS) separate a small part of pulses from the oscillator output. Those pulses are used as probe in the EO sampling (EOS). The remaining part of the oscillator pulses feeds two multi-pass amplifiers. Each amplifier delivers 25 fs pulses with a repetition rate of 1 kHz, and energy of up to 1 mJ. A beam splitter divides the output of the first amplifier in two pulses of same energy and mutual delay τ whereas the output pulse from the second amplifier is delayed by a further time interval T. The three beams are sent onto three separated GaSe crystals to drive difference frequency mixing for the generation of three sub-picosecond phase-locked THz pulses A, B, and C. After traveling through the nonlinear crystal, each 800 nm beam is filter out by a silicon wafer. The three THz beams are tightly focused on the sample by a 90° off-axis parabolic mirror. The THz electric fields transmitted through the sample are then imaged by a couple of off-axis parabolic mirrors onto a (110)-oriented ZnTe crystal of 10 μm thickness and detected by EOS. By varying the real time t between the oscillator and the three THz pulses, each THz electric field transient is obtained. Since the three

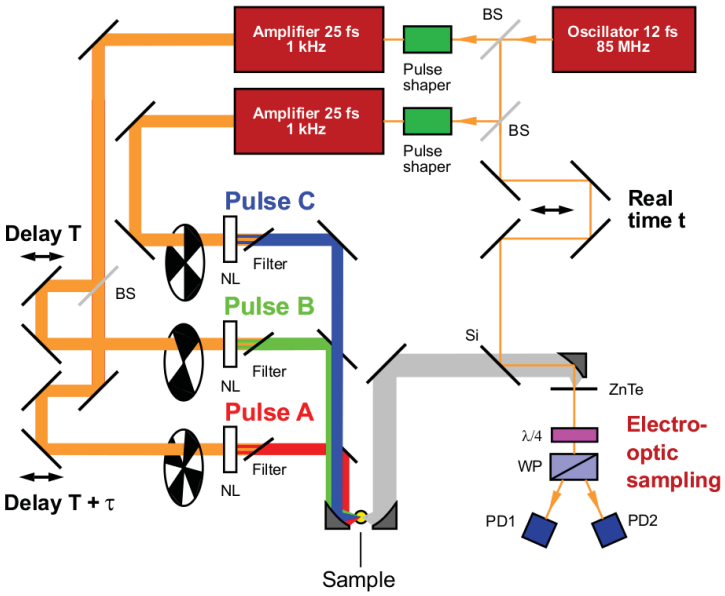

Figure 2.7: Schematic view of the experimental setup for 2D collinear THz spectroscopy. High-field sub-picosecond THz pulses are generated by optical rectification of near-infrared pulses in a nonlinear crystal (NL) and detected by electro-optic sampling (EOS) in a thin ZnTe crystal. Two acousto-optic pulse shapers, implemented in both amplifiers, are used to optimize the THz generation by tailoring the spectral components of the pulses from the oscillator. Three mechanical choppers, placed in the beam paths, allow to separate the nonlinear electric field emitted by the sample from the transmitted THz electric fields.

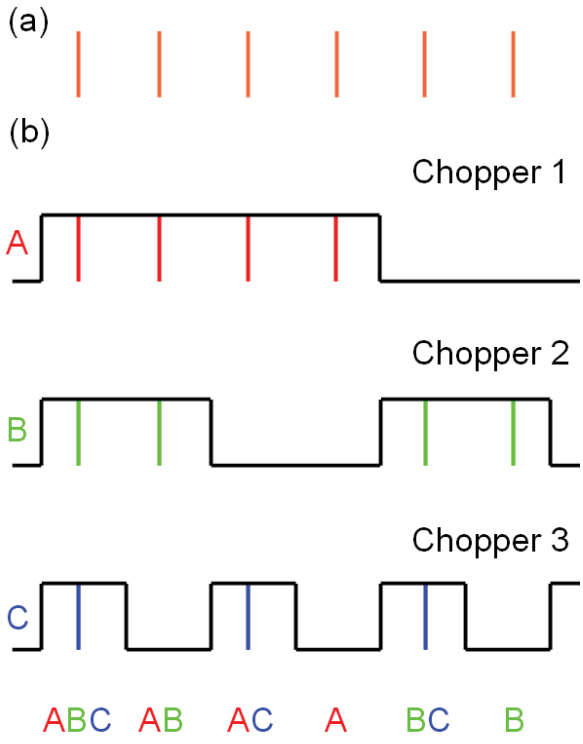

Figure 2.8: (a) Train of laser pulses at 1 kHz repetition rate. (b) Choppers 1,2 and 3 working at 125 Hz, 250 Hz and 500 Hz, respectively. The choppers synchronized with the laser repetition rate allow for sending all pulses ABC, or the pulse pairs AB, AC, or BC, or the single pulses A, B, or C onto the sample.

THz pulses interact in a collinear geometry with the sample, the nonlinear electric field is emitted in the same direction of the THz pulses transmitted through the sample. A method to disentangle the nonlinear electric field from the THz pulses is to place in the beam paths three mechanical choppers synchronized with the amplifier repetition rate (see Fig. 2.8). The chopper 1 blocks every second four pulses, whereas chopper 2 every second two pulses and chopper 3 every second pulse. In this way one can measure seven different combinations of electric fields, one when all three pulses ABC interact with the sample, three for the pairs AB,BC, or CA, and one for the single pulses A, B, or C.

Chapter 3

High-Field THz Bulk Photovoltaic Effect in Lithium Niobate

3.1 Lithium Niobate

Lithium niobate ($LiNbO_3$) is one of the most versatile synthetic ferroelectric materials being widely employed in numerous optical applications. The wide use is made possible by its prominent piezoelectric, photorefractive, electro-optic and nonlinear properties [122]. Its high electro-optic coefficients are exploited for the manufacture of very efficient optical modulators, Q-switches and electro-optic waveguides [2, 20, 57]. Due to its large second-order nonlinear coefficients it is used for optical parametric oscillation, second harmonics generation and difference frequency mixing to generate infrared and THz radiation [81, 90, 95, 128]. In addition, it is applied for holographic data storage technology [19].

At temperatures below its Curie temperature $T_C = 1415$ K [87], i.e., in the ferroelectric phase, the structure of lithium niobate belongs to the R3c space group and consists of planar sheets of oxygen in a distorted hexagonal close-packed configuration; one third of the resulting octahedral interstices are occupied by niobium (Nb), one-third by lithium (Li), one-third is vacant [3, 4]. The cations Nb and Li are displaced from the center of the oxygen octahedra along the trigonal c-axis (see Fig. 3.1). Without external perturbation, the displacement is equally probable in positive or negative c direction, leading typically to multi-domain material (unpoled). Applying a strong electric field

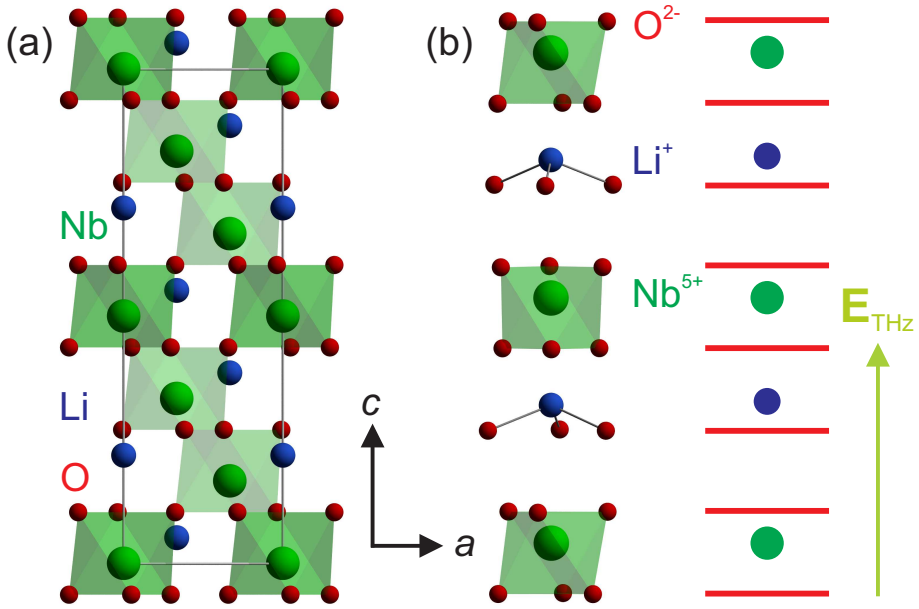

Figure 3.1: Crystal structure of $LiNbO_3$ in the ferroelectric phase ($T < T_C$). (a) Hexagonal unit cell viewed along the b-axis. Lattice constant $c = 1.3863$ nm and $a = 0.5148$ nm. (b) Positions of the lithium ions and the niobium ions with respect to the oxygen octahedra. Octahedral interstices are filled along the c-axis according the sequence: Nb, vacancy, Li, Nb, vacancy, Li, ... The Nb-occupied octahedra share a face with the each of the following vacant octahedra and the preceding Li-occupied octahedra. The green arrow sketches the polarization of the driving THz electric field.

(poling), it is possible to make single-domain crystals. As a consequence of such a displacement, the $LiNbO_3$ crystal lacks spatial inversion symmetry in its ferroelectric state and displays a large spontaneous electric polarization $P_s = 0.71$ C/m^2 [123], corresponding to a voltage drop of $P_s c/\varepsilon_c = 3.5$ V per unit cell along the ferroelectric c-axis.

When studying the photorefractive effect in iron and copper-doped $LiNbO_3$ crystals Glass et al. [40] discovered a new type of photo-induced process, the so-called bulk photovoltaic effect (BPVE). Uniformly exposing the short-circuited crystals to light with wavelengths corresponding to the impurity absorption region (green light), they observed a stationary current flowing parallel to the direction of c-axis and proportional to the incident intensity I [see Fig. 3.2(a)]. Such an unidirectional charge transport through the bulk of the crystal occurred

although there were neither spatial inhomogeneities, i.e., a charge concentration gradient as in a *p*-*n* junction, nor a temperature gradient. The authors explained the occurrence of the (BPVE) current in terms of an asymmetry in the optical transition probabilities of exiting the electrons along the directions parallel and antiparallel to the polar *c*-axis. Such asymmetry was attributed to different transition metal-Fe^{2+} distances along the *c* direction, resulting in an asymmetric potential to which the electrons are bound at the impurity. Accordingly, absorption of a photon excites an electron from a bound state to a conduction band state and the subsequent intraband motion of electrons occurring in the asymmetric potential leads to a net current. However, such two-step model failed to explain the intrinsic (due to fundamental absorption) BPVE [68, 69, 72].

According to the experimental dependence on the intensity and the polarization of the incident radiation, the BPVE is connected with a quadratic tensorial relationship between the current density **J** and the electric field **E**. This relationship is presented in the following form:

$$J_i(t) = \sum_{j,k} \int_{-\infty}^{t} dt' \int_{-\infty}^{t'} dt'' \sigma_{ijk}^{(2)}(t-t';t'-t'')E_j(t')E_k(t''). \tag{3.1}$$

$\sigma^{(2)}$ is the second-order conductivity tensor in the time domain. The stationary bulk photovoltaic (BPV) current is given by the dc component of Eq. (3.1). The BPV current is necessarily null in centrosymmetric system, i.e., the BPVE can occur only in crystals lacking a center of inversion. Bulk polarization (ferroelectricity) is not necessary. In the frequency domain the BPV current reads

$$J_i(\Omega) = \sigma_{ijk}^{(2)}(\Omega = \nu_1 - \nu_2; \nu_1, \nu_2)E_j(\nu_1)E_k^*(\nu_2). \tag{3.2}$$

Baltz and Kraut [73, 121] proposed a microscopic theory of the BPVE which was founded on a quantum-mechanical representation of the BPV current in terms of Bloch states. In a perturbative density-matrix calculation, they demonstrated that:

- the BPVE exclusively stems from the non-diagonal components of the density current operator, i.e., it is connected to the interband transition (see Eq. (37) of [121]),
- the damping of the quantum coherences in generating the BPV current plays a role (see Eq. 21 of [73]).

Although Eq. (3.1) is mathematically analogous to the quadratic relationship between the induced polarization **P** and the electric field **E**, the BPVE is substantially different from optical rectification: the latter involves a nonresonant $\chi^{(2)}$

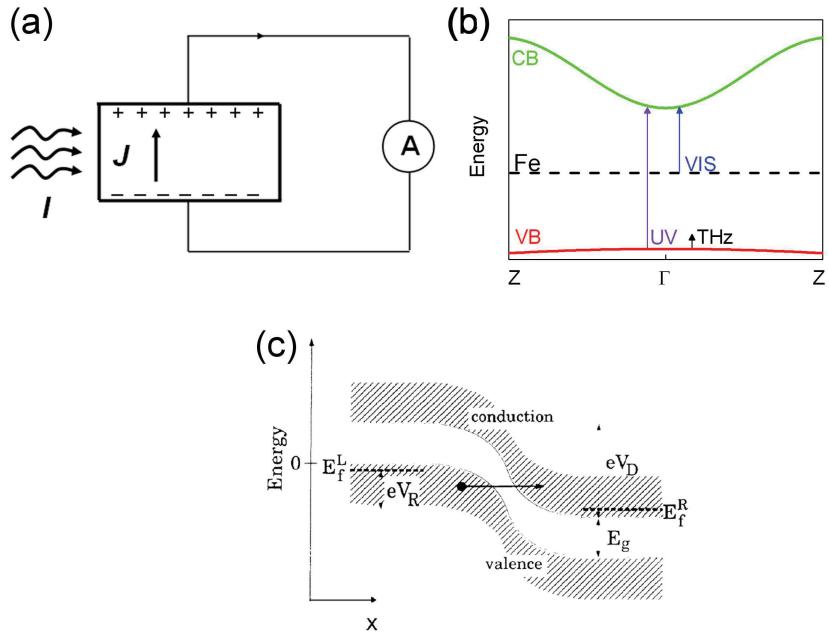

Figure 3.2: (a) Conventional bulk photovoltaic effect. Upon uniform illumination with radiation in the absorption range, ferroelectric materials as $LiNbO_3$ [40], $BaTiO_3$ [69] develop a short-circuit photovoltaic current density J. (b) Schematic of the $LiNbO_3$ band structure. Comparison among the band gap energy and the most frequently used photoexcitations for generating a shift current. Ultraviolet radiation (violet arrow) and visible radiation (blue arrows) for iron-doped lithium niobate. The THz photon energy (8 meV at 2 THz) is far below the bandgap ($E_g = 4$ eV corresponding to approximately 1000 THz). (c) Zener tunneling [27] in a p-n junction. A strong electric field can bend the valence and the conduction bands in such a way that an electron in the valence band can tunnel to the conduction band.

optical nonlinearity, visualized, e.g., by nonresonantly induced bound-charge dipoles oscillating in an asymmetric potential; the former is associated with the generation of charge carriers in the resonantly excited bands and gives rise to an electric current.

More recent theoretical and experimental works have suggested the so- called shift current as basic mechanism for the BPVE [23, 96, 110, 129]. The current density J of Eq. (3.2) originates from the difference of the center of the electronic charge in the unit cell for the valence and the conduction bands. Therefore, a resonant interband excitation of electrons from valence to conduction bands is accompanied by an asymmetric shift of the center of charge in real space between

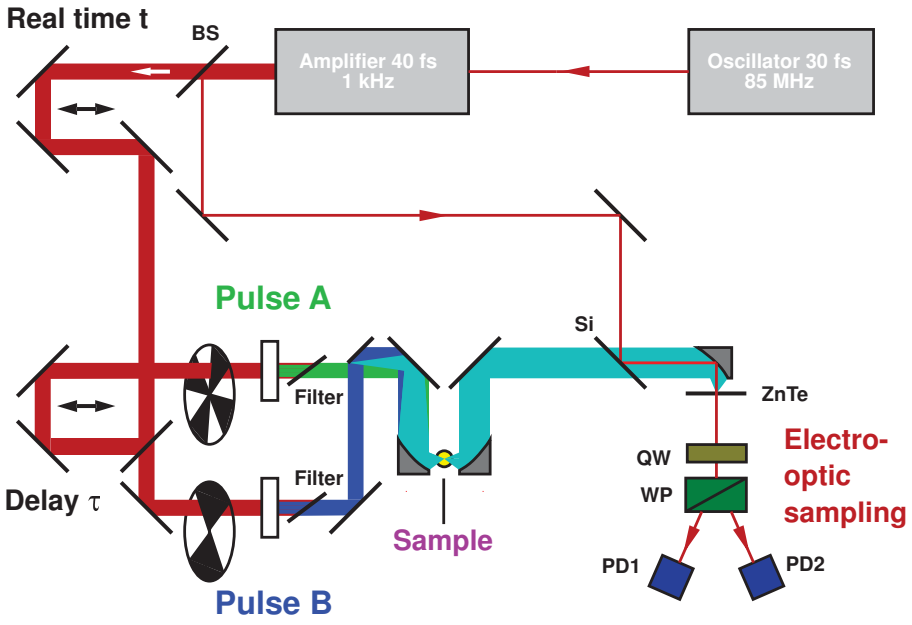

Figure 3.3: Schematic view of the experimental setup for 2D THz spectroscopy. Intense THz electric fields are generated via DFG of NIR pulses in GaSe crystals and detected by EO sampling in a ZnTe crystal.

the atoms in each unit cell. The shift is of the order of the bond length and occurs on femtosecond time scales [96].

In contrast to all previous work, we address the BPVE from a completely different perspective. To study the shift current on its ultrafast time scales without involving direct photo-absorption, we exploit a strong pulsed excitation in the THz range well below any electronic absorption. Furthermore, the BPVE is investigated in the nonperturbative regime of light-matter interaction. In this regime, the carrier generation relies on THz-induced nonresonant Zener tunneling of electrons from the valence into the conduction band [77].

3.2 Experiment and Results

We investigate the nonlinear response of an undoped single-domain $LiNbO_3$ crystal of thickness $d = 50$ μm by collinear two-dimensional (2D) THz spectroscopy. The sample is cut in such a way that the polar c-axis lies in the surface plane. Our experimental set-up is sketched in Fig. 3.3. Two intense phase-locked THz pulses A and B with electric field amplitudes of approximately 100 kV/cm are generated by DFG of 800 nm pulses from a Ti:Sa amplifier in two GaSe

crystals. Both pulses are polarized along the direction parallel to the ferroelectric c-axis. Their frequencies are centered at 2 THz very far below the bandgap of the sample ($E_g \approx 1000$ THz). The electric field waveforms of the two pulses transmitted through the $LiNbO_3$ are detected in a ZnTe crystal by electro-optic sampling as a function of the real time t and the delay time τ between the two THz pulses. To separate the nonlinear signal from the transmitted electric fields, we use in the beam paths only two choppers synchronized with the laser repetition rate of 1 kHz. In this way, for each time point (t,τ) we measure the electric field transmitted through the sample for four situations, one when all two pulses AB interact with the sample, two for the single pulses A or B, and one when neither pulse A nor pulse B interact with the sample. While the temporal position of pulse B is kept constant, the mutual delay between pulse A and pulse B is varied from $\tau = -2$ ps to $\tau = 2$ ps [see Fig. 3.4(a)]. The measurements are performed at room temperature and under nitrogen atmosphere to remove the influence of water vapor.

The nonlinear field emitted from the sample is retrieved as the difference

$$E_{NL}(t,\tau) = E_{AB}(t,\tau) - E_A(t,\tau) - E_B(t). \tag{3.3}$$

Since the thickness d of our sample is much smaller than the wavelength of the THz pulses, the nonlinear signal $E_{NL}(t,\tau)$ is proportional to the nonlinear current density $j_{NL}(t,\tau)$ induced in the sample by the incident THz field, and reads

$$E_{NL}(t,\tau) = -\frac{Z_0 d}{2} j_{NL}(t,\tau), \tag{3.4}$$

where $Z_0 = 377\ \Omega$ is the vacuum impedance. Accordingly, the nonlinear electric field E_{NL} provides the full information of the microscopic carrier dynamics along the c-axis. As shown in Fig. 3.4 (b), the nonlinear signal occurs mainly when the two pulses overlap in time with t and τ spanning respectively between approximately ± 0.7 ps and ± 1 ps. Furthermore, it has opposite phase with respect to the driving field E_{AB}. Figure 3.4(c) shows the strongest electric nonlinear transient which occurs for delay time $\tau = 0$. For a better comparison with the driving field E_{AB}, the amplitude of the nonlinearly emitted electric field is magnified 10 times. It reaches its maximum value of 20 kV/cm at $t = 0$ and is almost unidirectional. According to Eq. 3.4, the underlying current is unidirectional, too.

To decompose the nonlinear signal into different terms we perform a 2D Fourier transform (2DFT) of $E_{NL}(t,\tau)$ along both time axes t and τ. Moreover, to identify the type of nonlinearity we use the frequency vector analysis discussed in the previous chapter. The frequency vectors associated with pulse A and pulse

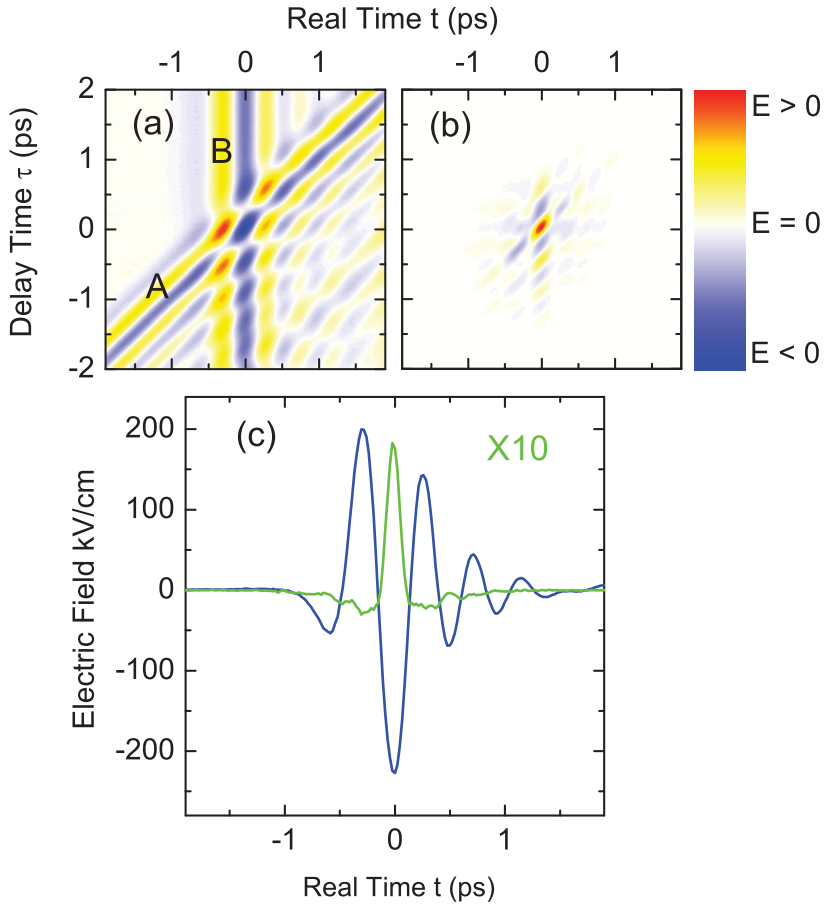

Figure 3.4: Experimental results. (a) Electric field $E_{AB}(t,\tau)$ transmitted through the sample plotted as a function of the real time t and the delay time τ. The amplitude of the driving field $E_{AB}(t,\tau)$ ranges from -220 kV/cm up to 200 kV/cm. (b) Nonlinear THz signal $E_{NL}(t,\tau) = E_{AB}(t,\tau) - E_A(t,\tau) - E_B(t)$ emitted by the sample. The field amplitude ranges from about -3 kV/cm up to approximately 20 kV/cm. The colour bar shows the sign of the electric fields. (c) Electric field E_{AB} (blue line) and nonlinear electric field E_{NL} (green line) for $\tau = 0$ as function of the real time t. The electric field E_{NL} has opposite direction of the total electric field E_{AB} and an amplitude of about 20 kV/cm.

B in the 2D frequency domain are $\nu^A = (2\text{ THz}, -2\text{ THz})$ and $\nu^B = (2\text{ THz}, 0)$. As we use fully-phase resolved detection, the 2DFT calculates the real and imaginary parts of the nonlinear signal without ambiguity. The 2DFT signal $E_{NL}(\nu_t, \nu_\tau)$ is presented in Figs. 3.5(a) and 3.5(b) as a function of the detection frequency ν_t and excitation frequency ν_τ. Figures 3.5(a) and 3.5(b) shows the

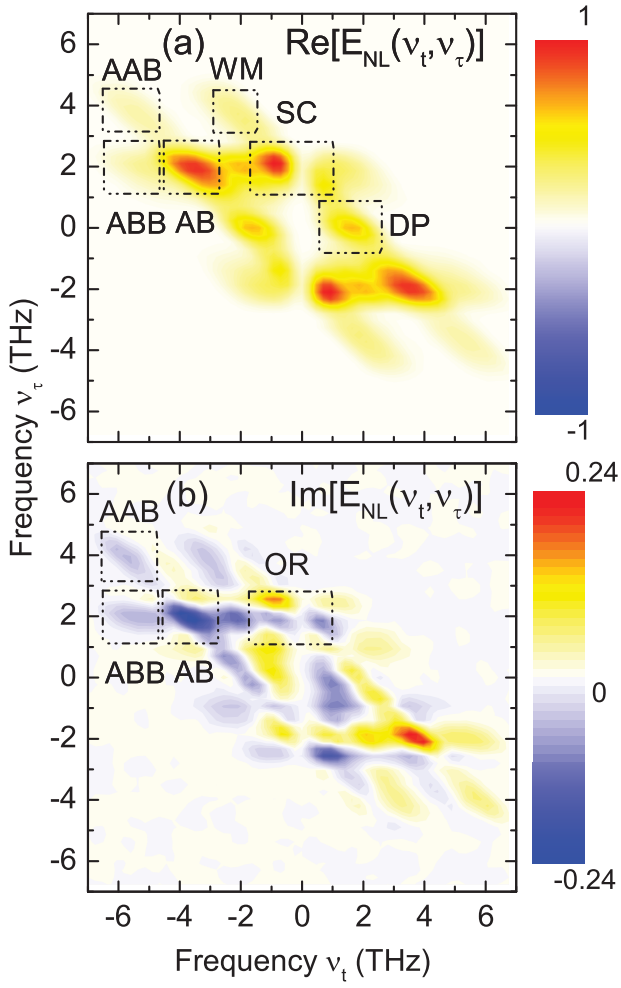

Figure 3.5: 2D Fourier transform of the nonlinear signal $E_{NL}(t, \tau)$ along the real time t and the delay time τ. (a), (b) Real and imaginary parts of the spectrum display the signatures of the shift current (SC), the optical rectification (OR), the second (AB) and the third (ABB) and (AAB) harmonics, wave mixing (WM), and the pump depletion signal (DP). The real part has a maximum amplitude four times larger than the imaginary part.

real and the imaginary part of the signal, respectively the 2D spectra show a spot at frequency vector $\nu^{AB} = (-4\ \text{THz}, 2\ \text{THz})$. It is caused by the frequency combination $-(\nu^A + \nu^B)$ and corresponds to second harmonic generation. We observe also spectral peaks at $\nu^{AAB} = -(2\nu^A + \nu^B) = (-6\ \text{THz}, 4\ \text{THz})$ and $\nu^{ABB} = -(2\nu^B + \nu^A) = (-6\ \text{THz}, 2\ \text{THz})$. They are connected to third harmonic generation where one of the pulses interacts twice with the system. In

addition a wave mixing signal and a pump depletion signal are found at $\nu^{WM} = -(2\nu^A - \nu^B) = (-2\ \text{THz}, 4\ \text{THz})$ and $\nu^{DP} = \nu^A - \nu^A + \nu^B = (2\ \text{THz}, 0)$, the latter caused by the conversion of the fundamental into higher harmonics. There are also contributions at frequencies close to $\nu \approx \nu^B - \nu^A = (0, 2\ \text{THz})$, labeled as shift current (SC) and as optical rectification (OR). However, the direct current (DC) component of the nonlinear signal cannot be accessed with electro-optic sampling since it is not radiated, therefore at the detection frequency $\nu_t = 0$ both signals SC and OR vanish. Since $E_{NL}(t, \tau)$ is real, the real part of the 2DFT signal $E_{NL}(\nu_t, \nu_\tau)$ is symmetric with respect to the transformation $(\nu_t, \nu_\tau) \rightarrow (\nu_t^{'}, \nu_\tau^{'}) = -(\nu_t, \nu_\tau)$, the imaginary part is anti-symmetric. As a result the remaining spots at frequencies $(\nu_t^{'}, \nu_\tau^{'}) = -(\nu_t, \nu_\tau)$ give no further information.

3.3 Discussion

There are two possible sources accounting for the signatures of the 2D spectra: (i) currents generated by oscillating nonlinear polarizations, i.e., $J_P^{(2,3)}(t) = dP^{(2,3)}(t)/dt$, and (ii) currents of electrons generated and driven by the THz electric field. The mechanism (i) is not connected to a transport of free electrons but to oscillating nonresonantly field-induced dipoles of bound electrons. As the THz excitation is far from any resonances of $LiNbO_3$, one expects real nonlinear polarizations $P^{(2,3)}(t)$, the underlying susceptibilities being real. As a consequence, the mechanism (i) generates currents, which are 90° out of phase with respect to the driving field and, thus, such currents emit nonlinear electric fields which have only an imaginary part in the frequency domain. Therefore, real nonlinear polarizations, i.e., nonresonant $\chi^{(n)}$ mixing processes, explain only the contributions of the imaginary part of $E_{NL}(\nu_t, \nu_\tau)$ [Fig. 3.5(b)]. Our experiment, however, demonstrates that the nonlinear emitted field $E_{NL}(t, \tau)$ shows a real part even larger than the imaginary one. Thus, the nonlinear behavior of the $LiNbO_3$ crystal under strong THz excitation is dominated by the mechanism underlying $\text{Re}[E_{NL}(\nu_t, \nu_\tau)]$. The latter corresponds to currents in phase with respect to the driving field and, therefore, involves the generation of free electrons in the crystal [mechanism (ii)].

The mechanism (ii) is consistent with the experimental finding that the energy density transiently deposited by the driving THz field is irreversibly

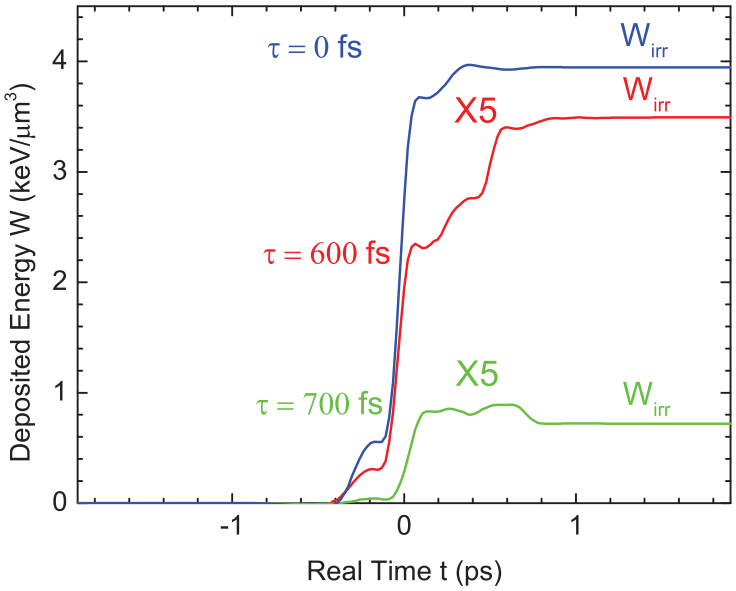

Figure 3.6: Electromagnetic energy density transiently deposited in the sample by the total field E_{AB} for different delay times τ. For $\tau = 0$ and 600 fs, all the deposited energy density is irreversible stored in the sample, whereas for $\tau = 700$ fs part of it is coherently reemitted.

stored in the sample. We calculate it as follows [38, 77]:

$$W(t,\tau) = \int_{-\infty}^{t'} j_{NL}(t',\tau) E_{AB}(t',\tau) dt' = \frac{-2}{Z_0 d} \int_{-\infty}^{t'} E_{NL}(t',\tau) E_{AB}(t',\tau) dt'. \tag{3.5}$$

Figure 3.6 displays $W(t)$ for different delays τ. For $\tau = 0$ during the driving THz pulse the amount of deposited electromagnetic energy density increases as a function of time up to $W_{\max} = 4$ keV/μm^3. Due to decoherence processes, this energy density is not coherently reemitted and contributes to the generation of free charge carriers. An energy density deposition of 4 keV/μm^3 leads to an e-h generation of density $n_{e-h} = 4000$ e-h/μm^3. We found an analogous behavior for $\tau = 600$ fs, but $W_{\max} = 700$ eV/μm^3. Finally, for delay $\tau = 700$ fs the maximum and irreversibly deposited energy density do not coincide, being $W_{\max} = 178$ eV/μm^3 and $W_{\text{irr}} = 144$ eV/μm^3, the difference is coherently reemitted. As a remark, the peak amplitude of the driving electric field E_{AB} decreases as the delay τ between the pulses A and B increases and, thus, results in a nonlinear current density with an amplitude decreasing as τ increases. Such analysis allows to conclude that the mechanism of charge-carrier generation depends on both the amplitude of the THz driving field and on decoherence

processes.

The electronic bandgap of $LiNbO_3$ is about 1000 times larger than the THz photon energy. How can the THz radiation induce the shift current and its higher nonlinear terms? Kuehn et al. [77] have recently demonstrated that free electrons can be generated by high-field THz induced interband tunneling of electrons from the valence into the conduction band.

The basics of this mechanism are as follows. The electric field of the THz driving pulse creates a coherent superposition of valence band states and conduction band states, corresponding to a creation of "virtual" electron-hole pairs, responsible for the deposited energy density W_{max}. Here, virtual means that this energy density can be coherently reemitted, thus, not leading to any generation of real electron-hole pairs when the incident field is switched off. Furthermore, the coherent superposition undergoes an intraband motion under the influence of the THz electric field. During this motion, the conduction band and the valence band parts move in opposite direction and follow an oscillatory motion in real space. A strong THz electric field leads to a spatial separation of the electron and the hole parts inside the wave packet, that can extend in space over several 100 nm. As a consequence of such large separation, both parts interact with different environments, caused by, e.g., random thermal fluctuations. Therefore, the two parts gradually and irreversibly lose their phase relationship. Such behavior is summarized in the following expression [131, 132] for the interband decoherence rate

$$\Gamma_{ij}(t) = \tau_m^{-1} \left(\frac{\Delta x_{ij}(t)}{\lambda_{dB}} \right)^2 , \tag{3.6}$$

where τ_m is the momentum relaxation time, Δx_{ij} the electron-hole separation within the wave packet and $\lambda_{dB} = \hbar(2mk_BT)^{-1/2}$ the thermal de Broglie wavelength. At room temperature with a spatial separation of 200 nm the ratio of the decoherence and the intraband damping rate is $\Gamma/\tau_m^{-1} \sim 10^3$. Even for a momentum relaxation time of 1 ps, the quantum coherence would be irreversibly destroyed in 1 fs. A sufficiently high decoherence rate leads to the generation of free incoherent electron-hole pairs by dephasing of the interband polarization wave packet. In $LiNbO_3$ the generation of free charge is connected to an unidirectional motion, i.e., a current, due to the asymmetric potential along the ferroelectric c-axis of the crystal [see Fig. 3.7(a)].

3.4 Model Calculation

Similar to the theory of Kraut and Baltz [73], our theoretical treatment is based on the Liouville equation of the density operator,

$$i\hbar\dot{\rho}(t) = [H(t), \rho(t)] - i\hbar\Gamma(t, \rho(t)). \tag{3.7}$$

The first term accounts for the light-matter interaction and the propagation of the density matrix, whereas the term Γ is a relaxation operator. Its diagonal elements describe the population relaxation, whereas its non-diagonal the decoherence relaxation of the interband polarization. Equation 3.6 gives the interband decoherence rate as function of the time-dependent electron hole separation within the interband polarization wave packet ρ_{ij} between bands i and j. The separation is calculated as

$$\Delta x = \int v_e(k(t))dt. \tag{3.8}$$

Here v_e is the electron velocity and is obtained from the band structure (the velocity of the holes is negligible) and k is the wave vector of the coherent superposition

$$k(t) = -eA(t)/\hbar, \tag{3.9}$$

where $A(t)$ is the vector potential of the THz driving field and e is the electron charge. In our calculations we neglect the diagonal terms, caused , e.g., by spontaneous electron-hole recombination, because nanosecond lifetimes of electrons in the conduction band yields a low decay rate.

We describe the light-matter interaction in the nonperturbative regime and use the $\mathbf{p} \cdot \mathbf{A}$ gauge. We search for solutions of the Liouville equation of the form

$$\Psi_{b,\mathbf{k}}(\mathbf{r}, t) = e^{i\mathbf{k}\cdot\mathbf{r}} \sum_{\mathbf{G}} c_{b,\mathbf{k},\mathbf{G}}(t) e^{i\mathbf{G}\cdot\mathbf{r}}, \tag{3.10}$$

which describes a Bloch electron with wave vector $\mathbf{k}$ in the band b as a coherent superposition of plane waves displaced by the reciprocal lattice vectors $\mathbf{G}$. The function $u_{b,\mathbf{k}}(\mathbf{r}, t) = \sum_{\mathbf{G}} c_{b,\mathbf{k},\mathbf{G}}(t) e^{i\mathbf{G}\cdot\mathbf{r}}$ has the period of the crystal lattice with $u_{b,\mathbf{k}}(\mathbf{r}, t) = u_{b,\mathbf{k}}(\mathbf{r} + \mathbf{R}, t)$. Here, $\mathbf{R}$ is a translation vector of the lattice. The coefficients $c_{b,\mathbf{k},\mathbf{G}}$ are calculated by diagonalizing the following single-particle Hamiltonian which incorporates the interaction with the electromagnetic field in the vector potential $\mathbf{A}$(t) [77]:

$$[H(\mathbf{k}, \mathbf{A})]_{\mathbf{G},\mathbf{G}'} = \frac{\delta_{\mathbf{G},\mathbf{G}'}}{2m_0} [\hbar (\mathbf{k} + \mathbf{G}) - e\mathbf{A}]^2 + V(\mathbf{G} - \mathbf{G}') \tag{3.11}$$

Here, the V(**G**) are the coefficients of the Fourier expansion of the periodic potential and m_0 is the free electron mass. Our single-particle treatment neglects all many-body interactions, among them electron-electron (e-e), electron-phonon (e-ph) and electron-impurity (e-imp) scatterings. The e-e scattering leads to a redistribution of the electrons in the bands, which does not affect the current amplitude because the total momentum of the electrons is conserved. Incoherent e-ph and e-imp scatterings yield a randomization of the electron momentum, which creates an asymmetric distribution of electrons in the conduction band within a momentum relaxation time given by the inverse of the scattering rate $1/\tau = 1/\tau_{e-ph} + 1/\tau_{e-ph}$, resulting in an ohmic transport for driving electric field with small amplitude and oscillations on a time scale larger than the scattering time. The e-ph scattering dominates over the e-imp one at room temperature. As observed in [76], the dynamic of an electron in a high-amplitude THz electric field can be decoupled from the phonons even for all the duration of the driving pulse, resulting in a ballistic motion for times longer than the momentum relaxation time.

The electronic band gap of our system is much larger than k_BT, therefore we assume that initially all the valence band states are filled and all the conduction band states are empty. The relaxation operator has an useful representation only in the $\mathbf{r} \cdot \mathbf{E}$ gauge, therefore in solving Eq. 3.7 it is necessary to transform back and forth between the two gauges in every step of the calculation. Once ρ(t) is obtained , the current density is calculated as $J(t) = e\mathrm{Tr}[\rho(t)v]$.

Results of the model

Since we have not performed a band structure calculation for $LiNbO_3$, we have applied the interband tunneling mechanism to a one-dimensional model crystal which has no inversion symmetry. Nevertheless, our model allows to qualitatively explain the experimental results. Figure 3.7(a) displays the asymmetric potential and the electronic probability density relative to valence and conduction bands, which are shown in Fig. 3.7(b). We consider two equal THz pulse of amplitude E/2 and with center frequency ν_0. They are overlapped in time. In analogy how we determine the nonlinear emitted field in our experiment (cf. Eq. 3.3), we calculate the spectrum of the THz-induced nonlinear interband current density as $\Delta J_E(\nu) = J_E(\nu) - 2J_{E/2}(\nu)$. The first term corresponds to the case when both fields are present and the last one to when each field is singly present. In our calculations we vary the driving field amplitude E from 1 to 3000, the latter corresponds to the experimental value of 200 kV/cm. Figure 3.7(c) displays the overall spectra, real and imaginary part of $\Delta J_E(\nu)$,

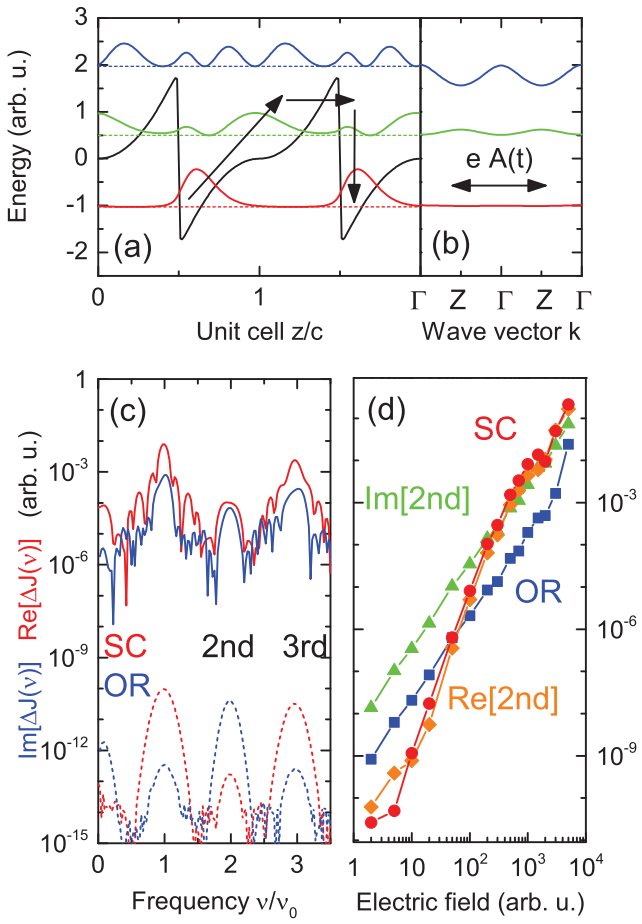

Figure 3.7: 1D Model crystal. (a) Asymmetric potential (black line), the black arrows show the unidirectional motion of the electron upon THz field-induced interband tunneling. The red, green, and blue curves show the electronic probability density in the valence and in the two conduction bands, respectively. (b) Band structure of the 1D model crystal. (c) Spectra of the Re[ΔJ(ν)] and Im[ΔJ(ν)] interband currents driven by the THz electric field for two amplitudes $E = 1$ (dashed lines) and $E = 3000$ (solid lines). (d) Amplitudes of the shift current (SC) (circles), real second harmonic Re[2nd] (diamonds), optical rectification (OR) (squares) and imaginary second harmonic Im[2nd] (triangles) as function of the THz electric field strength.

corresponding to a driving THz electric field of 1 (dashed lines) and 3000 (solid lines) in amplitude, whereas Fig. 3.7(d) shows the different contributions to the nonlinear interband current as function of the driving THz field amplitude.

In the limit of small field amplitude (E=1), the nonlinear behavior is dominated by $\mathrm{Im}[\Delta J_E(\nu)]$ and is within the $\chi^{(2)}$ limit of nonlinear response. Low-frequency (OR) and second harmonic (2nd) components depend quadratically on the driving field. Conversely, for high field strength ($E = 3000$) the system is driven into the nonperturbative regime of light-matter interaction and the nonlinear response is controlled by $\mathrm{Re}[\Delta J_E(\nu)]$.

The strength of the shift current crucially depends on the interband decoherence (Eq. 3.6). For low field strength, the vector potential $A(t)$ of the driving THz field allows the wave packet of the electron-hole pair to explore a small portion of the Brillouin zone. This leads to a small spatial separation Δx and, thus, the interband decoherence contributes to the generation of a negligible amount of electron-hole pairs. Therefore, in this limit the shift current is smaller than the optical rectification contribution. For field strength ($E > 500$) at which the system enters the nonperturbative regime there is a drastic change of amplitude of the shift current. In this regime, the wave packet is driven through a large portion of the Brillouin zone, eventually up to its boundary [Z point in Fig. 3.7(b)], resulting in a large spatial separation Δx and, thus, in a large interband decoherence rate according to Eq. 3.6. As a consequence, a significant amount of charge carriers are generated, that increase the amplitude of the shift current to values even higher then the optical rectification contribution. Finally, when we do not include interband decoherence in our calculation the shift current vanishes completely, since the interband tunneling is reversible without decoherence and, thus, does not lead to an irreversible generation of free charge carriers.

Summary

In this Chapter, we have presented the first studies of the high-field bulk photovoltaic effect in $LiNbO_3$ under nonperturbative conditions. Exploiting two-dimensional collinear THz spectroscopy with two high-field phase-locked THz pulses polarized along the ferroelectric c-axis of a $LiNbO_3$ crystal, we have separated the nonlinear response into distinct contributions in the two-dimensional Fourier domain, i.e., a rectification signal close to zero frequency, second- and third-harmonic signals. We have identified the nonlinear interband shift current as the source of the nonlinear signals. The shift current has been generated by

interband tunnelling.

Chapter 4

Ultrafast Dynamics of Nonlinear Two-Phonon and Two-Photon Interband Coherences in Indium Antimonide

4.1 Indium Antimonide

Indium antimonide (InSb) is a III-V semiconductor with the zinc-blende crystal structure. Figure 4.1 shows the electronic band structure of InSb which has been calculated with a method known as the emprirical pseudopotential technique [26]. InSb is characterized by a direct bandgap of $E_g = 0.17$ eV (41 THz), which is localized around the high-symmetry point Γ in k-space. The valence band exhibits three distinct bands. The heavy-hole (HH) and the light-hole (LH) bands are characterized by different dispersions and are degenerate at $k = 0$. Moreover, a split-off hole (SO) band is present which by virtue of the spin-orbit coupling is shifted down in energy by the spin-orbit splitting Δ_0. Experimental values of the main features of the band structure are summarized in Tab. 4.1.

Below the electronic interband transitions, the semiconductor InSb exhibits various vibrational modes. Figure 4.2 shows the phonon dispersion curves of InSb measured by inelastic neutron scattering along the high-symmetry direc-

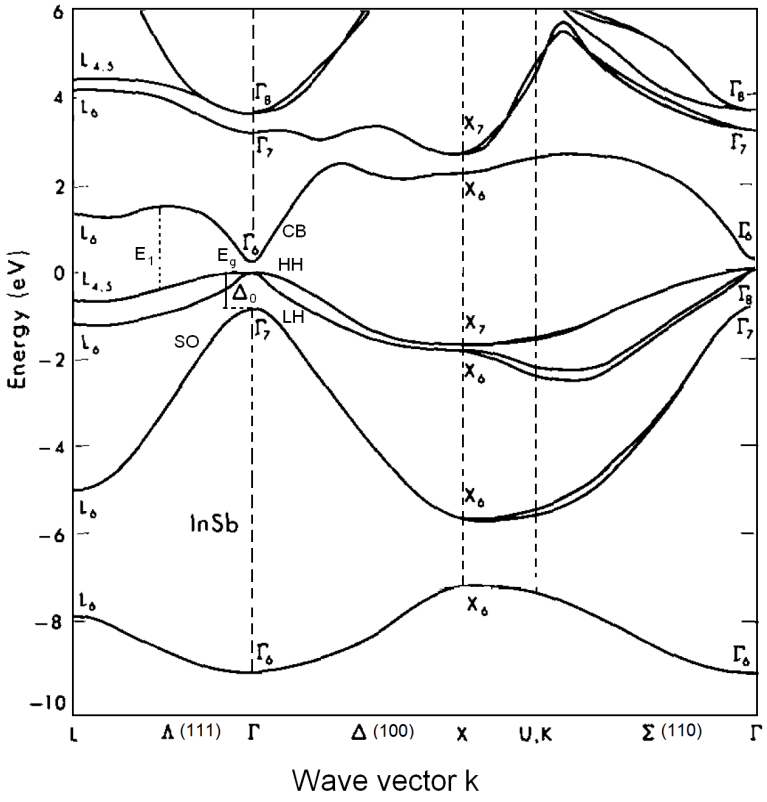

Figure 4.1: Electronic band structure of InSb calculated by the pseudopotential technique along the principal symmetry directions in the Brillouin zone [26]. $\Gamma_6, \Gamma_7, \Gamma_8$, and etc. indicate the symmetry of the basis functions. At valence-band edge, the valence band (VB) consists of heavy-hole (HH) and light-hole (LH) bands, and a split-off hole (SO) band which is separated by the spin-orbit splitting Δ_0. The conduction band (CB) is separated from the top of the valence band by the energy gap E_g. Values of the main features are summarized in Tab. 4.1.

InSb						
E_g [eV]	E_1 [eV]	Δ_0 [eV]	m_c/m_0	m_{HH}/m_0	m_{LH}/m_0	m_{SO}/m_0
0.17	1.9	0.81	0.015	0.42	0.016	0.19

Table 4.1: Experimental values: direct band gap E_g, E_1 transition, valence band spin-orbit splitting at zone center Δ_0 given in units of eV, conduction band effective mass m_c, heavy-hole m_{HH}, light-hole m_{HH}, and spin-orbit split-off hole m_{SO} effective masses given in units of the free electron mass.

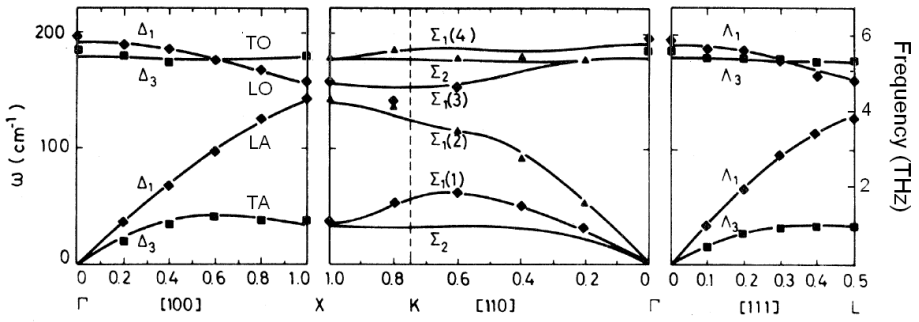

Figure 4.2: Phonon-dispersion curves in InSb along the high-simmetry directions Δ, Σ and Λ, taken from [64]. The solid lines are the calculated dispersion curves, whereas the points are the experimental values obtained by inelastic neutron scattering. Along the Σ direction the six phonon branches are disentangled.

tions Δ ([100]), Σ ([110]) and Λ ([111]) [64]. Since there are two atoms per primitive unit cell, six phonon branches occur. These consist of three acoustic phonon branches and three optical phonon branches, which can be classified as transverse or longitudinal according to whether their displacement is perpendicular or parallel to the direction of the wave vector. Along the direction (110) the six phonon branches are non degenerate. At wave vectors around the zone edges X and L the transverse acoustic (TA) phonons have much lower energies than the longitudinal acoustic (LA) phonon and display relatively flat dispersion curves. Furthermore, near the zone center the longitudinal optical (LO) phonon and the transverse optical (TO) phonon are nondegenerate as it happens for the TA and the LA phonons. The LO phonon energy is higher than that of the TO phonons. Conversely, the TO phonons have energies higher than the LO phonons near the zone edge and exhibit a moderately flat dispersion along the three high-symmetry directions.

Due to the lack of inversion symmetry in the InSb crystal, phonons can be excited optically by Raman scattering and also by infrared radiation. Single-phonon and multi-phonon processes in InSb have been extensively investigated by far-infrared absorption [35, 71, 112] and second-order Raman scattering. Figure 4.3 shows the Raman spectrum of InSb measured by Kiefer et al. [64] using 647 nm laser excitation nearly resonant with the E_1 valence-to-conduction band transition. It exhibits a very strong one-phonon scattering peak at 5.45 THz corresponding to the zone-center TO phonon. The one-LO-phonon scattering at 5.8 THz appears relatively weak. In addition to the one-phonon peaks, the Raman spectrum of InSb displays several weaker features, which are caused by

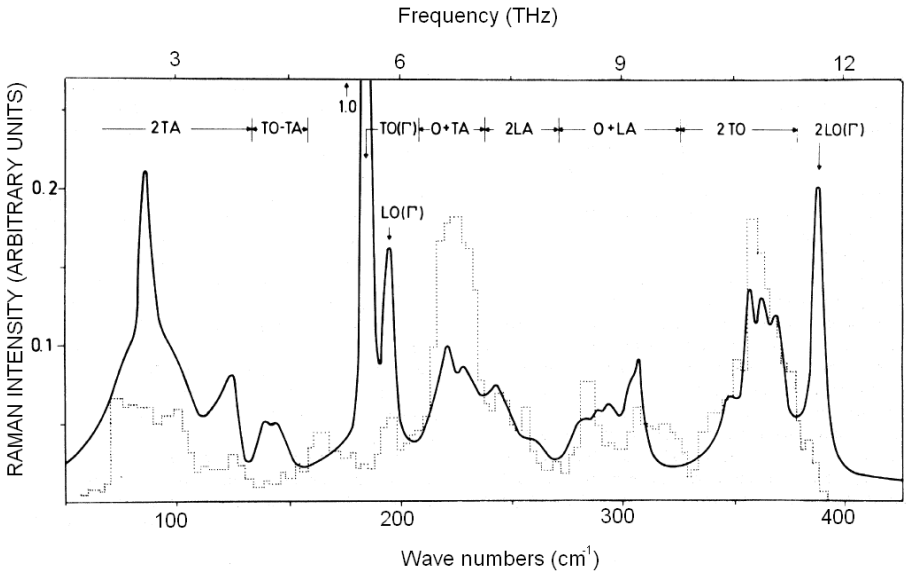

Figure 4.3: Second-order Raman spectrum of InSb obtained by Kiefer et al. [64] at 80 K with 647-nm radiation (solid lines) nearly resonant with the E_1 gap at 1.9 eV . It contains the components with Raman symmetry $\Gamma_1 + \frac{4}{3}\Gamma_{15}$. Beside the first-order TO at 183 cm^{-1} ($\approx$ 5.45 THz) and LO phonons at 194 cm^{-1} ($\approx$ 5.8 THz), phonon overtone and phonon combination bands are observed. The assignment of such bands is also given. Combined two-phonon-sum density of states (dotted lines).

two-phonon Raman scattering. Such a second-order light scattering process is connected to phonon pairs. For two phonons of different branches, scattering peaks occurring at frequencies $\nu_i + \nu_j$ and $\nu_i - \nu_j$ (i and j define the type of phonon) are due to combination and difference modes, respectively. In case the two phonons are identical, i.e., they belong to same branch, the peaks are called overtone. In the Raman spectrum of InSb shown in Fig. 4.3 the assignment of each peak is also indicated.

Unlike the one-phonon Raman scattering, the phonon wavevector in two-phonon scattering is not restricted to the zone center. The conservation of the wavevector requires that

$$q_1 + q_2 = 2k \approx 0 \tag{4.1}$$

where q_1 and q_2 are the wavevectors of the two phonons and k is the photon wavevector. Equation 4.1 implies that phonons through the whole Brilluoin zone can be excited in second-order Raman scattering. As a consequence, the second-order Raman spectrum of InSb is correlated to the two-phonon density

of states (dotted line in Fig. 4.3). Furthermore, the strength of the second-order resonant peaks is connected to the interaction of the two involved phonons with virtual electron-hole pairs which mediate the Raman scattering. An analysis of such peaks has allowed to estimate the corresponding electron-two-phonon deformation potentials which describe such interaction [64].

The two-phonon modes in InSb represent prototypical quantum excitations being ideal for investigating the dynamics of two-quantum coherences. The basic laws of quantum mechanics allow for phase-coherent superposition of different quantum states. Quantum coherences can be driven by an optical electric field that interacts resonantly with the allowed transition dipole moment between two states of a system. Not only the generation but also the coherent control of such one-quantum coherences on electronic and also vibrational transitions have been the subjects of extensive experimental studies [47, 97]. Ultrafast time-resolved four-wave mixing spectroscopy on exciton and intersubband excitations has provided valuable insight in the interaction processes occurring in the femto- to picosecond time regime that destroy the coherence.

Much less work has been carried out on two-quantum coherences mainly because they are connected to spectroscopically dark states, e.g., in a resonant generation scheme the optical excitation of two-quantum coherence involve a dipole moment of relatively small amplitude. Recently, two-quantum two-dimensional spectroscopy has been demonstrated as a powerful technique which allows to access to quantum pathways including a two-quantum coherence [66], providing prominent insight in high-order correlations regarding many-body interactions [39, 60]. These works are mainly focused on two-quantum coherences involving excitonic resonances.

In contrast to all previous studies, we investigate the ultrafast dynamics of nonlinear two-phonon and two-photon interband quantum coherences in InSb by 2D off-resonant THz spectroscopy in the strongly nonperturbative regime of light-matter interaction.

4.2 Experiment and One-Pulse and Pump-Probe Results

We exploited fully phase-resolved collinear 2D THz spectroscopy with three pulses A, B and C for studying at room temperature the nonlinear response of a 70 μm thick (100)-oriented InSb single crystal with a low n-type doping ($n \leq 10^{16}$ cm^{-3}). The experimental setup and the 2D method have been described in detail in chapter 2. The three-pulse nonlinearly emitted field E_{NL} is deduced

from the difference:

$$E_{\mathrm{NL}}(t,T,\tau) = E_{ABC}(t,T,\tau) - E_{AB}(t,T,\tau) - E_{BC}(t,\tau) - E_{CA}(t,T,\tau) + E_A(t,T,\tau) + E_B(t,\tau) + E_C(t). \quad (4.2)$$

THz electric-field transients are displayed in Figs. 4.4(a) and 4.4(b) as a function of the real time t. Figure 4.4(a) shows the THz pulse A incident on the sample, Fig 4.4(b) the THz pulses A, B and C transmitted through the sample with their mutual delay τ and T. The real time $t = 0$ is set at the largest negative peak of pulse C. A Fourier transform of the time-dependent electric fields provides the spectra of the pulses A, B and C shown in Fig. 4.4(c). The THz pulses exhibit a sharp dip at 18 THz originating from linear absorption due to a combination resonance of 1 TA and 1 TO phonons in the silicon filters for the 800 nm radiation after the THz generation (Fig. 2.7 of chapter 2). Furthermore, the spectra show an additional pronounced peak around 10 THz, i.e., the frequency of the two-phonon resonance in the InSb sample.

4.2.1 Nonlinear Interaction with a Single Pulse

In a first series of measurements we investigated the nonlinear response of the sample induced by the THz pulse A. By comparing the transmitted with the incident THz field [Figs. 4.4(a) and 4.4(b)], we observe:

- A nearly flat decrease of the transmitted amplitude, beside the losses due to the reflection at the entrance and the exit surfaces of the sample, although the incident 22 THz pulse is nonresonant with the bandgap energy of $E_g = 0.17$ eV (corresponding to a frequency of 41 THz). According to the Fresnel equations, reflection would lead to a reduction of the amplitude to 64 %, i.e., the transmitted field amplitude would be $E = 96$ kV/cm instead of $E = 35$ kV/cm.

- An additional oscillating component appears in the transmitted field between $t = -0.6$ ps and $t = 0$ ps, which is emitted by the sample and decays within about 1 ps.

The nonlinearly emitted transient results in the strong peak around 10 THz in the transmitted spectrum [red solid line in Fig. 4.4(c)]. The incident field has nearly no spectral density at this frequency [dashed line in Fig. 4.4(c)].

As pointed out earlier, InSb exhibits a two-phonon resonance at this frequency which corresponds to a two-phonon overtone state consisting of one TO phonon with wavevectors $\vec{q}$ and a second TO phonon with vavevector $-\vec{q}$ (cf. Eq. 4.1) within the phononic dispersion curves in Fig. 4.2.

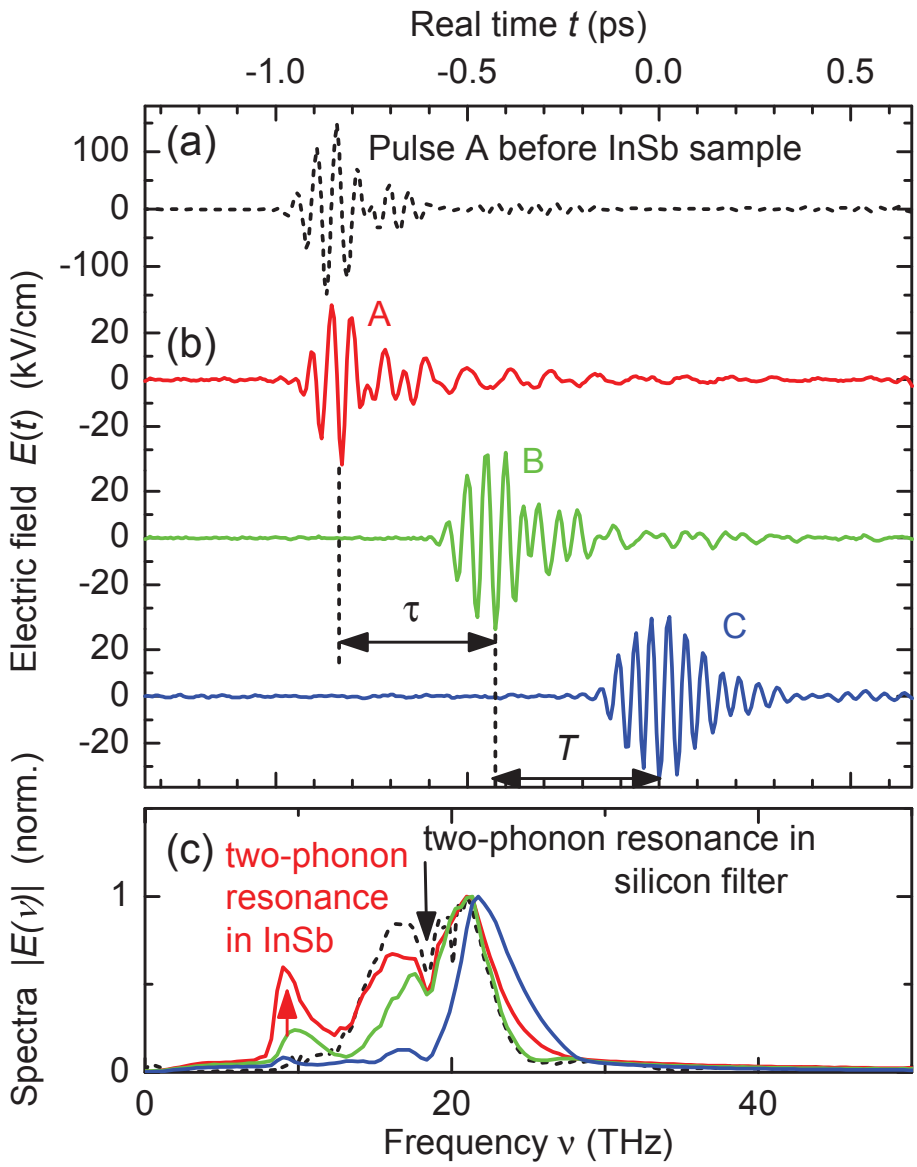

Figure 4.4: (a) Measured THz electric-field transient of pulse A impinging on the sample as function of the real time t. (b) Electric-field transients of pulses A, B and C transmitted through the InSb sample. τ is the coherence time, T the waiting time in the 2D experiment. (c) The Fourier spectra of the transmitted and incident transients show a sharp dip at 18 THz ($\approx$ 600 cm^{-1}) caused by linear two-phonon absorption [combination of 1 TO (L) and 1 TA (X) [102]] in the silicon filters after the respective GaSe crystal in Fig. 2.7 of chapter 2. The peak in the transmitted spectra around 10 THz stems from impulsive excitation of the two-phonon coherence in the InSb sample.

For a better understanding of the experimental findings it is important to remark that our experiments are in the strongly nonperturbative regime of light-matter interaction. As a consequence of the narrow bandgap, the interband transition dipole moment is extremely strong [58] with a value of $d_{cv} = e_0 \cdot 4$ nm at the Γ point, where e_0 is the elementary charge. The extraordinarily large transition dipole leads for THz electric fields of an amplitude $E = 35$ kV/cm to an interband Rabi frequency $\nu_{\mathrm{Rabi}} = Ed_{cv}/h = 3.5$ THz, which is on the same order of magnitude as the THz carrier frequency. At such field amplitude, the light-matter interaction is in the nonperturbative regime, which allows for multiple interactions of a single THz electric-field transient with the InSb sample, leading to the simultaneous occurrence of nonlinear polarizations of different nonlinear orders $\chi^{(n)}$.

The observed reduction in field amplitude is mainly caused by interband two-photon absorption [89, 99]. This is confirmed in the pump-probe experiments we have performed with pairs of THz pulses, which will be discussed below.

We now discuss the lowest order processes which contribute to the oscillating two-phonon coherences. Figures 4.5(a)-(c) display the most important corresponding interaction sequences within the electronic band structure of InSb. We adapt here the Liouville pathway diagrams of Ref. [100], introduced in Chap. 2. The "orange" line in the bandgap represents the 2TO-phonon state, whereas the dashed line a "virtual" state. For clarity, since the THz radiation is not resonant to any of the real state of the system, it is more appropriate to talk of virtual transition, i.e., a transition to a real excited state where the system stays for a short interval of time given by $\delta t \leq 1/2\pi\delta\nu$, where $\delta\nu$ is the detuning.

The diagram shown in Fig. 4.5(a) describes the linear excitation of the two-phonon coherence. For a linear generation scheme, the two-phonon transition dipole $d_{2\mathrm{ph}}$ enters during the generation of the two quantum coherence via the coupling between the two-phonon dipole and the THz electric field and the absorption strength at this frequency is proportional to $\mid N_{2\mathrm{TO}} d_{2\mathrm{ph}} \mid^2$, being $N_{2\mathrm{TO}}$ the density of the 2TO oscillators. The latter is assumed equal to the density N_{InSb} of InSb molecules in the InSb crystal. Since the dispersion of TO phonons in InSb is very flat (cf. Fig. 4.2), we assume identical anharmonic TO oscillators with the density N_{InSb}.

The value of the transition dipole of the two-phonon coherence can be deduced from the equation

$$d_{2\mathrm{ph}} = \sqrt{\frac{\hbar}{2\mu 2\pi 2\nu_{TO}} \frac{q_{\mathrm{eff}}^2 f_{\mathrm{os}}}{\varepsilon_{\mathrm{sta}} - \varepsilon_{\mathrm{inf}}}}. \tag{4.3}$$

Here, μ is the reduced mass of the two ions In and Sb with masses m_{In} and

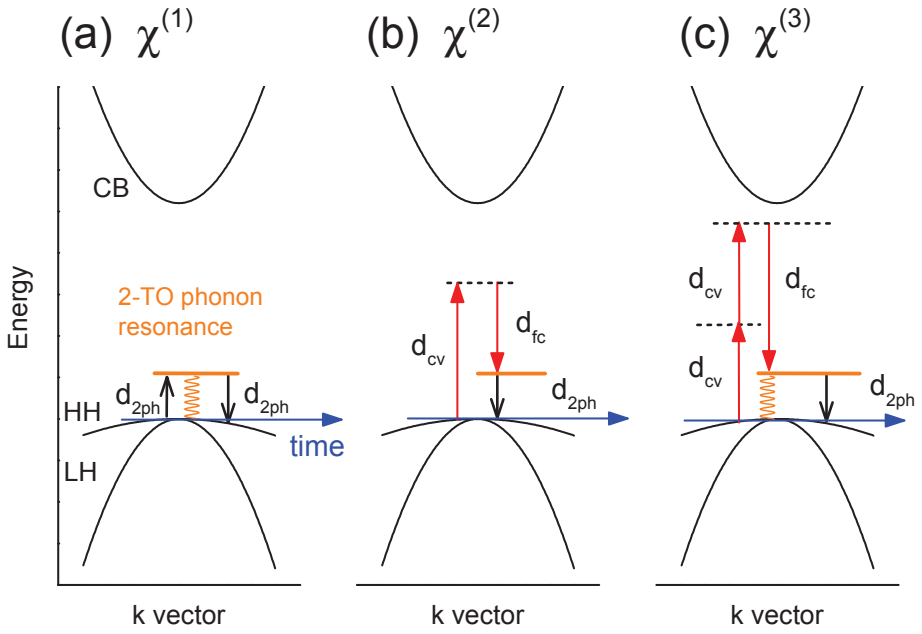

Figure 4.5: Diagrammatic representation of the interaction sequences of a single THz pulse within the electronic band stucture of InSb comprising the light hole (LH) and the heavy hole (HH) valence bands, and the conduction band (CB). The orange lines in the band gap indicates a two-phonon overtone state consisting of a TO phonon with vavevector $\vec{q}$ and a second TO phonon with vavevector $-\vec{q}$ within the phononic dispersion curves in Fig. 4.2. (a) Two-phonon quantum coherence excitation by linear resonant absorption. (b) Resonant difference frequency mixing leading to two-phonon quantum coherence emission. (c) Impulsive excitation of the two-phonon resonance via three interactions (hyper-Raman excitation.)

m_{Sb}, respectively ($\mu^{-1} = m_{\mathrm{In}}^{-1} + m_{\mathrm{Sb}}^{-1}$); ν_{TO} is the frequency of the TO phonons in InSb; $\varepsilon_{\mathrm{sta}}$ and $\varepsilon_{\mathrm{inf}}$ are the low frequency (static) and the high frequency dielectric constants; f_{os} is the oscillator strength of the valence-to-2TO phonon state transition; q_{eff} is an effective ionic charge on the ions and is typically expressed in terms of measurable quantities [109]:

$$q_{\mathrm{eff}} = \sqrt{\frac{\epsilon_0 \mu (\varepsilon_{\mathrm{sta}} - \varepsilon_{\mathrm{inf}})}{N_{\mathrm{InSb}}}} 2\pi\nu_{\mathrm{TO}} \tag{4.4}$$

with ϵ_0 the vacuum permittivity. As a remark, the second fraction in Eq. 4.3 is the effective charge related to the 2TO phonon. The oscillator strength f_{os} can be derived from the mid-infrared absorption strength measured at 10 THz [35]. The absorption coefficient α is related to the imaginary part of the refractive index $\tilde{n}$ by

$$\alpha = 4\pi\Im[\tilde{n}]/\lambda_0, \tag{4.5}$$

where λ_0 is the wavelength of the THz radiation in vacuum. The refractive index $\tilde{n}$ is in turn related to the dielectric function $\varepsilon(\nu)$ by

$$\tilde{n} = \sqrt{\varepsilon(\nu)}. \tag{4.6}$$

For our purpose, we consider an ensemble of two oscillators, one at the frequency ν_{TO} the other at $\nu_{\mathrm{2TO}} = 2\nu_{\mathrm{TO}}$, and we calculate the absorption coefficient from the following dielectric function:

$$\varepsilon(\nu) = \varepsilon_{\mathrm{inf}} + \frac{(\varepsilon_{\mathrm{stat}} - \varepsilon_{\mathrm{inf}})\nu_{\mathrm{TO}}^2}{\nu_{\mathrm{TO}}^2 - \nu^2 + 2\imath\gamma_1\nu} + \frac{f_{\mathrm{os}}\nu_{\mathrm{TO}}^2}{\nu_{\mathrm{2TO}}^2 - \nu^2 + 2\imath\gamma_2\nu}, \tag{4.7}$$

where γ_1 and γ_2 are the damping constant for the TO and 2TO phonons. The oscillator strength f_{os} and the damping constant γ_2 have been adjusted in order to fit the lattice absorption in InSb around 10 THz measured by Fray et al. [35]. Taking the values listed in Tab. 4.2 we obtain an extremely small transition dipole moment of $d_{\mathrm{2ph}} \backsimeq e_0 \cdot 220$ fm, resulting in an two-phonon coherence in the density matrix $p_{\mathrm{2ph}}^{(1)} \approx d_{\mathrm{2ph}} E \Delta t/\hbar = 2.2 \times 10^{-4}$, where $E = 35$ kV/cm is the amplitude of the driving field and $\Delta t = 200$ fs the pulse duration.

The two-phonon transition dipole can be alternatively estimated from

$$\alpha_{\nu_{\mathrm{2TO}}} = \frac{2N_{\mathrm{InSb}}\nu_{\mathrm{2TO}}}{\varepsilon_0 n \hbar \Delta\nu} d_{\mathrm{2ph}}^2, \tag{4.8}$$

where ε_0 is the vacuum permittivity and $\alpha_{\nu_{\mathrm{2TO}}}$ the absorption coefficient at the 2TO phonon frequency ν_{2TO} of an ensemble of two-level systems with a transition frequency ν_{2TO}, a transition dipole d_{2ph} and linewidth $\Delta\nu$ embedded in a dielectric medium with refraction index n [45]. Substituting in Eq. 4.8 the

μ [amu]	N_{InSb} [cm^{-3}]	$\varepsilon_{\mathrm{sta}}$	$\varepsilon_{\mathrm{inf}}$	n	q_{eff} [e$_0$]
59	1.47×10^{22}	17.7	15.6	4	2.4
Fitting parameters					
	f_{os}	γ_1 [THz]	γ_2[THz]		
	23×10^{-4}	0.01	0.28		
2TO IR Absorption [35]					
	$\alpha_{\nu_{2\mathrm{TO}}}$[mm^{-1}]		$\Delta\nu$[THz]		
	0.73		0.48		

Table 4.2: Physical parameters of the narrow-bandgap semiconductor InSb for calculating the two-phonon transition dipole moment $d_{2\mathrm{ph}}$.

respective values listed in Tab. 4.2 we obtain the same value $d_{2\mathrm{ph}} = e_0 \cdot 220$ fm for the two-phonon transition dipole moment, as previously calculated from Eq. 4.3.

By virtue of its lack of inversion symmetry, InSb also exhibits nonlinear susceptibilities $\chi^{(2)}$, $\chi^{(4)}, \ldots$, of an even order. As a consequence, two-phonon coherences can, in principle, be induced by two-phonon-resonant difference frequency mixing. Figure 4.5(b) describes such a $\chi^{(2)}$ mechanism. It is characterized by two interactions with the THz pulse on the ket side of the density matrix. The first interaction via d_{cv} causes a "virtual" transition to an excited electronic state in the conduction band, and, then, the second interaction couples such excited state to the two-phonon state via the Frank-Condon transition dipole moment d_{fc}, so involving a vibronic transition. Once excited, the oscillating two-phonon coherence emits at 10 THz involving the two-phonon dipole moment $d_{2\mathrm{ph}}$. However, all even orders do not contribute to the observed nonlinear signal since in our experimental configuration with a (100)-oriented InSb crystal and a THz linearly polarized driving field the underlying even-order nonlinear polarization does not emit radiation in the propagation direction of the THz driving field. Therefore, the emitted radiation does not contain nonlinear polarizations of even order. In fact, as a result of the selection rules of point group $\bar{4}3m$, the nonzero components of even-order susceptibilities are, e.g., $\chi^{(2)}_{xyz}$, $\chi^{(4)}_{xyzzz}$ and $\chi^{(6)}_{xyyyzzz}$ [33].

Finally, Fig. 4.5(c) displays a $\chi^{(3)}$ mechanism where the two-phonon coherence is impulsively excited via three interactions with the THz pulse on the ket side of the density matrix. Such excitation scheme involves combined electronic/vibronic transitions. Again, the two-phonon transition dipole moment $d_{2\mathrm{ph}}$ enters only in the coherent emission. As a consequence, in contrast to the

linear case the two-phonon coherence is mediated by the large interband and Frank-Condon transition dipoles. From the InSb Raman spectrum shown in Fig. 4.3, we estimate the dipole moment $d_{\rm fc} \approx 0.1 d_{\rm cv} = e_0 \cdot 0.4$ nm. The two-phonon coherence in the density matrix is $p^{(3)}_{\rm 2ph} \approx (d_{\rm cv} E_{\rm THz}/h\delta\nu)^2 d_{\rm fc} E_{THz} \Delta t/\hbar$ $= 4 \times 10^{-2}$ with the detuning $\delta\nu \approx 10$ THz. Therefore, such nonlinear process induces two-phonon coherences much larger in amplitude than the linear response.

4.2.2 Pump-Probe Signals with a Pair of THz Pulses

As already pointed out, one of the most relevant processes in our experiments on InSb is two-photon absorption due to the very strong interband transition dipole moment $d_{\rm cv}$. To support this interpretation, we have performed pump-probe experiments for various pump-pulse amplitudes. The pump-probe signal for two THz pulses is derived from

$$E^{\rm pp}_{\rm NL}(t, t_D) = E_{\rm AB}(t, t_D) - E_{\rm A}(t, t_D) - E_{\rm B}(t), \tag{4.9}$$

where t and t_D are the real time and the pump-probe delay, respectively. The nonlinear signal $E^{\rm pp}_{\rm NL}$ contains both the $\rm A_{pump}B_{probe}$ signal and the $\rm B_{pump}A_{probe}$ signal. As described in chapter 2, we separate the two signals in the 2D frequency domain by appropriate filters and then transform their individual contribution back to the time domain. The transient absorption change as a function of the pump-probe delay t_D is given by

$$\Delta A(t_D) = -\ln\left(\frac{\int_{-\infty}^{\infty} dt \mid E_{\rm probe}(t, t_D) + E^{\rm pp/filter}_{NL}(t, t_D) \mid^2}{\int_{-\infty}^{\infty} dt \mid E_{\rm probe}(t, t_D) \mid^2}\right), \tag{4.10}$$

where $E_{\rm probe}(t, t_D)$ and $E^{\rm pp/filter}_{NL}(t, t_D)$ are the probe pulse and the filtered pump-probe signal, respectively. The absorption change $\Delta A = -\ln(T/T_0)$ (T and $\rm T_0$ are the probe transmission with and without the pump excitation, respectively) for the $\rm A_{pump}B_{probe}$ (dotted line), $\rm B_{pump}A_{probe}$ (dashed line) and the $\rm C_{pump}A_{probe}$ (solid line) signal components are shown in Fig. 4.6(a). The pump-probe transients exhibit similar behaviors. A strong induced absorption occurs around $t_D = 0$. After the pulse overlap for $t_D > 0$, a smaller step-like absorption increase is observed, which decays on a time scale $T_{\rm decay} \gg 1$ ps. The amplitude of this components increases with the second power of the pump intensity. The inset in Fig. 4.6(a) shows the second-power intensity dependence of the measured absorption change ΔA. Plotting the amplitude of ΔA measured at $t_D = 0.6$ ps (filled red circle) as function of the time integral $\int \mid E_{\rm pump}(t) \mid^4 dt$

($\propto I^2_{\mathrm{pump}}$) of the different pump pulses, we find that it exactly fits a linear dependence (solid line). This experimental finding is consistent with the two-photon absorption, where one expects that the excited electron-hole density and, thus, the pump-probe signal amplitude is proportional to $\int \mid E_{\mathrm{pump}}(t) \mid^4 dt$. Since the pulses A, B and C differ in their amplitude and spectral shape, they induce a different electron-hole density resulting in a different ratio of peak amplitude and amplitude of the step-like signal. Particularly, the pump pulse C generates a larger electron-hole density because it induces a stronger two-photon absorption. Since it is centered at a higher frequency, the corresponding two-photon absorption coefficient is larger [89, 99].

We now address the interaction with the THz probe pulse. Theoretical and experimental studies on n- and p-doped InSb samples [41, 54, 62, 80] have demonstrated three possible mechanisms: (i) free-electron absorption due to intraband motion within the conduction band, (ii) free-hole absorption due to intraband motion within the HH or LH valence bands, (iii) interband absorption of holes from the HH to the LH valence bands. For an estimation of the strength of intervalence band absorption relative to mechanism (i), we compare the absorption coefficient α due to the mechanisms (i) and (iii) measured with n-doped and p-doped InSb crystals [80], respectively. For an electron density $n = 2 \cdot 10^{17}$ cm^{-3} and a hole density $p = 10^{17}$ cm^{-3}, values of $\alpha_n \simeq 9$ cm^{-1} and $\alpha_p \simeq 80$ cm^{-1} at approximately 100 meV (25 THz) were found, leading to $\sigma_{\mathrm{CB}} = \sigma_{\mathrm{HH}\rightarrow\mathrm{LH}}/18$ where σ_{CB} and $\sigma_{\mathrm{HH}\rightarrow\mathrm{LH}}$ are the cross section for the mechanisms (i) and (iii), respectively. Thus, holes make the dominant contribution to the total absorption of the THz probe pulse.

In Fig. 4.6(b) (i) we show the contribution to the pump-probe signals corresponding to the mechanism (i). After the pump pulse has generated an electron-hole pair via two-photon absorption, the THz probe experiences an enhanced absorption caused by free carrier absorption. During this process a free electron from its initial state is excited to an empty state of the conduction band. Scattering with a phonon (typically a LO phonon via Fröhlich interaction [11]) or impurity is necessary to conserve energy and wavevector in this process. From a nonlinear optics point of view the pump-probe picture sketched in Fig. 4.6(b) (i) is a $\chi^{(5)}$ process due to four interactions (two on the ket side and two on the bra side of the density matrix leading to interband two-photon absorption) with the electric field of the pump pulse and one interaction on the ket side with the electric field of the probe. The loop of the Liouville pathway is closed by the interaction with a LO phonon (tilted black arrow) plus the nonlinear emitting coherent polarization (dashed black arrow, upward in this case due to its

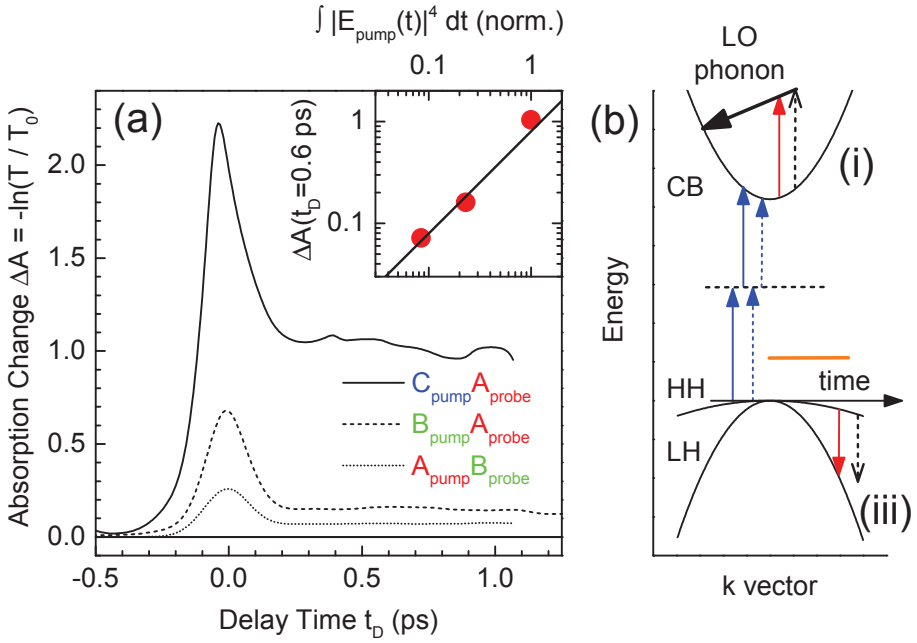

Figure 4.6: (a) Measured transient absorption change ΔA as function of the pump-probe delay t_D for both the $A_{pump}B_{probe}$ (dotted line) contribution, the $B_{pump}A_{probe}$ (dashed line) contribution and for another two-pulse combinations, e.i., the $C_{pump}A_{probe}$ (solid line) signal. Inset: red circle is the absorption change at $t_D = 0.6$ ps as a function of $\int \mid E_{pump}(t) \mid^4 dt$, the solid line the corresponding linear fit. (b) Interaction pathway contribution leading to two-pulse pump-probe signals measured in InSb. The interaction sequence in Liouville space created by the THz pump pulse involves four interactions causing a creation of an electron-hole pair via two-photon absorption. The THz probe pulse experiences both excited state absorption (ESA) due to free carrier absorption in the conduction band (CB) of InSb and intervalence absorption of holes. For momentum conservation the ESA requires a third particle, which is typically a longitudinal optical (LO) phonon (tilted black arrow).

absorptive nature). Finally, the stronger enhancement of the probe absorption during the pulse overlap, i.e., the peak around $t_D = 0$, is probably caused by a $\chi^{(3)}$ process, where the pump pulse interacts twice on ket side, whereas the probe only once on the bra side (see Fig. 4.9).

4.3 Three-Pulse 2D THz Spectroscopy

Results of the three-pulse 2D experiments are presented in Fig. 4.7. Figure 4.7(a) displays a contour plot of the electric-field transients $E_A(t,T,\tau) + E_B(t,T) + E_C(t)$ transmitted through the InSb sample as function of the real time t and the coherence time τ for a waiting time of $T = 35$ fs. All contour plot presented in the following are normalized to their respective maximum signal. From Eq. 4.2 we retrieved the corresponding nonlinear signal $E_{\mathrm{NL}}(t,T,\tau)$ shown in Fig. 4.7(b). As a result of the law of causality, we observe a non-vanishing

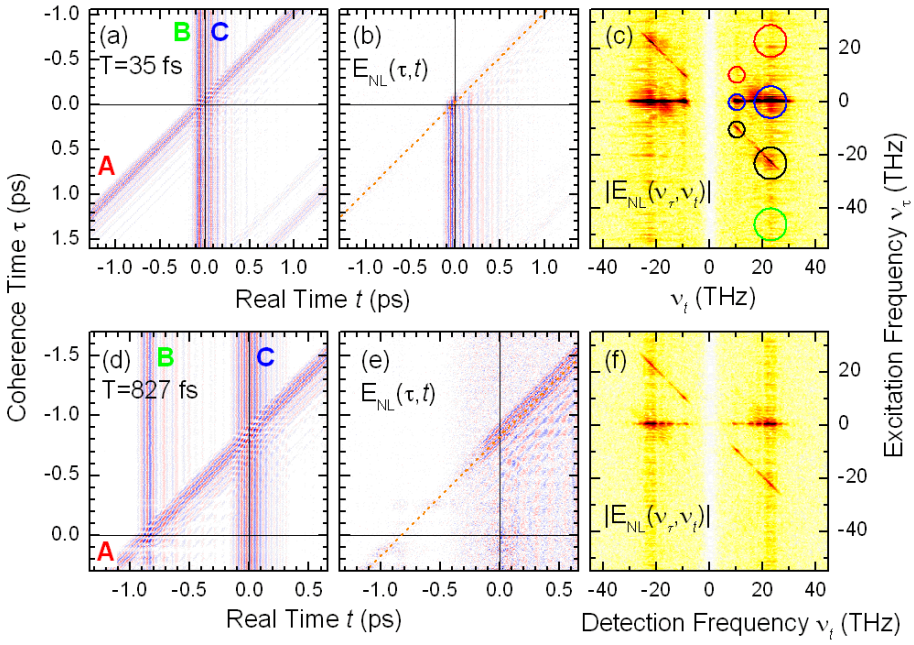

Figure 4.7: Experimental results of two-dimensional THz spectroscopy on InSb. (a) Contour plot of the electric-field transients $E_A(t,T,\tau) + E_B(t,T) + E_C(t)$ transmitted through the InSb sample as a function of the real time t and the coherence time τ for the waiting time $T = 35$ fs. (b) Nonlinear signal $E_{NL}(t,T,\tau)$ according to the Eq. 4.2. The orange dashed lines indicates the center of the pulse A. (c) Contour plot of the amplitude $\mid E_{NL}(\nu_t,\nu_\tau) \mid$, the 2D Fourier spectrum of $E_{NL}(t,T,\tau)$ as function of the detection frequency ν_t and the excitation frequency ν_τ. The colored circles indicate the position of the prominent contributions to the nonlinear signal in the 2D frequency space. Panels (d)-(f) display the same as in the panels (a)-(c) but for waiting time $T = 827$ fs. The amplitude scales of the 2D scans vary within a) $\pm$76.5 kV/cm, (b) $\pm$30 kV/cm, (d) $\pm$69 kV/cm, (e) $\pm$6 kV/cm.

$E_{\mathrm{NL}}(t,T,\tau)$ only starting with or after the respective last pulse in the timing sequence. For a comparison of the phase-front orientation between the pulse A and the nonlinear signal, we display the center of pulse A as an orange dashed line, which intersects the horizontal $\tau = 0$ black line at $t = -T$. The vertical black line at $t = 0$ indicates the center of pulse C. A 2D Fourier transform of $E_{\mathrm{NL}}(t,T,\tau)$ along t and τ provides the 2D spectrum $\mid E_{\mathrm{NL}}(\nu_t,\nu_\tau) \mid$ shown in Fig. 4.7(c) as a function of the detection frequency ν_t and the excitation frequency ν_τ. Since the pulses B and C have a fixed pulse separation $T = t_C - t_B$ in our 2D scans, the ν_T component of the frequency vectors cannot be accessed, i.e., does not play any role. The circles of different sizes and colour indicate the positions of prominent contributions to the nonlinear signal in the 2D frequency space. The 2D spectrum exhibits strong contributions occurring in the spectral range of the driving pulses 15 THz $< \nu_t <$ 25 THz (large circles) and at frequency of the 2TO phonon resonance $\nu_t = 10$ THz (small circles). The nonlinear signal E_{NL} has no spectral feature at the frequency of one-phonon resonance around $\nu_t = 5$ THz due to the reststrahlen band of the InSb sample in this frequency range. Regarding the excitation frequency ν_τ, the nonlinear signal displays relevant contributions for $\nu_\tau = 0$ (blue circles), $\nu_\tau = +\nu_t$ (red circles), $\nu_\tau = -\nu_t$ (black circles) and $\nu_\tau = -2\nu_t$ (green circle). Figures 4.7(d)-(f) show the corresponding 2D scans and 2D spectrum for a waiting time of $T = 827$ fs. To extract and individually analyze the single contributions occurring at different frequency vector $\nu = (\nu_t,\nu_\tau)$, we applied the procedure introduced in Chap. 2. The results shown in Figs. 4.8 and 4.11 correspond to the nonlinear signals centered at a frequency vector $\nu = (22\ \mathrm{THz},\nu_\tau)$, i.e., nonlinear contributions occurring at a detection frequency ν_t close to the maxima of the THz pulses, whereas results for $\nu = (10\ \mathrm{THz},\nu_\tau)$ will be shown and discussed in Sec. 4.3.2.

4.3.1 Nonlinearly Emitted Field at Frequencies of The Driving Pulses

The extracted nonlinear signals according to the large circles in Fig. 4.7(c) for waiting time $T = 35$ fs are displayed in Figs. 4.8(a)-(c), whereas the data for $T = 827$ fs are shown in Figs. 4.8(d)-(f). The orientation of the various nonlinear signals depends on the excitation frequency ν_τ. For $\nu_\tau = 0$ [Figs. 4.8(a) and 4.8(d)], the respective nonlinear signals are characterized by vertical phase fronts and, therefore, have a nonrephasing character. For $\nu_\tau = -\nu_t = -22$ THz [Figs. 4.8(b) and 4.8(e)], the phase fronts of the respective nonlinear signals are parallel to those of pulse A. Hence, also those contributions are nonrephasing

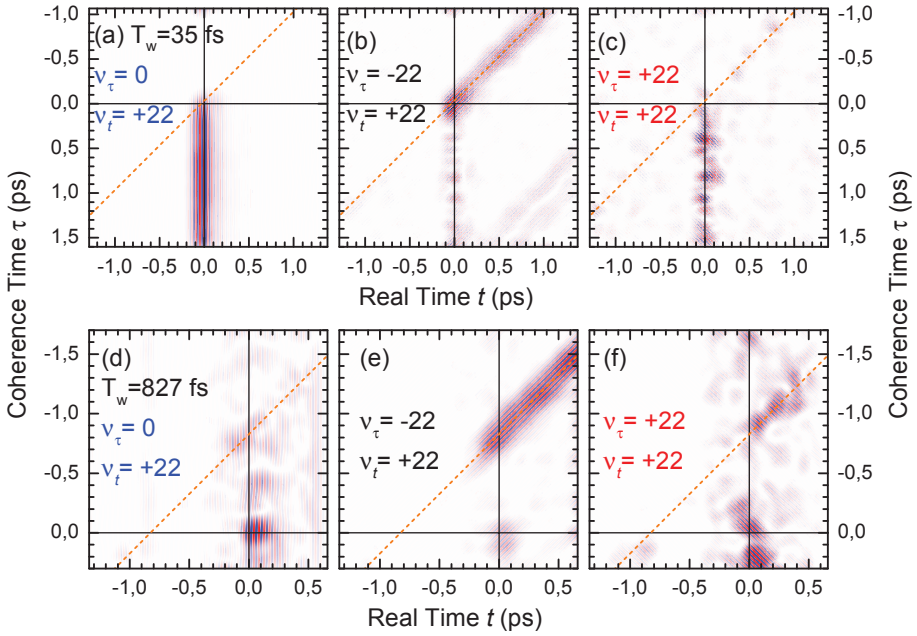

Figure 4.8: Emitted nonlinear signals corresponding to different frequency vectors ($\nu_t = 22$ THz, ν_τ), [large colored circles in Fig. 4.7(c)] as function of the real time t and the coherence time τ. The orange dashed line indicates the center of pulse A. Panels (a)-(c) display experimental results for waiting time $T = 35$ fs, panels (d)-(f) for waiting time $T = 827$ fs. Panels (a) and (d) display non-rephasing signals with vertical phase fronts, i.e., $\nu_\tau = 0$. Panels (b) and (e) display non-rephasing signals with phase fronts parallel to those of pulse A, i.e., $\nu_\tau = -\nu_t$. Panels (c) and (f) display rephasing signals with phase fronts perpendicular to those of pulse A, i.e., $\nu_\tau = \nu_t$. The amplitude scales vary within (a) ±5.2 kV/cm, (b) ±0.8 kV/cm, (c) ±0.35 kV/cm, (d) ±0.27 kV/cm, (e) ±0.585 kV/cm, and (f) ±0.105 kV/cm.

signals. For $\nu_\tau = +\nu_t = +22$ THz [Figs. 4.8(c) and 4.8(f)], the respective nonlinear contributions have phase fronts perpendicular to those of pulse A and, thus, are rephasing signals. Figure 4.11 shows nonlinear signals exhibiting tilted phase fronts according to $\nu_\tau = -2\nu_t = -44$ THz. Please note, for all frequency vectors $\nu = (22\ \text{THz}, \nu_\tau)$ the nonlinear emitted field is characterized by short electric-field transients along the real time t, which are generated during the interaction with the respective last pulse, i.e., pulse A for $\tau < -T$ and pulse C for $\tau > -T$. Such a behavior is mainly caused by the fact that the interaction with the last pulse involves a transition from a virtual to a real state where energy conservation can be violated for a short time interval $\delta t \leq 1/2\pi\delta\nu$ according to Heisenberg's uncertainty principle. For a detuning of $\delta\nu \approx 20$ THz, we obtain $\delta t \approx 8$ fs. Figure 4.9 displays the lowest-order Liouville pathways which can lead to the observed nonlinear contributions. They are characterized by multiple interactions of a single pulse (A, B, or C) with the InSb sample, due to the fact that the light-matter interaction is in the nonpertubative regime.

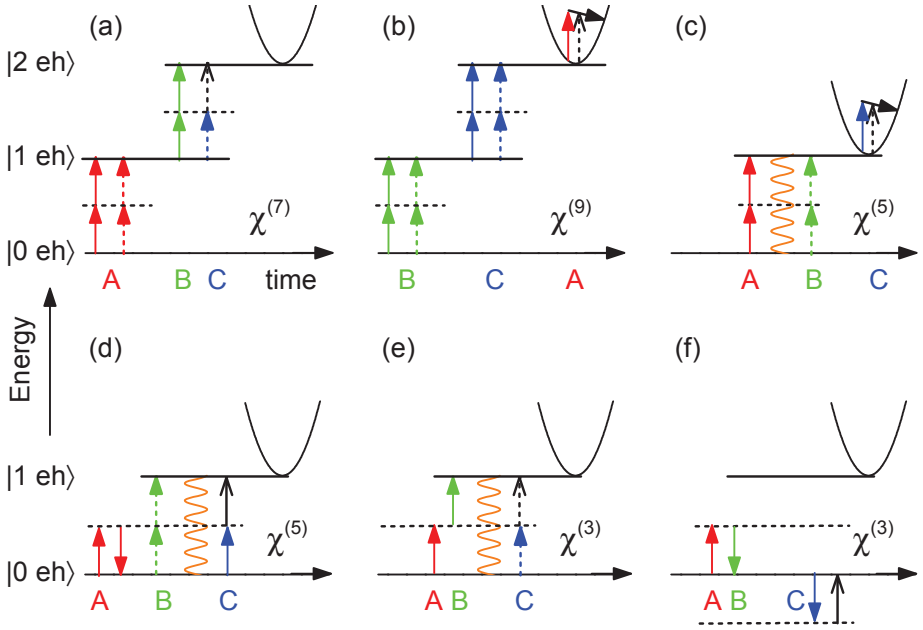

Figure 4.9: Lowest-order Liouville pathways leading to the nonlinear signals displayed in Figs 4.7 and 4.11. Horizontal solid lines: "real" states with no $|\ 0\,\text{eh}\ >$, one $|\ 1\,\text{eh}\ >$, and two-photo-induced electron-hole pairs $|\ 2\,\text{eh}\ >$ in InSb. Horizontal dashed lines: "virtual" intermediate states. Parabola and tilted black arrow represents intraband excitation of conduction band electrons. The orange wavy lines represent the optically dark two-photon coherence in Insb.

We now discuss the evolution of the nonlinear nonrephasing signals centered at the frequency vector $\nu = (22\ \text{THz}, -22\ \text{THz})$ as function of the coherence time τ. For $\tau < -T$, the nonlinear contributions shown in Figs. 4.8(b) and 4.8(e) display an amplitude almost independent from the coherence time. This implies that in the corresponding diagrams the density matrix evolves along τ in a population state (bra and ket side are in the same state) instead of coherences, i.e., coherent quantum mechanical superpositions, as expected for nonlinear signals within the $\chi^{(3)}$ limit of the light-matter interaction. Outside the overlap temporal range of pulses A, B and C, the diagram shown in Fig. 4.9(b) accounts for these two nonlinear signals. Pulse B induces a two-photon interband absorption, thereby generating a first electron-hole pair. Afterwards, pulse C creates a second electron-hole pair. Pulse A then probes ESA due to the intraband motion within the conduction band. From a nonlinear optics point of view such a scenario corresponds to a $\chi^{(9)}$ process where the first two pulses both interact four times whereas the last one only once with the InSb sample. Such an interaction sequence is also consistent with the phase-front orientation of the observed nonlinear signals. The respective nonlinear polarization with a frequency vector $\vec{\nu}_{\text{NL}} = (2\vec{\nu}_B - 2\vec{\nu}_B) + (2\vec{\nu}_C - 2\vec{\nu}_C) + \vec{\nu}_A$ leads to the emission of a nonlinear signal with phase fronts parallel to those of pulse A. To support our interpretation we compare nonlinear transients measured at different waiting times T. For this, in Fig. 4.10(a) we plot the transients shown in Figs. 4.8(b) and 4.8(e) taken at the respective coherence time $\tau = -T - 165$ fs for $T = 35$ fs (dashed line) and for $T = 827$ fs. The two nonlinear transients exhibit an identical amplitude of $E_{\text{NL}} \approx 0.4$ kV/cm and identical phase. Therefore, pulse A generates a free carrier absorption signal which does not depend on the temporal separation of the pulses B and C. Additionally, it is also independent from the pulse separation between C and A, as a result of the large lifetime of the photo-excited carriers.

In Fig. 4.8(b) around $\tau = 0$, we observe a stronger nonlinear signal due to the temporal overlap of all pulses that allows for additional contributions of lower orders, e.g., $\chi^{(3)}$ is the lowest-order nonlinearity. One of the possible corresponding diagrams is displayed in Fig. 4.9(e). It involves the generation of a two-photon interband coherence by a concerted action of pulses A and B. Such a diagram also accounts for the signal observed in Fig. 4.8(e) around $\tau = 0$, i.e., for the temporal overlap of pulses A and B.

We now address the nonlinear signals centered at the frequency vector $\nu = (22\ \text{THz}, 0)$. We concentrate on the positive τ. The nonlinear signal displayed in Fig. 4.8(a) is characterized by an amplitude that remains almost constant when varying the coherence time τ. Again, the scenario of the diagram Fig. 4.9(b) is

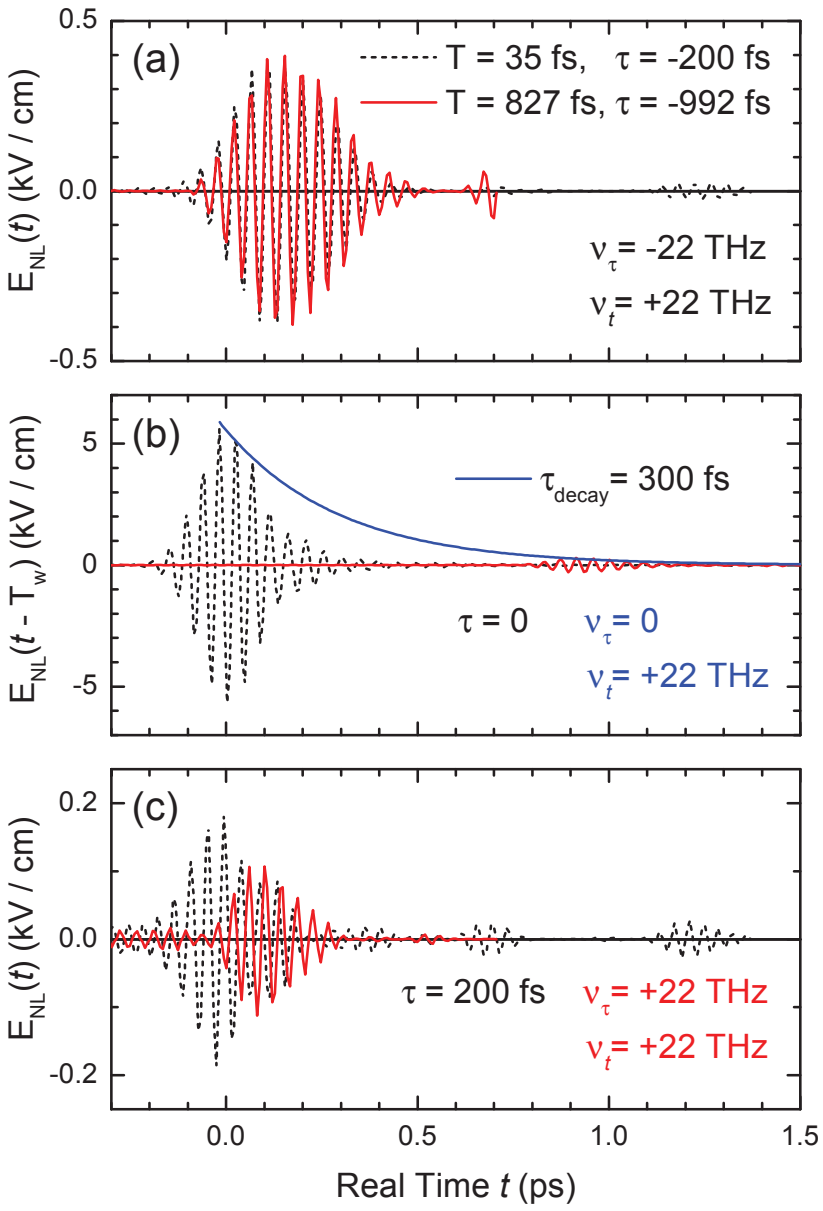

Figure 4.10: Direct comparison of the nonrephasing electric-field transients displayed in Figs. 4.7(b) and 4.7(e) taken at the respective coherence time $\tau = -T - 165$ fs for $T = 35$ fs (dashed line) and $T = 827$ fs (solid line). (b) Direct comparison of the nonrephasing electric-field transients displayed in Figs. 4.7(a) and 4.7(d) taken at $\tau = 0$. For an easier comparison of the transients at two waiting times T we plot them here shifted in time by T. The blue curve is the fit for the amplitude decay. (c) Direct comparison of the nonrephasing electric-field transients displayed in Figs. 4.7(c) and 4.7(f) taken at $\tau = 200$ fs.

expected but with different pulse sequence ABC. However, due to the temporal overlap of pulses B and C an additional $\chi^{(7)}$ order contribution to the nonlinear signal is possible. The corresponding pulse interaction sequence is depicted in the Liouville pathway of Fig. 4.9(a). Pulse A interacts four times, pulse B twice, and pulse C only once with the InSb sample. The corresponding nonlinear polarization has a frequency vector $\vec{\nu}_{\mathrm{NL}} = (2\vec{\nu}_A - 2\vec{\nu}_A) + (2\vec{\nu}_B - \vec{\nu}_C)$ emitting a nonlinear signal characterized by vertical phase fronts, as observed in Fig. 4.8(a). The two-photon absorption, generating the second electron-hole pair, arises from the concerted interaction of both pulses B and C. Again, when all pulses overlap for $\tau = 0$, additional contributions of lower orders can arise. However, $\chi^{(5)}$ is the lowest-order nonlinearity. Since pulse A has tilted phase fronts, to induce a nonlinear signal with vertical phase fronts it is necessary that it interacts with sample at least twice in a way to get rid of any contribution of its phase fronts. Additionally, we measure nonlinear signals where all pulses interact at least once with the sample. Therefore, a $\chi^{(3)}$ process is ruled out. The Liouville pathway for the $\chi^{(5)}$ process is depicted in Fig. 4.9(d). According to this diagram, the frequency vector of the nonlinear polarization is $\vec{\nu}_{\mathrm{NL}} = (\vec{\nu}_A - \vec{\nu}_A) + (-2\vec{\nu}_B + \vec{\nu}_C)$. In the overlap region of two or three pulses there are many other Liouville pathways because there is not a well defined pulse sequence.

In Fig. 4.8(d) we observe an enhanced nonlinear signal around the coherence time $\tau = 0$, i.e., when pulses A and B overlap in time. It contains signal contributions arising from a $\chi^{(5)}$ process in the lowest order whose diagram is displayed in Fig. 4.9(d) as for the respective nonlinear signal at waiting time $T = 35$ fs. Pulse A interacts twice on the ket side of the density matrix. The first interaction brings the valence electron to a virtual state from which is soon de-excited by the second interaction. Pulse B interacts twice on the bra side creating a two-photon coherence between the valence and the conduction bands which evolves during the waiting time T. Then, pulse C interacts once.

To obtain information about the decay of the two-photon interband coherence along the waiting time T, we directly compare the electric-field transients of Figs. 4.8(a) and 4.8(b) taken at $\tau = 0$. For an easier comparison, in Fig. 4.10(b) the transients are shifted by their respective waiting time T. The dashed line is the electric-field transient for $T = 35$ fs, whereas the red solid line for $T = 827$ fs. Their respective amplitudes are approximately 5 kV/cm and 0.3 kV/cm. An exponential fit for the amplitude decay indicated by the blue solid line provides a time constant of $\tau_{\mathrm{decay}} = 300$ fs.

Next, we present the nonlinear response centered at the frequency vector $\nu_{\mathrm{NL}} = (22\ \mathrm{THz}, -44\ \mathrm{THz})$. In Fig. 4.11(a) the corresponding nonlinear signal

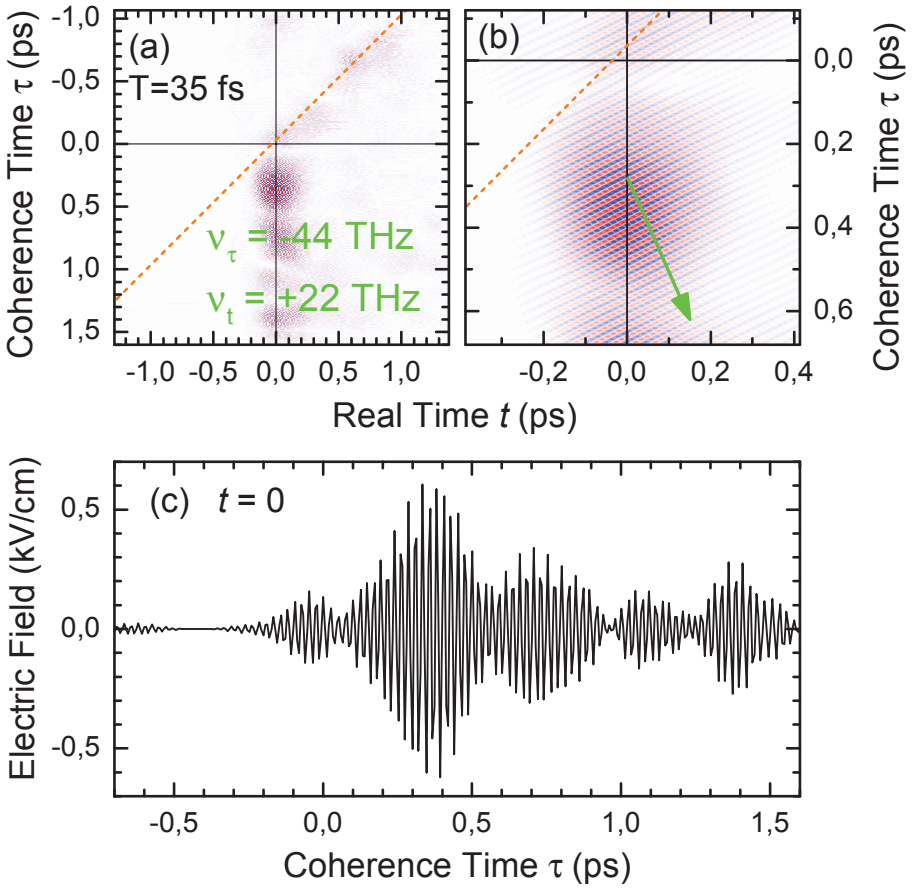

Figure 4.11: (a) Emitted nonlinear signals for waiting time $T = 35$ fs corresponding to frequency vector ($\nu_t = 22$ THz, $\nu_\tau = -44$ THz) [green circle in Fig. 4.7(c)] as function of the real time t and the coherence time τ. (b) A close view of the signal for small t and τ values. (c) Electric-field transient of the optically dark two-photon interband coherence as function of the coherence time τ (cut along $t = 0$ of panel (a)).

is displayed as function of the real time t and the coherence time τ . For a better view of the orientation of its phase fronts, we show in Fig. 4.11(b) an enlargement of the nonlinear signal for small values of t and τ. The frequency vector is depicted as a green arrow and is perpendicular to the signal phase fronts. The nonlinear emitted field mainly occurs for $\tau > 0$ and exhibits an oscillating amplitude when varying the coherence time τ. Figure 4.11(c) displays the emitted field for $t = 0$ as function of the coherence time τ. The electric-field transient oscillates with center frequency of $\nu = 44$ THz, i.e., with the frequency of the two-photon interband coherent polarization. Its amplitude of $E = 0.5$ kV/cm decays on a time scale of $\tau \approx 300$ fs. The observed oscillatory behavior with frequency of $\nu = 44$ THz along the coherence time and the decay time of $\tau \approx 300$ fs indicate that the nonlinear signal reflects the dynamics of the two-photon interband coherence.

We now address the lowest-order Liouville diagram yielding the nonlinear signal with the frequency vector located at ($\nu_t = 22$ THz, $\nu_\tau = -44$ THz). Pulse A is the only among the pulses with a nonzero excitation frequency component, i.e., $\nu_\tau = -22$ THz. As a result, it has to interact at least twice to generate the observed signal excitation frequency $\nu_\tau = -44$ THz. On the other hand, according to Eq. 4.2, each pulse has to interact at least once. Therefore, the lowest-order process is a $\chi^{(5)}$ nonlinearity, whose pathway is depicted in Fig. 4.9(c). Pulse A interacts twice on the ket side of the density matrix, pulse B twice on the bra side and pulse C once on the ket side, leading to a nonlinear polarization with a frequency vector $\vec{\nu}_{\mathrm{NL}} = 2\vec{\nu}_A - 2\vec{\nu}_B + \vec{\nu}_C$. In the interaction sequence, pulse A creates the two-photon interband coherence which evolves during the coherence time τ. Depending on the relative phase between the oscillating two-photon interband coherent dipole and the electric field of pulse B, the latter can either induce stimulated emission from the excited state or experience two-photon absorption. As a result, the number of electron-hole pairs in the excited state is modulated with the frequency $\nu_\tau = -44$ THz. Pulse C probes the intraband absorption of the photo-excited modulated electrons in the conduction band. As pointed out previously, the nonlinear signal is characterized by a decay time of $\tau_{\mathrm{decay}} = 300$ fs, implying that decoherence processes responsible for the dephasing of the two-photon interband polarization occur on an unexpectedly long time scale. One possible explanation is a strong inhibition of the electron-electron scattering at the Fermi edge [65]. However, the reasons for the observed long decoherence time are an open question because there is no theoretical investigation about microscopic dephasing mechanism of the two-photon interband coherences.

Finally, we turn to a brief discussion regarding the rephasing signals with frequency vectors at ($\nu_t = 22$ THz, $\nu_\tau = 22$ THz) displayed in Figs. 4.8(c) and 4.8(f). Figure 4.9(f) displays the only possible $\chi^{(3)}$ Liouville pathway which leads to the nonlinear signals having the phase fronts perpendicular to those of pulse A. As a consequence of the strongly off-resonant character of the diagram the nonlinear response is characterized by a very small signal. Higher-order diagrams accessing the two-photon coherence might also contribute to the rephasing signal. In Fig. 4.10(c), we show a direct comparison of the electric-field transients for $T = 35$ fs (dashed line) and $T = 827$ fs (solid line) taken at $\tau = 200$ fs. We observe a slow decay of the amplitude which is probably caused by an even longer homogeneous dephasing time of the two-photon coherent polarization. Further measurements with a better signal-to-noise ratio are necessary to clarify this issue.

4.3.2 Nonlinearly Emitted Field at Frequencies of The Two-Phonon Resonance

The contributions to the total nonlinear signal occurring at the frequency vector ($\nu_t = 10$ THz, ν_τ), shown in the 2D Fourier space of Figs. 4.7(c) and 4.7(f), correspond to the coherent response of the two-phonon resonances of InSb. The two-phonon 2D signals are measured as function of the real time t and the coherence time τ for waiting times $T = 35$ fs and $T = 827$ fs. The extracted signals on the small circles in Fig. 4.7(c) are shown in Figs. 4.12(a)-(f) as contour plots. According to their respective frequency vectors, the nonlinear signals exhibit different time structure. The contributions at frequency vectors (10 THz, 0) in Fig. 4.12(a) and (10 THz, −10 THz) in Fig. 4.12(b) display vertical phase fronts and tilted phase fronts as those of pulse A, respectively. For this reason, we refer to them as nonrephasing signals. Indeed, the contribution at (10 THz, 10 THz) in Fig. 4.12(c) is referred as rephasing signal, since it shows phase fronts perpendicular to those of pulse A. Figs. 4.12(d)-(f) display their respective nonlinear signals for waiting time $T = 827$ fs.

We first discuss the nonrephasing signals with the frequency vector $\vec{\nu}_{\mathrm{NL}} =$ (10 THz, 0). As shown in Figs. 4.12(a) and (d) for $\tau > -T$, the signal amplitude is independent from the coherence time τ. This implies that pulse A does not create the two-phonon coherence. Moreover, we observe a lower signal amplitude for $T = 827$ fs. For directly comparing the nonlinear electric-field transients for the two waiting times, we consider those taken at the coherence time $\tau = 0$ from Figs. 4.12(a) and (d), and then we plot them in Fig. 4.13(b) shifted by their respective waiting time T. We observe that the electric-field transient

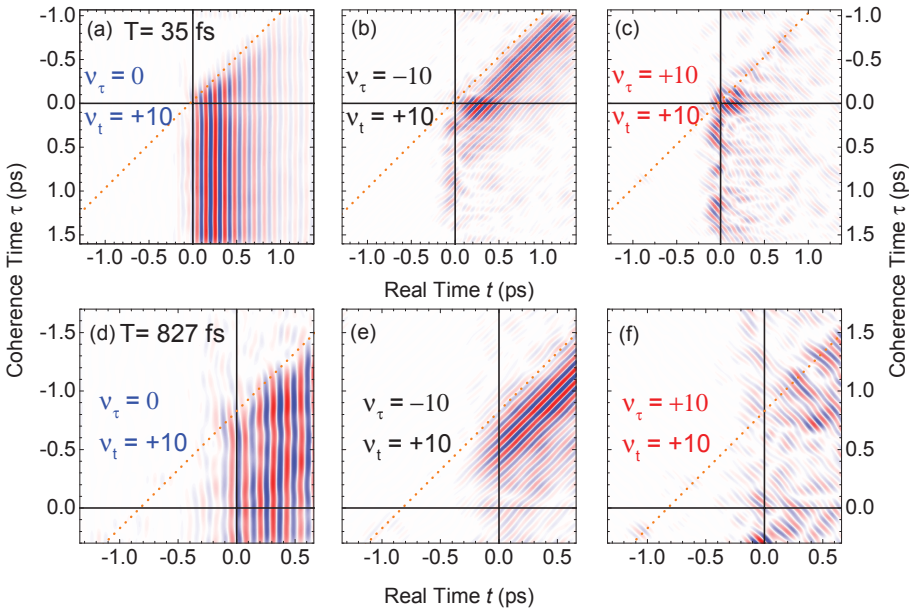

Figure 4.12: Emitted nonlinear signals at various two-phonon frequency vectors $(\nu_t = 10 \text{ THz}, \nu_\tau)$ [small colored circles in Fig. 4.7(c)] as function of the real time t and the coherence time τ for waiting times $T = 35$ fs and $T = 827$ fs. Panels (a) and (d) show the nonrephasing signal with vertical phase fronts, i.e, $\nu_\tau = 0$. Panels (a) and (d) show the nonrephasing signal with tilted phase fronts parallel to those of pulse A, i.e, $\nu_\tau = -10$ THz. Panels (c) and (f) show the rephasing contribution with phase fronts perpendicular to those of pulse A, i.e., $\nu_\tau = 10$ THz.

for $T = 827$ fs (red solid line) represents the direct continuation in amplitude and phase of the one for $T = 35$ fs (black dashed line). This points to the fact that only pulse B generates the observed oscillating two-phonon coherence which is then probed by pulse C or pulse A, according to the pulse sequences ABC ($\tau > 0$), BAC ($-T < \tau < 0$) and BCA ($\tau < -T < 0$). The signal field is emitted after the respective last pulse and its temporal evolution reflects a free induction decay. From an exponential fit of the amplitude decay indicated by the blue solid line, we derive a time constant of $\tau_{\text{decay}} = 450$ fs, which corresponds to a linewidth of $\Delta\nu = 1.1$ THz (37 cm^{-1}). This value equals the bandwidth of the 2TO-phonon density of state [cf. Fig. 4.3]. This points to the fact that the decay of the nonrephasing two-phonon polarization is caused by an inhomogeneous broadening mechanism.

We now discuss the lowest-order Liouville pathways leading to the nonlinear

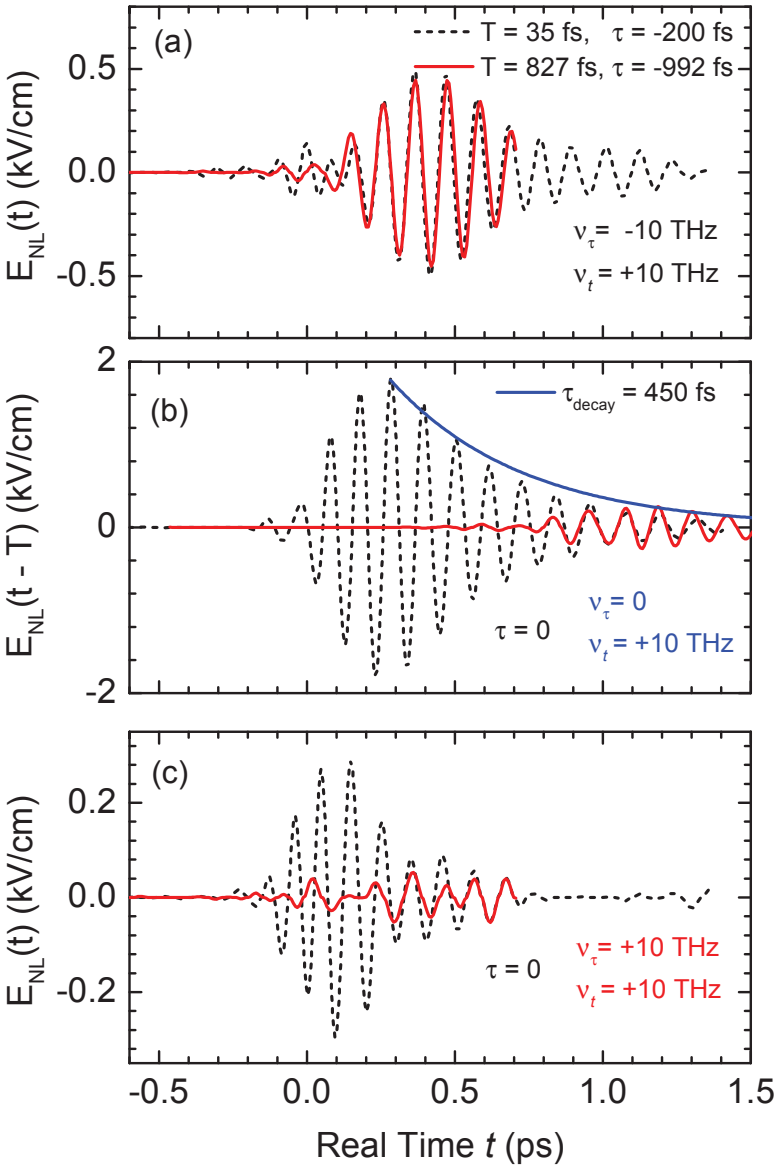

Figure 4.13: (a) Direct comparison of the nonrephasing electric-field transients displayed in Figs. 4.12(b) and 4.12(e) taken at the respective coherence time $\tau = -T - 165$ fs for $T = 35$ fs and $T = 827$ fs. (b) Comparison of the nonrephasing electric-field transients displayed in Figs. 4.12(a) and 4.12(d) taken at the coherence time $\tau = 0$ for $T = 35$ fs (dashed line) and $T = 827$ fs (solid line). For an easier comparison of the transients at two waiting times T we plot $E_{NL}(t - T)$ instead of $E_{NL}(t)$. The blue curve is the fit for the two-phonon coherence amplitude decay. (b) Direct comparison of the rephasing electric-field contributions taken at $\tau = 0$.

signal with the frequency vector occurring at ($\nu_t = 10$ THz, $\nu_\tau = 0$). Since the nonlinear signal is characterized by vertical phase fronts, pulse A has to interact an even number of times with the sample to get rid of any contributions from its tilted phase fronts. Moreover, the timing of pulses A and C does not influence the nonlinear signal. This behavior reflects the fact that both pulses just generate electron-hole pairs via two-photon interband absorption. The lowest-order diagrams for the pulse sequence ABC is depicted in Fig. 4.14(a). Pulse A generates the first electron-hole pair. After the coherence time τ, pulse B induces the two-phonon coherence. After the evolution during the waiting time T, the two-phonon coherence is transferred to a two-photon excited electron-hole pair by the pulse C. Afterwards, it evolve along the real time t radiating via its optical dipole. From a nonlinear optics point of view it represents a $\chi^{(11)}$ process. For the pulses sequences BAC and BCA, the two-phonon coherence initially generated by the pulse B is transferred to the first electronic excited state by the second pulse and then to the final electronic excited state by the last pulse [Fig. 4.14(c)].

Next, we address the nonrephasing response at (10 THz, -10 THz). In Fig. 4.12(b) for $\tau < -T$, we observe a constant signal amplitude when varying the coherence time τ, i.e., the signal amplitude does not depend from the temporal separation between pulses B and A, and between pulses C and A. We observe the same behavior in the corresponding nonlinear signal at waiting time $T = 827$ fs. Thus, the nonlinear signal is also not influenced by the pulse separation of B and C. In Fig. 4.13(a) we plot the transients displayed in Figs. 4.12(b) and 4.12(e) taken at the respective coherence time $\tau = -T - 165$ fs for $T = 35$ fs (dashed line) and $T = 827$ fs (solid line). The two nonlinear transients are identical in amplitude and in phase. As a result, only pulse A creates the two-phonon coherence, whereas the pulses B and C induce two-photon interband absorption, thus creating electron-hole pairs. Figure 4.14(b) displays the lowest-order Liouville pathways accounting for such a picture. For $-T < \tau < 0$ the overlap region of pulses ABC in Fig. 4.12(b), the nonlinear signal shows a higher amplitude. Therefore, we expect an additional lower-order contribution, i.e., a $\chi^{(7)}$ nonlinear process shown in Fig. 4.14(d). Here, the generation of the electron-hole pair is a concerted action of pulses B and C. For $\tau > 0$, we observe a lower signal amplitude as a result of the free induction decay of the two-phonon coherence. The corresponding lowest-order Liouville pathway is similar to the one in Fig. 4.14(c) but with the pulse sequence ABC.

Finally, we discuss the rephasing nonlinear signal with the frequency vector located at (10 THz, 10 THz) [Figs. 4.12(c) and 4.12(f)]. The lowest order Liou-

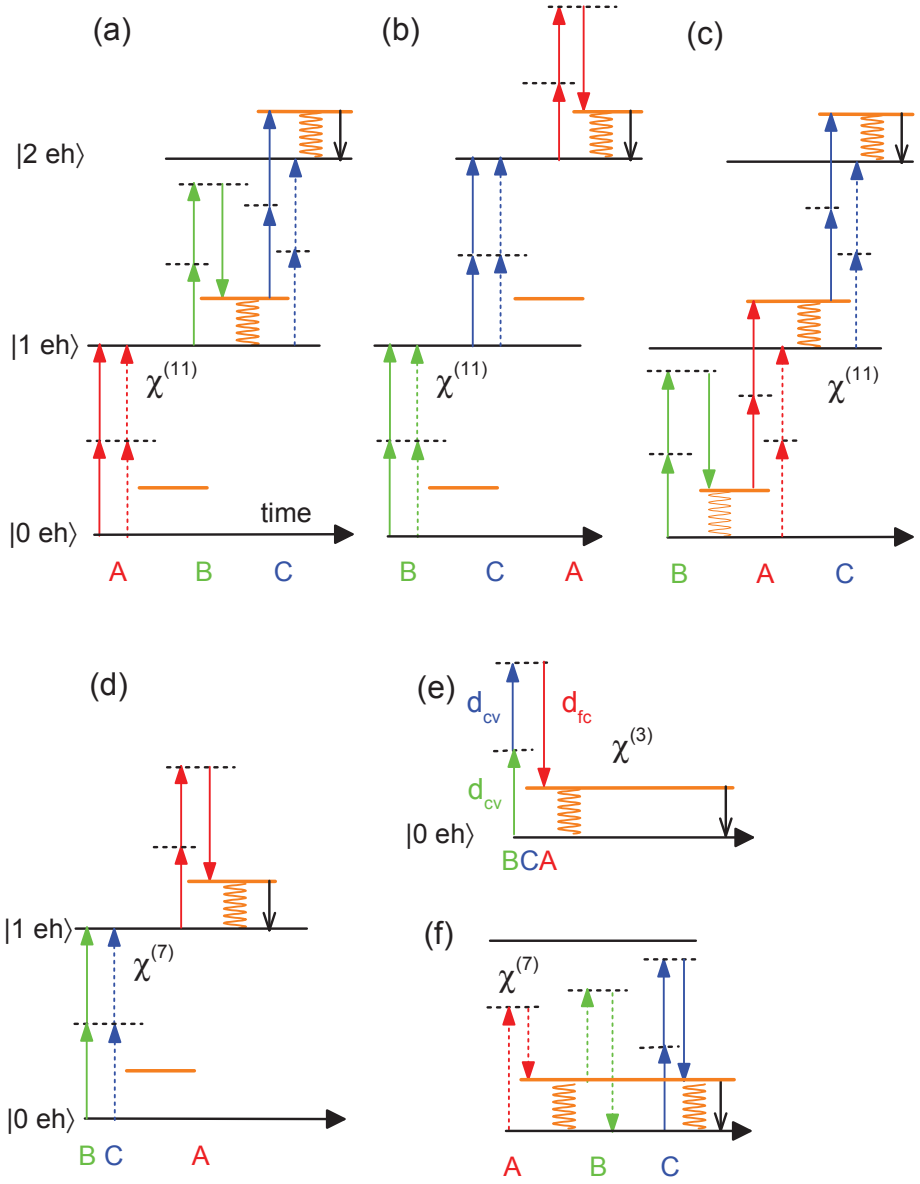

Figure 4.14: Possible Liouville pathway diagrams in the lowest order leading to the observed two-phonon nonlinear signals. Horizontal solid lines: "real" states with no $|\,0\,\mathrm{eh}>$, one $|\,1\,\mathrm{eh}>$, and two-photo-induced electron-hole pairs $|\,2\,\mathrm{eh}>$ in InSb. Horizontal dashed lines: "virtual" intermediate states. The orange wavy lines indicate the two-phonon coherence in InSb.

ville pathways leading to a rephasing two-phonon coherence is the $\chi^{(3)}$ process displayed in Fig. 4.14(e). The nature of such a diagram has already been explained in Sec. 4.2.1. Since all transitions are off-resonantly driven by pulses A, B and C, the strongest nonlinear signal occurs when all three pulses overlap, i.e., $T = 35$ fs and $\tau = 0$. The corresponding electric-field transient is shown in Fig. 4.13(c) as dashed line. On the other hand, the nonlinear signal shown in Fig. 4.12(e) exhibits a much smaller amplitude [the red solid line in Fig. 4.13(c)] at the level of the signal-to-noise ratio due to the larger separation T between pulses B and C. Here, higher-order diagrams account for the nonlinear signal. Figure 4.14(f) describes a possible interaction sequence which accesses to the two-phonon coherence twice. Pulse A excites the two-phonon coherence via difference frequency mixing. The first interaction of pulse B with the sample leads to a virtual transition from the two-phonon state to an excited electronic state via the Frank-Condon transition dipole moment d_{fc}. Then, the second interaction de-excites the system to the ground state through the interband dipole moment d_{cv}. After the waiting time T, pulse C generates the second two-phonon coherence. The nonlinear two-phonon signal is emitted via the two-phonon transition dipole moment $d_{2\mathrm{ph}}$.

4.4 Summary

In this last Chapter, we have presented the first two-dimensional THz experiment with three phase-locked THz pulses and phase-resolved detection by electro-optic sampling. The three-pulse 2D THz spectroscopy has allowed for exciting and, then, mapping in real time the coherent dynamics of two-photon interband and two-phonon excitations in the narrow-bandgap semiconductor InSb. By virtue of the extremely large interband dipole moment of InSb, the experiments were performed in the nonperturbative limit of light-matter interaction. In such a regime the THz pulses can interact a multiple number of times, allowing to access the two-quantum excitations off-resonantly. By the analysis of the 2D signal phase fronts we have identified the predominant generation mechanisms for the observed coherences. The coherent response on the two-phonon resonance is dominated by nonlinear contributions in the driving field. The relevant nonlinear generation scheme involves electronic and vibronic excitations which exploit both the large interband and Frank-Condon dipole moments. The extraordinarily small two-phonon dipole moment plays a role only during the coherent emission.

Conclusions

Nonlinear THz spectroscopy has developed into a prominent and powerful diagnostic method for exploring, e.g., under nonperturbative conditions, both the dynamics of low-energy excitations in bulk and nanostructured semiconductor and field-induced nonlinear charge transport processes on their fundamental ultrafast time scale. The coherent generation of high-field multi-octave THz pulses was investigated in an organic crystal. Multidimensional off-resonant coherent THz spectroscopy allowed to gain new insight in nonlinear charge transport and one- and two-quantum coherences of elementary excitations in bulk semiconductors.

Ultrabroadband THz generation in a DSTMS Crystal

The generation of ultra-broadband high-field THz pulses in the organic crystal DSTMS was demonstrated by non-phase-matched difference frequency mixing within the broad spectrum of amplified near infrared pulses. Phase-resolved detection via electro-optic sampling in a thin ZnTe crystal allowed to fully characterize the electric field of the generated THz pulses.

- The THz electric fields displayed an initial amplitude on the order of MV/cm that was damped on a picosecond time scale.
- The spectra covered an extraordinarily broad frequency range from approximately 0.5 THz up to 30 THz, thereby filling the so-called THz gap.

As a first spectroscopic application of this novel ultra-broadband coherent THz source, the absorption spectrum of an optically-thick DAST organic crystal was measured. The sample exhibited several vibrational absorption bands over the entire frequency range $[0.5 \div 30]$ THz. Absorption amplitudes of up to 6 OD were measured.

Field-induced Bulk Photovoltaic Effect in a $LiNbO_3$ crystal

The bulk photovoltaic effect was investigated in the prototypical ferroelectric crystal $LiNbO_3$ under nonperturbative conditions by 2D THz spectroscopy with two high-field THz pulses. The nonlinear response along the ferroelectric c-axis of an undoped $LiNbO_3$ crystal was driven by an extreme off-resonant THz electric field of amplitude 200 kV/cm. The nonlinear signal emitted by the sample exhibited electric field amplitude of up to 20 kV/cm.

The dominant contribution to the nonlinear signal was caused by an interband *shift current*, i.e., an hallmark of the bulk photovoltaic effect. The generation mechanism of such a current relied upon both the lack of inversion symmetry in the crystal structure and the nonresonant field-induced interband tunneling of charge carrier from the valence to the conduction band.

The strong THz field drives an interband coherent polarization, which dephases in few femtosecond due to the high interband decoherence rate, thereby creating charge carriers. The generation of charge carriers is related to an unidirectional charge motion owing to the asymmetric potential along the ferroelectric c-axis of the $LiNbO_3$ crystal.

Two-Phonon and Two-Photon Coherences in InSb

A 2D THz spectroscopy with three strong terahertz pulses centered at 22 THz allowed for driving multi-quantum excitations, i.e., the two-photon interband excitation at 44 THz and the two-phonon excitation at 10 THz, in the prototypical narrow-band semiconductor InSb and, then, monitoring their coherent dynamics directly in time domain. The respective transition dipole moment are $d_{cv} = e_0 \cdot 4$ nm and $d_{2ph} = e_0 \cdot 220$ fm. The extraordinarely large interband dipole moment d_{cv} led the light-matter interaction into the nonperturbative regime. In such a condition each pulse interacts multiple times thereby allowing to drive the two-quantum excitations off-resonantly.

- The predominant generation mechanism for the two-photon interband coherence signal is a $\chi^{(5)}$ nonlinear process in the driving field. The first THz pulse drives the two-photon interband coherent polarization by involving the large interband dipole moment twice. Depending on the relative phase between the two-photon interband coherent polarization and the second pulse, the latter can either induce stimulated emission or experience two photon-absorption, thereby modulating the population in both the valence and the conduction bands. The last pulse finally probes the modulated free charge-carrier absorption. The latter is mainly caused by intervalence

absorption of holes from the heavy-hole to the light-hole bands. The electric field of the two-photon interband coherence exhibits an amplitude of up to 0.5 kV/cm and decays on a time scale of 300 fs.

- In the generation scheme for the two-phonon coherence, electronic excitations in the conduction band induced via d_{cv} are coupled to the two-phonon state through the Frank-Condon transition dipole moment $d_{fc} = 0.4$ nm, so involving a vibronic transition. Once excited, the oscillating two-phonon coherent polarization radiates at 10 THz involving the extremely small two-phonon dipole d_{2ph}. The two-phonon electric-field amplitude is of up to 2 kV/cm and decays within 450 fs. The decay of the two-phonon polarization is caused by an inhomogeneous broadening mechanism.

In this thesis, a 2D collinear THz spectroscopy with three inherently phase-locked THz pulses is demonstrated for the first time. This novel technique, which is based on phase-resolved detection, could be applied to investigate the coherent response on ferroelectric soft-phonon excitations while approaching the phase transition. A further application could be to study coherent interactions among collective excitations like magnons in ferromagnetic systems, thereby achieving valuable insight in magnetic multi-quantum coherences. Our spectroscopic approach can be straightforwardly extended to a higher number of pulses and be readily developed into a two-colour nonlinear spectroscopy [34].

Publications

The work presented in this thesis is based on the following articles in refereed journals and books:

- C. Somma, K. Reimann, C. Flytzanis, M. Woerner, T. Elsaesser. *High-field terahertz bulk photovoltaic effect in lithium niobate.* Physical Review Letters **112**, 146602 (2014).

- C. Somma, K. Reimann, M. Woerner, T. Elsaesser, C. Flytzanis. *Ultrafast terahertz response of lithium niobate in the nonperturbative regime. Ultrafast Phenomena XIX*, Springer Proceedings in Physics **162**, 620-622 (2015).

- C. Somma, K. Reimann, M. Woerner, T. Elsaesser, C. Flytzanis. *Ultrafast THz photo-galvanic carrier transport. Extreme field induced regime.* Romanian Reports in Physics **67**, 1597-1601 (2015).

- C. Somma, G. Folpini, J. Gupta, K. Reimann, M. Woerner, T. Elsaesser. *Ultra-broadband terahertz pulses generated in the organic crystal DSTMS.* Optics Letters **40**, 3404-3407 (2015).

- C. Somma, G. Folpini, K. Reimann, M. Woerner, T. Elsaesser. *Phase-resolved two-dimensional terahertz spectroscopy including offresonant interactions beyond the $\chi^{(3)}$ limit.* Journal of Chemical Physics **144**, 184202 (2016).

- C. Somma, G. Folpini, K. Reimann, M. Woerner, T. Elsaesser. *Two-phonon quantum coherences in indium antimonide studied by nonlinear two-dimensional terahertz spectroscopy.* Physical Review Letters **116**, 177401 (2016).

Conference Proceedings:

- C. Somma, K. Reimann, M. Woerner, T. Elsaesser, C. Flytzanis. *High-field terahertz shift current in lithium niobate.* Conference on Lasers and Electro-Optics (CLEO) in San Jose, California (USA), June (2015).

- C. Somma, K. Reimann, M. Woerner, T. Elsaesser, C. Flytzanis. *Ultrafast THz bulk photovoltaic effect in lithium niobate in the nonperturbative regime.* Optical Terahertz Science and Technology Conference in San Diego, California (USA), March (2015).

- C. Somma, G. Folpini, J. Gupta, K. Reimann, M. Woerner, T. Elsaesser. *Generation of ultra-broadband transients in the organic crystal DSTMS.* German THz Conference in Dresden, Germany, June (2015).

- C. Somma, G. Folpini, K. Reimann, M. Woerner, T. Elsaesser. *Two-phonon quantum coherences in InSb observed by two-dimensional three-pulse THz spectroscopy.* The 8th International Conference on Coherent Multidimensional Spectroscopy in Groningen, Netherlands, June (2016).

- C. Somma, G. Folpini, K. Reimann, M. Woerner, T. Elsaesser. *Two-phonon quantum coherences in InSb studied by two-dimensional terahertz spectroscopy.* The 20th International Conference on Ultrafast Phenomena in Santa Fe, New Mexico (USA), July (2016).

Bibliography

[1] M. Abo-Bakr, J. Feikes, K. Holldack, P. Kuske, W. B. Peatman, U. Schade, G. Wüstefeld, and H.-W. Hübers. Brilliant, coherent far-infrared (THz) synchrotron radiation. *Phys. Rev. Lett.*, 90:094801, 2003.

[2] M. M. Abouellell and F. J. Leonberger. Waveguides in lithium niobate. *J. Am. Ceram. Soc.*, 72:1311–1321, 1989.

[3] S. C. Abrahams, W. C. Hamilton, and J. M. Reddy. Ferroelectric lithium niobate. 4. Single crystal neutron diffraction study at 24°C. *J. Phys. Chem. Solids*, 27:1013–1018, 1966.

[4] S. C. Abrahams, J. M. Reddy, and J. L. Bernstein. Ferroelectric lithium niobate. 3. Single crystal X-ray diffraction study at 24°C. *J. Phys. Chem. Solids*, 27:997–1012, 1966.

[5] W. P. Aue, E. Bartholdi, and R. R. Ernst. Two-dimensional spectroscopy. Application to nuclear magnetic resonance. *J. Chem. Phys.*, 64:2229–2246, 1976.

[6] D. H. Auston and M. C. Nuss. Electrooptical generation and detection of femtosecond electrical transients. *IEEE J. Quant. Electron.*, 24:184–197, 1988.

[7] D. H. Auston and P. R. Smith. Generation and detection of millimeter waves by picosecond photoconductivity. *Appl. Phys. Lett.*, 43:631–633, 1983.

[8] T. Balčiūnas, D. Lorenc, M. Ivanov, O. Smirnova, A. M. Zheltikov, D. Dietze, K. Unterrainer, T. Rathje, G. G. Paulus, A. Baltuška, and S. Haessler. CEP-stable tunable THz-emission originating from laser-waveform-controlled sub-cycle plasma-electron bursts. *Opt. Express*, 23:15278–15289, 2015.

[9] T. Bartel, P. Gaal, K. Reimann, M. Woerner, and T. Elsaesser. Generation of single-cycle THz transients with high electric-field amplitudes. *Opt. Lett.*, 30:2805–2807, 2005.

[10] F. Blanchard, G. Sharma, X. Ropagnol, L. Razzari, R. Morandotti, and T. Ozaki. Improved terahertz two-color plasma sources pumped by high intensity laser beam. *Opt. Express*, 17:6044–6052, 2009.

[11] M. Born and K. Huang. *Dynamical Theory of Crystal Lattices.* Oxford University Press, London, 1954.

[12] Ch. Bosshard, M. Bösch, I. Liakatas, M. Jäger, and P. Günter. Nonlinear Optical Effects and Materials. *Nonlinear Optical Effects and Materials*, 2000.

[13] P. Bowlan, E. Martinez-Moreno, K. Reimann, T. Elsaesser, and M. Woerner. Ultrafast terahertz response of multi-layer graphene in the nonperturbative regime. *Phys. Rev. B*, 89:041408(R), 2014.

[14] T. Brixner, J. Stenger, H. M. Vaswani, M. Cho, R. E. Blankenship, and G. R. Fleming. Two-dimensional spectroscopy of electronic couplings in photosynthesis. *Nature*, 434:625–628, 2005.

[15] F. D. J. Brunner. *Generation and detection of terahertz pulses in the organic crystals OH1 and COANP.* PhD thesis, ETH Zürich, 2009.

[16] F. D. J. Brunner, S.-H. Lee, O.-P. Kwon, and T. Feurer. THz generation by optical rectification of near-infrared laser pulses in the organic nonlinear optical crystal HMQ-TMS. *Opt. Mater. Express*, 4:1586–1592, 2014.

[17] J. C. Cao. Interband impact ionization and nonlinear absorption of terahertz radiation in semiconductor heterostructures. *Phys. Rev. Lett.*, 91:237401, 2003.

[18] G. L. Carr, M. C. Martin, W. R. McKinney, K. Jordan, G. R. Neil, and G. P. Williams. High-power terahertz radiation from relativistic electrons. *Nature*, 420:153–156, 2002.

[19] F. S. Chen, J. T. LaMacchia, and D. B. Fraser. Holographic storage in lithium niobate. *Appl. Phys. Lett.*, 13:223–225, 1968.

[20] Y. H. Chen and Y. C. Huang. Actively Q-switched Nd:YVO_4 laser using an electro-optic periodically poled lithium niobate crystal as a laser Q-switch. *Opt. Lett.*, 28:1460–1462, 2003.

[21] Y. C. Cheng and G. R. Fleming. Dynamics of light harvesting in photosynthesis. *Phys. Chem.*, 60, 2009.

[22] H. S. Chung, Z. Ganim, K. C. Jones, and A. Tokmakoff. Transient 2D IR spectroscopy of ubiquitin unfolding dynamics. *Proc. Natl. Acad. Sci. USA*, 104:14237–14242, 2007.

[23] D. Côté, N. Laman, and H. M. van Driel. Rectification and shift currents in GaAs. *Appl. Phys. Lett.*, 80:905–907, 2002.

[24] Paul D Cunningham and L Michael Hayden. Optical properties of dast in the thz range. *Optics express*, 18(23):23620–23625, 2010.

[25] X. Dai, A. D. Bristow, D. Karaiskaj, and S. T. Cundiff. Two-dimensional Fourier-transform spectroscopy of potassium vapor. *Phys. Rev. A*, 82:052503, 2010.

[26] C. V. De Alvarez, J. P. Walter, R. W. Boyd, and M. L. Cohen. Calculated band structures, optical constants and electronic charge densities for InAs and InSb. *J. Phys. Chem. Solids*, 34:337–345, 1973.

[27] A. Di Carlo, P. Vogl, and W. Pötz. Theory of Zener tunneling and Wannier-Stark states in semiconductors. *Phys. Rev. B*, 50:8358–8377, 1994.

[28] M. J. Dodge. Refractive properties of magnesium fluoride. *Appl. Opt.*, 23:1980–1985, 1984.

[29] A. Dreyhaupt, S. Winnerl, M. Helm, and T. Dekorsy. Optimum excitation conditions for the generation of high-electric-field terahertz radiation from an oscillator-driven photoconductive device. *Opt. Lett.*, 31:1546–1548, 2006.

[30] M. D. Fayer. Dynamics of water interacting with interfaces, molecules, and ions. *Acc. Chem. Res.*, 45:3–14, 2011.

[31] C. J. Fecko, J. D. Eaves, J. J. Loparo, A. Tokmakoff, and P. L. Geissler. Ultrafast hydrogen-bond dynamics in the infrared spectroscopy of water. *Science*, 301:1698–1702, 2003.

[32] N. C. Fernelius. Properties of gallium selenide single crystal. *Prog. Crystal Growth and Charact.*, 28:275–353, 1994.

[33] R. Fieschi. Matter tensors in the crystallographic groups of Cartesian symmetry. *Physica*, 23:972–976, 1957.

[34] G. Folpini, D. Morrill, C. Somma, K. Reimann, M. Woerner, T. Elsaesser, and K. Biermann. Nonresonant coherent control—intersubband excitations manipulated by a nonresonant terahertz pulse. *Phys. Rev. B*, 92:085306, 2015.

[35] S. J. Fray, F. A. Johnson, and R. H. Jones. Lattice absorption bands in indium antimonide. *Proc. Phys. Soc.*, 76:939, 1960.

[36] J. A. Fülöp, L. Pálfalvi, S. Klingebiel, G. Almási, F. Krausz, S. Karsch, and J. Hebling. Generation of sub-mJ terahertz pulses by optical rectification. *Opt. Lett.*, 37:557–559, 2012.

[37] P. Gaal, W. Kuehn, K. Reimann, M. Woerner, T. Elsaesser, and R. Hey. Internal motions of a quasiparticle governing its ultrafast nonlinear response. *Nature*, 450:1210–1213, 2007.

[38] P. Gaal, W. Kuehn, K. Reimann, M. Woerner, T. Elsaesser, R. Hey, J. S. Lee, and U. Schade. Carrier-wave Rabi flopping on radiatively coupled shallow donor transitions in n-type GaAs. *Phys. Rev. B*, 77:235204, 2008.

[39] F. Gao, S. T. Cundiff, and H. Li. Probing dipole–dipole interaction in a rubidium gas via double-quantum 2D spectroscopy. *Opt. Lett.*, 41:2954–2957, 2016.

[40] A. M. Glass, D. von der Linde, and T. J. Negran. High-voltage bulk photovoltaic effect and the photorefractive process in $LiNbO_3$. *Appl. Phys. Lett.*, 25:233–235, 1974.

[41] G. W. Gobeli and H. Y. Fan. Infrared absorption and valence band in indium antimonide. *Phys. Rev.*, 119:613–620, 1960.

[42] B. Guchhait, Y. Liu, T. Siebert, and T. Elsaesser. Ultrafast vibrational dynamics of the DNA backbone at different hydration levels mapped by two-dimensional infrared spectroscopy. *Struct. Dyn.*, 3(4):043202, 2016.

[43] P. Hamm, M. Lim, and R. M. Hochstrasser. Structure of the amide I band of peptides measured by femtosecond nonlinear-infrared spectroscopy. *J. Phys. Chem. B*, 102:6123–6138, 1998.

[44] P. Hamm and M. Zanni. *Concepts and Methods of 2D Infrared Spectroscopy*. Cambridge University Press, Cambridge, 2011.

[45] H. Haug and S. W. Koch. *Quantum Theory of the Optical and Electronic Properties of Semiconductors*. World Scientific, Singapore, 1993.

[46] C. P. Hauri, C. Ruchert, C. Vicario, and F. Ardana. Strong-field single-cycle THz pulses generated in an organic crystal. *Appl. Phys. Lett.*, 99:161116, 2011.

[47] A. P. Heberle, J. J. Baumberg, and K. Köhler. Ultrafast coherent control and destruction of excitons in quantum wells. *Phys. Rev. Lett.*, 75:2598, 1995.

[48] J. Hebling, Ka-Lo Yeh, M. C. Hoffmann, B. Bartal, and K. A. Nelson. Generation of high-power terahertz pulses by tilted-pulse-front excitation and their application possibilities. *J. Opt. Soc. Am. B*, 25:B6–B19, 2008.

[49] H. Hirori, A. Doi, F. Blanchard, and K. Tanaka. Single-cycle terahertz pulses with amplitudes exceeding 1 MV/cm generated by optical rectification in $LiNbO_3$. *Appl. Phys. Lett.*, 98:091106, 2011.

[50] H. Hirori, K. Shinokita, M. Shirai, S. Tani, Y. Kadoya, and K. Tanaka. Extraordinary carrier multiplication gated by a picosecond electric field pulse. *Nature Commun.*, 2:594, 2011.

[51] R. M. Hochstrasser. Two-dimensional spectroscopy at infrared and optical frequencies. *Proc. Natl. Acad. Sci. USA*, 104:14190–14196, 2007.

[52] M. C. Hoffmann, J. Hebling, H. Y. Hwang, Ka-Lo Yeh, and K. A. Nelson. Impact ionization in InSb probed by terahertz pump—terahertz probe spectroscopy. *Phys. Rev. B*, 79:161201(R), 2009.

[53] M. C. Hoffmann, J. Hebling, H. Y. Hwang, Ka-Lo Yeh, and K. A. Nelson. THz-pump/THz-probe spectroscopy of semiconductors at high field strengths. *J. Opt. Soc. Am. B*, 26:A29–34, 2009.

[54] B. Jensen. Theory of free carrier absorption in InSb. *Solid State Commun.*, 9:1587–1589, 1971.

[55] D. M. Jonas. Two-dimensional femtosecond spectroscopy. *Annu. Rev. Phys. Chem.*, 54:425–463, 2003.

[56] R. A. Kaindl, F. Eickemeyer, M. Woerner, and T. Elsaesser. Broadband phase-matched difference frequency mixing of femtosecond pulses in GaSe: experiment and theory. *Appl. Phys. Lett.*, 75:1060–1062, 1999.

[57] I. P. Kaminow, V. Ramaswamy, R. V. Schmidt, and E. H. Turner. Lithium niobate ridge waveguide modulator. *Appl. Phys. Lett.*, 24:622–624, 1974.

[58] E. O. Kane. Zener tunneling in semiconductors. *J. Phys. Chem. Solids*, 12:181–188, 1959.

[59] D. Karaiskaj, A. D. Bristow, L. Yang, X. Dai, R. P. Mirin, S. Mukamel, and S. T. Cundiff. Two-quantum many-body coherences in two-dimensional Fourier-transform spectra of exciton resonances in semiconductor quantum wells. *Phys. Rev. Lett.*, 104:117401, 2010.

[60] D. Karaiskaj, A. D. Bristow, L. Yang, X. Dai, R. P. Mirin, S. Mukamel, and S. T. Cundiff. Two-quantum many-body coherences in two-dimensional Fourier-transform spectra of exciton resonances in semiconductor quantum wells. *Phys. Rev. Lett.*, 104:117401, 2010.

[61] B. J. Keay, S. J. Allen Jr., J. Galán, J. P. Kaminski, K. L. Campman, A. C. Gossard, U. Bhattacharya, and M. J. W. Rodwell. Photon-assisted electric field domains and multiphoton-assisted tunneling in semiconductor superlattices. *Phys. Rev. Lett.*, 75:4098, 1995.

[62] F. R. Kessler and E. Sutter. Über die Ultrarotabsorption freier Ladungsträger bei nichtparabolischer Bandstruktur am Beispiel InSb. *Zeitschrift für Naturforschung A*, 16:1173–1179, 1961.

[63] M. Khalil, N. Demirdöven, and A. Tokmakoff. Coherent 2D IR spectroscopy: Molecular structure and dynamics in solution. *J. Phys. Chem. A*, 107:5258–5279, 2003.

[64] W. Kiefer, W. Richter, and M. Cardona. Second-order Raman scattering in InSb. *Phys. Rev. B*, 12:2346–2354, 1975.

[65] Dai-Sik Kim, J. Shah, J. E. Cunningham, T. C. Damen, S. Schmitt-Rink, and W. Schäfer. Carrier-carrier scattering in a degenerate electron system: Strong inhibition of scattering near the Fermi edge. *Phys. Rev. Lett.*, 68:2838–2841, 1992.

[66] J. Kim, S. Mukamel, and G. D. Scholes. Two-dimensional electronic double-quantum coherence spectroscopy. *Accounts Chem. Res.*, 42:1375–1384, 2009.

[67] Pil-Joo Kim, Mojca Jazbinsek, and O-Pil Kwon. Selective growth of highly efficient electrooptic stilbazolium crystals by sequential crystal growth in different solvents. *Crystal Growth & Design*, 11(7):3060–3064, 2011.

[68] W. T. H. Koch, R. Munser, W. Ruppel, and P. Würfel. Bulk photovoltaic effect in $BaTiO_3$. *Solid State Commun.*, 17:847–850, 1975.

[69] W. T. H. Koch, R. Munser, W. Ruppel, and P. Würfel. Anomalous photovoltage in $BaTiO_3$. *Ferroelectrics*, 13:305–307, 1976.

[70] C. Kolano, J. Helbing, M. Kozinski, W. Sander, and P. Hamm. Watching hydrogen-bond dynamics in a β-turn by transient two-dimensional infrared spectroscopy. *Nature*, 444:469–472, 2006.

[71] E. S. Koteles, W. R. Datars, and G. Dolling. Far-infrared phonon absorption in InSb. *Phys. Rev. B*, 9:572–582, 1974.

[72] E. Krätzig and H. Kurz. Photo-induced currents and voltages in $LiNbO_3$. *Ferroelectrics*, 13:295–296, 1976.

[73] W. Kraut and R. von Baltz. Anomalous bulk photovoltaic effect in ferroelectrics: A quadratic response theory. *Phys. Rev. B*, 19:1548–1554, 1979.

[74] C. Kübler, R. Huber, and A. Leitenstorfer. Ultrabroadband terahertz pulses: generation and field-resolved detection. *Semicond. Sci. Technol.*, 20:S128–133, 2005.

[75] C. Kübler, R. Huber, S. Tübel, and A. Leitenstorfer. Ultrabroadband detection of multi-terahertz field transients with GaSe electro-optic sensors: Approaching the near infrared. *Appl. Phys. Lett.*, 85:3360–3362, 2004.

[76] W. Kuehn, P. Gaal, K. Reimann, M. Woerner, T. Elsaesser, and R. Hey. Coherent ballistic motion of electrons in a periodic potential. *Phys. Rev. Lett.*, 104:146602, 2010.

[77] W. Kuehn, P. Gaal, K. Reimann, M. Woerner, T. Elsaesser, and R. Hey. THz-induced interband tunneling of electrons in GaAs. *Phys. Rev. B*, 82:075204, 2010.

[78] W. Kuehn, K. Reimann, M. Woerner, and T. Elsaesser. Phase-resolved two-dimensional spectroscopy based on collinear n-wave mixing in the ultrafast time domain. *J. Chem. Phys.*, 130:164503, 2009.

[79] W. Kuehn, K. Reimann, M. Woerner, T. Elsaesser, and R. Hey. Two-dimensional terahertz correlation spectra of electronic excitations in semiconductor quantum wells. *J. Phys. Chem. B*, 115:5448–5455, 2011.

[80] S. W. Kurnick and J. M. Powell. Optical absorption in pure single crystal InSb at 298 and 78 K. *Phys. Rev.*, 116:597, 1959.

[81] Y. S. Lee, T. Meade, V. Perlin, H. Winful, T. B. Norris, and A. Galvanauskas. Generation of narrow-band terahertz radiation via optical rectification of femtosecond pulses in periodically poled lithium niobate. *Appl. Phys. Lett.*, 76:2505–2507, 2000.

[82] A. Leitenstorfer, S. Hunsche, J. Shah, M. C. Nuss, and W. H. Knox. Detectors and sources for ultrabroadband electro-optic sampling: Experiment and theory. *Appl. Phys. Lett.*, 74:1516–1518, 1999.

[83] Y. Li, J. Zhang, G. Zhang, L. Wu, P. Fu, and Y. Wu. Growth and characterization of DSTMS crystals. *J. Cryst. Growth*, 327:127–132, 2011.

[84] P. Liu, D. Xu, Y. Li, X. Zhang, Y. Wang, J. Yao, and Y. Wu. Widely tunable and monochromatic terahertz difference frequency generation with organic crystal DSTMS. *Europhys. Lett.*, 106:60001, 2014.

[85] P. Liu, D. Xu, Y. Li, X. Zhang, Y. Wang, J. Yao, and Y. Wu. Widely tunable and monochromatic terahertz difference frequency generation with organic crystal DSTMS. *EPL*, 106:60001, 2014.

[86] Chih-Wei Luo, Yu-Ting Wang, A. Yabushita, and T. Kobayashi. Ultrabroadband time-resolved spectroscopy in novel types of condensed matter. *Optica*, 3:82–92, 2016.

[87] B. T. Matthias and J. P. Remeika. Ferroelectricity in the ilmenite structure. *Phys. Rev.*, 76:1886–1887, 1949.

[88] T. A. McMath and J. C. Irwin. Indices of refraction of GaS and GaSe. *Phys. Status Solidi A*, 38:731–738, 1976.

[89] A. Miller, A. Johnston, J. Dempsey, J. Smith, C. R. Pidgeon, and G. D. Holah. Two-photon absorption in InSb and $Hg_{1-x}Cd_xTe$. *J. Phys. C*, 12:4839–4849, 1979.

[90] G.D. Miller, R.G. Batchko, W.M. Tulloch, D.R. Weise, M.M. Fejer, and R.L. Byer. 42%-efficient single-pass cw second-harmonic generation in periodically poled lithium niobate. *Opt. Lett.*, 22:1834–1836, 1997.

[91] B. Monoszlai, C. Vicario, M. Jazbinsek, and C. P. Hauri. High-energy terahertz pulses from organic crystals: DAST and DSTMS pumped at Ti: sapphire wavelength. *Opt. Lett.*, 38:5106–5109, 2013.

[92] S. Mukamel. *Principles of Nonlinear Optical Spectroscopy.* Oxford University Press, New York, 1995.

[93] S. Mukamel. Multidimensional femtosecond correlation spectroscopies of electronic and vibrational excitations. *Annu. Rev. Phys. Chem.*, 51:691–729, 2000.

[94] L. Mutter, F. D. Brunner, Z. Yang, M. Jazbinšek, and P. Günter. Linear and nonlinear optical properties of the organic crystal DSTMS. *J. Opt. Soc. Am. B*, 24:2556–2561, 2007.

[95] L. E. Myers, W. R. Bosenberg, G. D. Miller, R. C. Eckardt, M. M. Fejer, and R. L. Byer. Quasi-phase-matched 1.064-μm-pumped optical parametric oscillator in bulk periodically poled $LiNbO_3$. *Opt. Lett.*, 20:52–54, 1995.

[96] F. Nastos and J. E. Sipe. Optical rectification and shift currents in GaAs and GaP response: Below and above the band gap. *Phys. Rev. B*, 74:035201, 2006.

[97] P. Nuernberger, G. Vogt, T. Brixner, and G. Gerber. Femtosecond quantum control of molecular dynamics in the condensed phase. *Phys. Chem. Chem. Phys.*, 9:2470–2497, 2007.

[98] S. Park, K. Kwak, and M. D. Fayer. Ultrafast 2D-IR vibrational echo spectroscopy: a probe of molecular dynamics. *Laser Phys. Lett.*, 4:704–718, 2007.

[99] C. R. Pidgeon, B. S. Wherrett, A. M. Johnston, J. Dempsey, and A. Miller. Two-photon absorption in zinc-blende semiconductors. *Phys. Rev. Lett.*, 42:1785–1788, 1979. **43**, 1843(E) (1979).

[100] A. Polian. Brillouin scattering studies of rare gas solids. *High Pressure Res.*, 9:205–217, 1992.

[101] W. T. Pollard, S. L. Dexheimer, Q. Wang, L. A. Peteanu, C. V. Shank, and R. A. Mathies. Theory of dynamic absorption spectroscopy of nonstationary states. 4. Application to 12-fs resonant impulsive Raman spectroscopy of bacteriorhodopsin. *J. Phys. Chem.*, 96:6147–6158, 1992.

[102] M. M. Pradhan, R. K. Garg, and M. Arora. Multiphonon infrared absorption in silicon. *Infrared Phys.*, 27:25–30, 1987.

[103] K. Reimann, R. P. Smith, A. M. Weiner, T. Elsaesser, and M. Woerner. Direct field-resolved detection of terahertz transients with amplitudes of megavolts per centimeter. *Opt. Lett.*, 28:471–473, 2003.

[104] C. Ruchert, C. Vicario, Hauri, and C. P. Christoph. Spatiotemporal focusing dynamics of intense supercontinuum THz pulses. *Phys. Rev. Lett.*, 110:123902, 2013.

[105] J. Savolainen, S. Ahmed, and P. Hamm. Two-dimensional Raman-terahertz spectroscopy of water. *Proc. Natl. Acad. Sci. USA*, 110:20402–20407, 2013.

[106] A. Schneider, M. Neis, M. Stillhart, Bl. Ruiz, R. U. A. Khan, and P. Günter. Generation of terahertz pulses through optical rectification in organic DAST crystals: theory and experiment. *J. Opt. Soc. Am. B*, 23:1822–1835, 2006.

[107] T. Seidler, K. Stadnicka, and B. Champagne. Linear and second-order nonlinear optical properties of ionic organic crystals. *J. Chem. Phys.*, 141:104109, 2014.

[108] Y. C. Shen, P. C. Upadhya, H. E. Beere, E. H. Linfield, A. G. Davies, I. S. Gregory, C. Baker, W. R. Tribe, and M. J. Evans. Generation and detection of ultrabroadband terahertz radiation using photoconductive emitters and receivers. *Appl. Phys. Lett.*, 85:164–166, 2004.

[109] S. K. Sinba. Phonons in semiconductors. *CRC Crit. Rev. Solid State Sci.*, 3:273–334, 1973.

[110] J. E. Sipe and A. I. Shkrebtii. Second-order optical response in semiconductors. *Phys. Rev. B*, 61:5337–5352, 2000.

[111] P. R. Smith, D. H. Auston, and M. C. Nuss. Subpicosecond photoconducting dipole antennas. *IEEE J. Quant. Electron.*, 24:255–260, 1988.

[112] W. G. Spitzer and H. Y. Fan. Infrared absorption in Indium Antimonide. *Phys. Rev.*, 99:1893–1894, 1955.

[113] M. Stillhart, A. Schneider, and P. Günter. Optical properties of 4-N, N-dimethylamino-4-N-methyl-stilbazolium 2, 4, 6-trimethylbenzenesulfonate crystals at terahertz frequencies. *J. Opt. Soc. Am. B*, 25:1914–1919, 2008.

[114] Y. Takahashi, H. Adachi, T. Taniuchi, M. Takagi, Y. Hosokawa, S. Onzuka, S. Brahadeeswaran, M. Yoshimura, Y. Mori, H. Masuhara, T. Sasaki, and H. Nakanishi. Organic nonlinear optical DAST crystals for electro-optic measurement and terahertz wave generation. *J. Photochem. Photobiol. A*, 183:247–252, 2006.

[115] H. S. Tan. Theory and phase-cycling scheme selection principles of collinear phase coherent multi-dimensional optical spectroscopy. *J. Chem. Phys.*, 129:124501, 2008.

[116] M. Van Exter, Ch. Fattinger, and D. Grischkowsky. Terahertz time-domain spectroscopy of water vapor. *Opt. Lett.*, 14:1128–1130, 1989.

[117] C. Vicario, B. Monoszlai, and C. P. Hauri. GV/m single-cycle terahertz fields from a laser-driven large-size partitioned organic crystal. *Phys. Rev. Lett.*, 112:213901, 2014.

[118] C. Vicario, A. V. Ovchinnikov, S. I. Ashitkov, M. B. Agranat, V. E. Fortov, and C. P. Hauri. Generation of 0.9-mJ THz pulses in DSTMS pumped by a Cr:Mg_2 SiO_4 laser. *Opt. Lett.*, 39:6632–6635, 2014.

[119] T. Vijayakumar, I. Hubert Joe, C. P. Reghunadhan Nair, M. Jazbinsek, and V. S. Jayakumar. Electron–phonon coupling and vibrational modes contributing to linear electro-optic effect of the efficient NLO chromophore 4-(N, N-dimethylamino)-N-methyl-4′-toluene sulfonate (DAST) from their vibrational spectra. *J. Raman Spectrosc.*, 40:52–63, 2009.

[120] M. S. Vitiello and A. Tredicucci. Tunable emission in THz quantum cascade lasers. *IEEE Trans. THz Sci. Technol.*, 1:76–84, 2011.

[121] R. von Baltz and W. Kraut. Theory of the bulk photovoltaic effect in pure crystals. *Phys. Rev. B*, 23:5590–5596, 1981.

[122] R. S. Weis and T. K. Gaylord. Lithium niobate: Summary of physical properties and crystal structure. *Appl. Phys. A*, 37:191–203, 1985.

[123] S. H. Wemple, M. DiDomenico, Jr., and I. Camlibel. Relationship between linear and quadratic electro-optic coefficients in $LiNbO_3$, $LiTaO_3$, and other oxygen-octahedra ferroelectrics based on direct measurement of spontaneous polarization. *Appl. Phys. Lett.*, 12:209–211, 1968.

[124] B. S. Williams. Terahertz quantum-cascade lasers. *Nature photonics*, 1:517–525, 2007.

[125] B. S. Williams, H. Callebaut, S. Kumar, Q. Hu, and J. L. Reno. 3.4-THz quantum cascade laser based on longitudinal-optical-phonon scattering for depopulation. *Appl. Phys. Lett.*, 82:1015–1017, 2003.

[126] W. Xiong and M. Zanni. Signal enhancement and background cancellation in collinear two-dimensional spectroscopies. *Opt. Lett.*, 33:1371–1373, 2008.

[127] Z. Yang, L. Mutter, M. Stillhart, B. Ruiz, S. Aravazhi, M. Jazbinsek, A. Schneider, V. Gramlich, and P. Günter. Large-Size Bulk and Thin-Film Stilbazolium-Salt Single Crystals for Nonlinear Optics and THz Generation. *Adv. Funct. Mater.*, 17:2018–2023, 2007.

[128] K. L. Yeh, M. C. Hoffmann, J. Hebling, and K. A. Nelson. Generation of 10 μJ ultrashort terahertz pulses by optical rectification. *Appl. Phys. Lett*, 90:1–3, 2007.

[129] S. M. Young and A. M. Rappe. First principles calculation of the shift current photovoltaic effect in ferroelectrics. *Phys. Rev. Lett.*, 109:116601, 2012.

[130] J. Zheng, K. Kwak, J. Asbury, X. Chen, I. R. Piletic, and M. D. Fayer. Ultrafast dynamics of solute-solvent complexation observed at thermal equilibrium in real time. *Science*, 309:1338–1343, 2005.

[131] W. H. Zurek. Decoherence and the transition from quantum to classical. *Phys. Today*, 44(10):36–44, 1991.

[132] W. H. Zurek. Decoherence and the transition from quantum to classical—revisited. *Los Alamos Science*, 27:86–109, 2002.

Acknowledgements

Many people have contributed to make my PhD period formative, joyful and, summarized in one word, memorable.

I would like to express my sincere gratitude to my PhD supervisor Prof. Dr. Thomas Elsaesser for giving me the opportunity to pursue my PhD study and related research in the THz group at the Max Born Institute, for his patience and his motivation. His guidance helped me in all the time of research and writing of this thesis.

Besides my supervisor, I would like to thank the rest of my thesis committee: Prof. Dr. Kurt Busch, Prof. Dr. Manfred Helm, Prof. Dr. Oliver Benson and Prof. Dr. Ted Masselink for their insightful comments but also for the hard questions which stimulated me to widen my research from various perspectives.

My sincere thanks also goes to the head of my department Dr. Michael Woerner. His ideas and deep understanding of Physics have contributed to the success of this work.

I am grateful to Prof. Dr. Klaus Reinmann for having showed me experimental tricks to successfully perform the experiments, for his clear answers to many of my questions on difficult topics of Physics. His clear picture of complex physical processes has enlighten me throughout writing this thesis.

I also want to thank my former and current fellows: Drew, Sebastian, Marcel, Cristoph, Tony, Keisuke, Jannick and Giulia. The stimulating discussions, the time spent out of the institute life (going to concerts, organizing barbecues, birthday parties and ...) have contributed to create a friendly working environment. Thanks for the marvellous doctoral nerdy hat.

I am grateful to the many friends I have made: Milena, Radeck, Hanni, Janicka and Sophie, you all have contributed to make Berlin home.

I feel a sense of deep gratitude for Giulia and Michele. Getting to know you has been one of the most important experiences of the last four years. I thank you for your encouragement, constant support throughout writing this thesis, for our trips, for the laughter, for the friendship.

Finally, I would like to express my particular gratitude to my parents to whom this thesis is dedicated, for having instilled in me the curiosity and the courage for the long journey of my life.

List of Figures

List of Tables

Declarations

I declare that I have produced this doctor's thesis independently using only the literature and the tools I have specified, in accordance with section 7 para. 3 of the Faculty of Mathematics and Natural Sciences PhD regulations, published in the Official Gazette of Humboldt-Universität zu Berlin (*Amtliches Mitteilungsblatt*) no. 126/2014 on 18/11/2014.

I have not applied for a doctoral degree in the doctoral subject of Physics elsewhere and do not hold a doctoral degree in the doctoral subject of Physics.

I have taken due note of the Faculty of Mathematics and Natural Sciences PhD Regulations, published in the Official Gazette of Humboldt-Universität zu Berlin (*Amtliches Mitteilungsblatt*) no. 126/2014 on 18/11/2014.

Berlin, 19th January 2017 Carmine Somma